DIPLOMARBEIT

Monitoring of electrical performance and material stability of PV modules with repaired/coated backsheets

zur Erlangung des akademischen Grades

Diplom-Ingenieurin

im Rahmen des Studiums

Physikalische Energie- und Messtechnik

eingereicht von

Anika Gassner, BSc
Matrikelnummer: 01610625

ausgeführt am Institut für Angewandte Physik (IAP)
der Fakultät für Physik der Technischen Universität Wien
in Zusammenarbeit mit dem Österreichisches Forschungsinstitut für Chemie und Technik (OFI)

unter der Betreuung durch
Ao.Univ.-Prof. Dipl.-Ing. Dr. techn. Martin **Gröschl** (IAP)
Dipl.-Ing. Dr. techn. Gabriele C. **Eder** (OFI)

Wien, 10.10.2022

(Unterschrift Verfasser/in) (Unterschrift Betreuer/in)

Abstract

As photovoltaics play a key role in the energy transition, the reliability of PV modules is crucial. In recent years, however, several backsheet failures were observed after only few years in the field, especially cracking of polyamide backsheets. To avoid disposal of these modules, which would be necessary due to safety reasons, repair solutions for the cracked backsheets were developed. First tests had identified two types of coatings based on polyurethane and silicone, which showed promising results in respect to crack filling and protection of the backsheet from further degradation.

To monitor the long-term stability of the repaired modules with these two coatings in an outdoor environment (test site) we set up a monitoring system. The goal was to investigate, the stability of the coating on the backsheet as well as the electrical performance of the test site over time. To this end, we performed a non-destructive material analysis of the coatings on a two-monthly basis with portable spectrometers, NIR, ATR-IR, and Raman. Potential ageing induced changes in the surface morphology were analysed with the naked eye and with a light microscope. Additionally, I programmed a microcontroller so that the coated modules' electrical performance, their temperature and the environmental parameters ambient temperature and plane-of-array irradiation at the test site can be monitored continuously.

Calculations of the nominal power and the efficiency revealed that the electrical performance of the modules was neither affected by the cracks so far nor by the applied coating within eight months after coating. Visual inspection showed some minor changes in the two coatings after the cold winter months. Nevertheless, all cracks are still sealed, so the repair coating fulfils its purpose. Additionally, the spectroscopic measurements showed that the coatings are chemically stable and do not show any adhesion loss. With the built-up monitoring system, a long-term analysis on the repaired PV modules is possible, with the aim to evaluate for how long the coating can extend the service life of modules with cracked backsheets.

Zusammenfassung

Da Photovoltaik eine tragende Rolle bei der Energiewende spielt, ist die Zuverlässigkeit von PV Modulen besonders wichtig. In den letzten Jahren häuften sich aber Berichte über verschiedene Fehler in Backsheets, vor allem von Rissen in Polyamid Backsheets. Die betroffenen Module müssten aus Sicherheitsgründen entsorgt werden, weshalb als Alternative nach Reparaturlösungen gesucht wurde. Nach ersten Tests wurden zwei geeignete Materialien für eine Beschichtung ausgewählt, Polyurethan und Silikon, welche die Risse füllen und das Backsheet vor weiterer Degradation schützen konnten.

Um die Beschichtungen auf lange Zeit zu beobachten, bauten wir ein Monitoringsystem bei einer Testanlage im Freien auf. Damit soll die Stabilität der Beschichtung und die elektrische Leistung der Testanlage erforscht werden. Dafür haben wir alle zwei Monate zerstörungsfreie Messungen mit tragbaren Geräten, mit Nahem-IR, ATR-IR, und Raman Spektrometern durchgeführt. Potentielle alterungsbedingte Veränderungen in der Oberfläche wurden mit dem Auge und einem Lichtmikroskop untersucht. Außerdem programmierte ich einen Mikrokontroller, um die elektrische Leistung der Module, die Modultemperatur und die Umweltparameter Temperatur und Einstrahlung bei der Testanlage kontinuierlich zu messen.

Nachfolgende Berechnungen zeigten, dass weder die Risse noch die Beschichtung selbst (bis zu acht Monate nach dem Beschichtungsprozess) die Nennleistung und den Wirkungsgrad beeinträchtigten. Trotz kleiner Veränderungen, die bei der visuellen Inspektion nach den kalten Wintermonaten entdeckt wurden, konnte gezeigt werden, dass alle Risse noch gefüllt sind und die Reparaturbeschichtung daher noch ihren Zweck erfüllt. Außerdem zeigten die Spektroskopie-Messungen, dass beide Beschichtungen chemisch stabil sind und kein Haftungsverlust entstand. Mit dem aufgebauten Monitoringsystem sind Langzeit-Beobachtungen möglich, um festzustellen, wie lange die Beschichtung die Lebensdauer der Module verlängern kann.

Acknowledgements

I would like to warmly thank my supervisor Gabriele Eder for giving me the appreciated opportunity to write my master's thesis at OFI in the area of photovoltaics. Additionally, for helping me with the material measurements and analysis, and for guiding me and teaching me about a variety of methods such as spectroscopy, and PV in general. Especially, thanks for introducing me to the world of Austrian PV research.

Moreover, I want to thank Karl Knöbl for his advice and improvement concerning the electrical and programming aspects of this thesis, particularly for his help with troubleshooting in these areas. A big thanks also to my colleagues at OFI, who helped me with parts of my setup, especially to Philipp Larisch and Yuliya Voronko.

Furthermore, I want to acknowledge my supervisor at TU Wien Professor Gröschl for enabling my external thesis and for the administrative support.

Finally, thanks to my grandfather, who taught me how to write scientific English, corrected this thesis, and laid the foundation of my interest in research and engineering.

October 10, 2022 Anika Gassner

Contents

1 Introduction **1**
1.1 Research Aim and Research Question . . . 6

2 Theory **7**
2.1 Photovoltaics . . . 7
2.1.1 Semiconductor Properties . . . 7
2.1.2 Generation and Recombination . . . 10
2.1.3 Carrier Transport in Semiconductors . . . 11
2.1.4 PN-Junctions . . . 12
2.1.5 Solar Cells . . . 13
2.2 Spectroscopy . . . 14
2.2.1 Physical Principles . . . 14
2.2.2 Infrared Spectroscopy . . . 17
2.2.3 Near-Infrared Spectroscopy . . . 18
2.2.4 Raman Spectroscopy . . . 19

3 PV Test Site **23**
3.1 Modules . . . 24
3.1.1 Polyamide Backsheet . . . 24
3.2 Coating of the Modules . . . 25
3.2.1 Remsolar Polyurethane Coating . . . 26
3.2.2 Dowsil Silicone Coating . . . 27
3.3 Inverter . . . 28

4 Monitoring Setup **29**
4.1 Electrical Setup . . . 29
4.1.1 Raspberry Pi . . . 29
4.1.2 Temperature Sensors . . . 31
4.1.3 Plane-of-array Irradiance Measurement . . . 33
4.1.4 Modbus TCP . . . 34
4.1.5 Electrical Characterisation . . . 37
4.2 Material-stability Setup of the Coating . . . 38
4.2.1 Adhesion Check-up . . . 38
4.2.2 Visual Inspection . . . 38
4.2.3 Infrared Spectroscopy . . . 39
4.2.4 Raman Spectroscopy . . . 40
4.2.5 Near Infrared Spectroscopy . . . 41

5 Measurement Results and Interpretation **43**
5.1 Analysis of the Electrical Characterisation . . . 43
5.1.1 Wet Leakage Test . . . 43
5.1.2 I-V Curve . . . 43

5.1.3 Analysis of the Continuously Gathered Data 45
5.2 Analysis of the Coating-stability Measurements 50
5.2.1 Backsheet of the Uncoated Reference Module 51
5.2.2 Analysis of the Remsolar Polyurethane Coating on the Backsheet 56
5.2.3 Analysis of the Dowsil Silicone Coating 62

6 Conclusion and Outlook **69**

List of Figures **73**

List of Tables **77**

Abbreviations **79**

Bibliography **81**

Chapter 1

Introduction

Changing the primary energy production from fossil fuels to renewable energies is inevitable considering the climate crisis. As of 2020 only 36.5% of the gross final energy consumption in Austria and 22.1% in the EU are generated by renewable energy sources [1]. However, this has to change drastically in the next years due to environmental but also political reasons. The new EU goal as part of the REPowerEU plan is to achieve 45% (1236 GW) of the total energy by renewables in 2030. Half of that amount (600 GW) should come from photovoltaics (PV), which points out the importance of PV in this energy transition [2]. Nowadays, not only specialists believe that PV will play a key factor in the sustainable energy transition. In Austria 11 TW h should be installed until 2030, which is five times more than the 2.783 TW h generated in 2021. This would also raise the share of electricity from PV from 4.7% in 2021 to 15% in 2030, when 100% have to be renewable. Additionally, the market growth of PV is supported by the fact that today the cheapest produced energy comes from photovoltaics in most parts of the EU. Hence, electricity production by PV makes not only sense environmentally but also economically [3].

Using the unlimited available energy of the sun makes PV sustainable because no CO_2 is emitted while the power plant is operating. But how sustainable is the whole life cycle of a PV module? During the manufacturing process used resources and energy make an environmental impact. Most manufacturers try to make the module as cheap as possible, but sustainability and reliability in the material selection are not taken into account. Still, calculations for crystalline silicon modules show that already after 1-4 years [4, 5] the energy payback time is achieved and sustainable energy production is starting. Exact values depend on the local solar irradiation, nominal module power, and module technology. As nowadays the expected operating time of PV modules is more than 25 years, this emphasises the sustainability of PV [4].

Nevertheless, the end-of-life treatment is rarely considered in sustainability calculations, although the waste management needs to be considered in the environmental impact balance. Presently, the modules have to be taken back by the manufacturer who takes care of the disposal. As the amount of PV waste is still very low, no appropriate recycling technology is available for modules yet. As the number of PV modules reaching their end of life will increase significantly in the next years, real recycling strategies have to be developed for sustainability reasons. Additionally, large-scale recycling can also be reasonable economically in the future [6].

The reliability of most PV modules is good and especially the electrical degradation rates (the degradation of the modules' electrical performance) are low. PV modules consisting of crystalline silicon cells have a median degradation of 0.5%-0.6% per year [7]. However, infant or midlife failures can endanger the utilisation of PV modules until the end of the expected operating time. A worldwide study of 6.5 million inspected modules revealed that a third had detectable defects [8]. Failures can happen in different parts of a PV module (Fig. 1.1b). Though it is important to notice that a defect does not mean that the whole module is broken so it can stay in operation and produce electricity and often even does not endanger the electrical performance. Still the defects should not be left unintended.

To understand the parts where failures happen most often, Figure 1.1a presents the typical layer structure of a glass/backsheet PV Module. A module contains several solar cells, which are the active parts that transform light into electricity. In more than 90% of the PV modules on the global market, the cells are made of silicon. Hence, only such modules will be considered in the following. The cells are connected in series to a string to increase the voltage output. An encapsulant surrounds and protects the solar cells, often composed of ethylene-vinyl acetate copolymer (EVA). In the front, a specially designed solar glass is supporting the capture of solar radiation. On the backside a backsheet is protecting the active elements from environmental influences. Additionally, a frame (often aluminium) gives stability to the module. In the junction box, the cables are attached that connect several modules and lead the produced electricity to the inverter [9].

Manufacturers use different materials for the backsheet. Most common are either Tedlar backsheets, which have a polyethylene terephthalate (PET) core and Polyvinyl fluoride (PVF) outer layers, or Polyvinylidene difluoride (PVDF)/PET/PVDF backsheets. In recent years also multi-layered PET backsheets or PET-based backsheets with different protective layers (Polyamide (PA) or Polyolefine (PO)) were deployed. Additionally, some manufacturers used multi-layered PA backsheets for several years (2010-2015) [10].

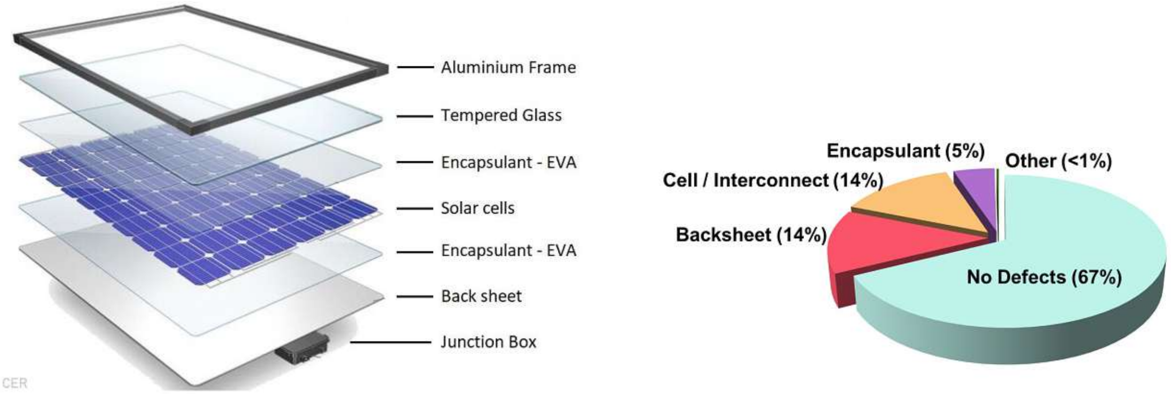

(a) Typical layer structure of a glass/backsheet module [9].

(b) Of defects affected PV parts according to a world-wide study by [8].

Figure 1.1: PV module structure and of defects affected PV module parts.

Figure 1.1b presents that cell/interconnection (14%) and backsheet (14%) related defects play the largest parts in the investigated modules [8] which is also approved by an internal study. Especially, the percentage of backsheet failures is growing within the last years [10, 11]. Here the backsheet materials and composition are an important factor for the modules reliability. After only four to six years in the field already two thirds of the PA backsheets develop some defects. Though also in around halve of the modules with PET or PVDF/PET/PVDF backsheets, defects could be detected after ten years. In the affected materials, typical backsheet failure types are discolouration and delamination. However, two thirds of the backsheet defects in all kind of materials are related to cracking [8, 12, 13]. Deeper cracks can either develop along busbars or in cell gaps. Moreover, microcracks can develop on the whole backsheet area (see Fig. 1.2) [10].


(a) Square cracks in the cell gaps [10]. (b) Longitudinal cracks along the busbars. (c) Microcracks.

Figure 1.2: Different crack types in polyamide (PA) backsheets.

Even though cracks can develop in various backsheet materials, polyamide is affected the most. Therefore, several investigations and research had focussed on this material. A detailed error analysis [10] revealed that several effects, happening at outdoor weathering, play together to result in the backsheet cracks. In the field, a module is exposed to daily and seasonal temperature changes. As the different materials in the module layers have varying thermal expansion coefficients this results in internal thermo-mechanical stress. As the busbars have a height of 200 µm, additional stress is induced there by this height difference. Therefore, deep longitudinal cracks develop in the PA backsheet along the busbars. They start from the airside and can develop so deep that only the encapsulant is left to protect the cells from the airside. In contrast, the square cracks in the cell gaps grow from the inside, i.e. the interface between encapsulant-backsheet. They are less common and only happen if special EVA types are used. Due to solar irradiation, this EVA degrades, forming acetic acid. This acid is degrading the PA material from inside which results in the squared cracks. Microcracks only affect the utmost PA-layer and develop randomly from higher stress levels [10].

As the cracks develop after a relatively short time in the field, the question arises why these failure modes were not detected at pretests. All PV modules need to pass certain tests before market introduction, which are given among others in the IEC 61215 [14]. Modules are tested with damp heat, thermal cycles, and artificial irradiance in climate chambers, but these climatic conditions were never applied simultaneously. Hence, the material did not degraded and no cracks evolved without the simultaneous thermo-mechanical load. Additionally, often environmental stresses expand the conditions in the test facilities [10].

Which problems do such backsheet cracks create? The longitudinal cracks along the busbars and the squared cracks in the cell gaps can grow through the whole backsheet. In this way, moisture can enter through the backsheet and only the encapsulant is left to protect the cells from the outside. This leads to degradations like corrosion of solder joints and metallisation, degradation or delamination of the encapsulant, or polymer hydrolysis. All this leads to a faster decrease in the module's electrical performance. On the other hand, the backsheet fails to protect the surrounding of the power generated in the solar cells. Due to the cracks it no longer acts as an electrical insulator and leakage currents can occur. Therefore, affected modules present a safety risk for people and animals. This can result in automatic disconnections of strings of affected modules by the inverter, which may lead to larger production losses in a solar park [12, 15].

Especially due to the safety risks, affected modules need to be replaced. This is economically and ecologically a problem. First, the module park owner faces outages during the replacing process and the module producer must take back the modules and deal with guarantee claims.

So this is quite an expensive procedure. New modules must be bought and installed and the old ones need to be disposed [15]. The production of the new module and also the disposal are additional impacts on the environment that should be avoided. Additionally, the confidence in the electricity production by PV could become compromised. Of course, for the future, the goal is to produce modules with more reliable compounds that survive longer outdoor weathering impacts in the field. Therefore, advanced tests need to be developed that simulate these conditions better.

But, what should be done with the millions of modules (alone 11-12 GW with PA-backsheets were installed in 2010-2015 [16]) which are already installed and have developed cracks already or will so in a short period of time? Thus, the scene was set for the birth of the idea to develop repair solutions for cracked backsheets to extend the operating time of affected modules. This was one of the largest parts of the PVRe^2 project [6].

PVRe^2 - Sustainable Photovoltaics

To make photovoltaics more sustainable the R&D project PVRe^2 (PV Repair and Recycling) was created. The goal was to find solutions to the above mentioned problems in the different areas of sustainability. One work package of the project aimed to improve the recycling processes of c-Silicon PV modules. As big amounts of waste will start to occur in the upcoming years and increase notably afterwards, it is definitely reasonable to develop recycling technologies for environmental and economic reasons. To go one step further, the goal of the project was to make the whole module more sustainable with materials that are better recyclable and have less impact on the environment, e.g. fluorine-free backsheets [6].

Another part of the project tried to develop repair possibilities for PV modules to increase the life span of defect modules. Earlier repair activities had been devoted only to broken cables, diodes, or inverters. Due to the above reported failures, which occur especially in the backsheets, the project team searched for suitable repair solutions. As polyamide backsheets are the most affected ones, first research focused on suitable solutions for these backsheets. In pre-analyses, it was found out that the squared cracks in the cell gaps are not repairable, as the damage is too heavy. But the much more common longitudinal cracks along the busbars and microcracks on the whole backsheet can be repaired indeed [12].

The first step in the development of the repair solution was the selection of materials that could durably fill and coat such cracks. A material used for the repair has to fulfill certain requirements. Most important, it has to take over the backsheets part of being an electrical insulator between the outside and the active PV parts. Moreover, it should be compatible with the backsheet material. So it should have similar thermal expansion coefficients, and no outgassing material should attack the backsheet. Furthermore, easy application onto the modules is required, preferable directly in the field to save logistic costs [12].

In a detailed analysis, different pre-treatment methods of the backsheet were tested and then 13 different repair solutions were applied on the modules' backsheets, for the first tests. They were either coatings, applied with a brush or a spray, or tapes or films that were adhered on the modules (see Tab. 1.1). Afterwards, several tests were done on all materials to investigate their compatibility. First, the adhesion was tested with a tape peel test and a scratch test, which some materials did not pass. Then cross-sections were cut out of the modules and analysed with a microscope to investigate the crack filling and coating thickness. It was found out that the tape-based solutions gave some protection over the whole backsheet but the cracks were not filled. Therefore, these solutions are not suitable for deep longitudinal cracks because the insulation properties are not regained. Nevertheless, they can be used for the repair of local failures on a small part of the module only. For the coating-based solutions, also the influence of the viscosity of the coating was investigated to get optimal conditions in the crack filling and coating handling [12].

Table 1.1: Overview of repair materials (Abbreviations: 1-K: 1 component; 2-K: 2 components system; RT: room temperature).

Sample ID	Application type	Material type	Solvent	Curing	Tape peel test	Scratch test	Crack filling	further testing
Re01	Brush-coating	Epoxy	Yes	1-K, RT	✓	✓	optimised	✓
Re02	Brush-coating	Polyurethane	Yes	2-K, RT	✓	✓	optimised	-
Re03	Brush-coating	Polyurethane	Yes	2-K, RT	✓	✓	✓	✓
Re04	Brush-coating	Acrylate	No	1-K, UV, RT	✓	Chipping	-	-
Re05	Brush-coating	Silicone	No	1-K, RT	✓	✓	✓	✓
Re06	Brush-coating	Epoxy	No	2-K,RT	✓	✓	-	-
Re07	Brush-coating	Epoxy	No	2-K,RT	✓	Chipping	-	-
Re08	Spray coating	Nitrile rubber	Yes	1-K,RT	✓	✓	✓	
Re09	Spray coating	Liquid rubber	Yes	1-K,RT	✓	✓	✓	✓
Re10	Tape/film	PU+Acrylate	No	RT	✓	✓	-	✓
Re11	Tape/film	PVC+Acrylate	No	RT	✓	✓	-	✓
Re12	Tape/film	TPT+Adhesive	No	RT	-	-	-	-
Re13	Tape/film	PET + EVA	No	RT	-	-	-	-

After the pretests were finished, the remaining four suitable coating materials and two adhesive tape solutions were applied to modules with microcracks. Some were directly coated in the field without dismantling and the material was monitored there every six months. Others were coated in the laboratory with the backsheet facing upward. They were then subjected to artificial weathering in the laboratory for accelerated testing. Here damp-heat, temperature cycles, and dynamical mechanical load were applied (tests according to IEC 61215 [14]). Additionally, economic calculations were done to know the material costs for each repaired module, which resulted in 1 to 3 Euros. Also the coating time was calculated to be around 10 minutes per module. With these values, economic estimations could be done to compare if the repair process pays off. In addition, one needs to know how much the coating is prolonging the modules' life time, which is not known yet [12].

After the coated modules were exposed to natural weathering in the field for twelve months, the different coating solutions were analysed. The same was done for the modules facing artificial weathering. The visual appearance, the crack propagation, chemical degradation, adhesion, and color change of the coating materials were analysed in detail. Moreover, the electrical power of the modules was measured. For all repair solutions, the electrical power did not change and the crack propagation was stopped or delayed. However, chemical degradation, inefficient adhesion or demanding handling at the coating process lead to only two materials with satisfactory results which were then used for further optimisations and testing [16].

The two-component polyurethane-based coating and an optimised flowable silicone-based coating were applied on modules with deeper longitudinal backsheet cracks. Here it was important that the collapsed insulation resistance was restored by the coatings. The first six modules were coated directly in the field without dismantling. First tests showed that the insulation resistance was restored. As the handling of the direct coating of the mounted modules was difficult, dismantling of the modules for the repair process was recommended for the future [16].

Monitoring of the Coated Modules

Additionally, twelve modules with polyamide backsheets with deeper longitudinal cracks were coated with the two most promising coatings (polyurethane- and silicone-based) in the laboratory. As these coatings showed good results on modules with microcracks after twelve months of natural weathering and artificial weathering, the coating stability on modules with deeper longitudinal cracks should be monitored in detail. This is where my contribution comes into play.

1.1 Research Aim and Research Question

The general research objective of my thesis is to examine the life-prolonging effect of the repair coatings. Modules with deep cracks would otherwise be disposed and exchanged due to safety reasons.

For this purpose, I built and programmed a monitoring system to analyse the coated backsheets over years of natural weathering in the field. Main parameters of interest are the electrical performance of the coated modules and the stability of the coatings on the backsheet. Based on these objectives and the identified knowledge gap, the following research questions were phrased:

- Electrical performance
    Is the coating affecting the electrical power and insulation resistance of the modules?
    How does the electrical performance of the modules change over time?
- Material stability of the repair coating
    After what time in the field is the coating changing visually?
    Is the coating chemically stable over time or does it change, and if so, how?
    Does the adhesion of the coating on the backsheet material change over time?
- How long can the operating time of a module with a cracked backsheet be extended by the repair coating?

Chapter 2

Theory

2.1 Photovoltaics

The work of this thesis is related to the generation of energy by photovoltaics. For a better understanding of the physical principles of this kind of energy generation, the basic working principles of solar cells will be explained in the following section.

2.1.1 Semiconductor Properties

Semiconductors are the basic material used in solar cells. They can either be elemental materials, for example silicon (Si) or germanium (Ge), or compound materials like gallium arsenide (GaAs) or cadmium telluride (CdTe). The semiconductors are arranged in a crystalline lattice with a covalent bonding. In such solid-state materials, the energy states of the electrons of the involved atoms form energy bands due to their interaction. The electrons fill up the energy bands starting with the ones with the lowest energies according to the Pauli principle [17]. At zero Kelvin all bands are filled up to the Fermi level, E_F. The last filled band is called the valence band E_v; the one above the conduction band E_c. The energy distance in between these two bands constitutes the bandgap $E_g = E_c - E_v$. In semiconductors at $T = 0\,\mathrm{K}$, the Fermi level lies in the middle of this band gap [17]. At higher temperatures some electrons have an energy higher than the bandgap, so they can move to the conduction band. In semiconductors the bandgap is smaller (e.g. 1.1 eV for Si and 1.4 eV for GaAs at room temperature) than in an insulator. Therefore, an electron can move to the conduction band already at room temperature due to thermal excitation. There it can move freely and contribute to the conductivity of the material. This explains why the conductivity increases with increasing temperature in semiconductors [17, 18].

An electron transferred to the conduction band leaves an empty place in the valence band. This is called a *hole* and can be seen as a positive charge carrier. The electron density in the conduction band, n, and the hole density in the valance band, p, are given by [19]

$$n = N_c \cdot e^{\frac{E_F - E_c}{kT}} \tag{2.1}$$

$$p = N_v \cdot e^{\frac{E_v - E_F}{kT}} \tag{2.2}$$

with the density of states in the conduction/valence band N_c/N_v, the Boltzmann constant k and the temperature T. Their product is defined by the bandgap:

$$np = n_i^2 = N_c N_v \cdot e^{\frac{E_v - E_c}{kT}} = N_c N_v \cdot e^{\frac{-E_g}{kT}} \tag{2.3}$$

In pure (intrinsic) semiconductors the electron density in the conduction band is equal to the hole density in the valence band $n = p = n_i$ (n_i is the so-called intrinsic carrier concentration) [19].

The band structure of semiconductors can be explained by energy-momentum diagrams (see Fig. 2.1). The electrons in the conduction band and the holes in the valence band can be interpreted as free-moving charge carriers using the effective mass m^*. This proxy quantity accounts for the fact that electrons or holes may undergo changes in their potential energy, not only in their kinetic energy, when moving through a lattice. The kinetic energy of a charged particle then becomes [17]

$$E_\mathrm{n}(\boldsymbol{k}) = E_\mathrm{g} + \frac{\hbar^2}{2m_\mathrm{e}^*}\left(\boldsymbol{k} - \boldsymbol{k}_{01}\right)^2, \tag{2.4}$$

$$E_\mathrm{p}(\boldsymbol{k}) = \frac{\hbar^2}{2m_\mathrm{p}^*}\left(\boldsymbol{k} - \boldsymbol{k}_{02}\right)^2, \tag{2.5}$$

with the reduced Planck constant, $\hbar$, and $\boldsymbol{k}$ representing the electron's wave vector (letters in bold face denote vectors). Here zero energy is set to the upper limit of the valence band. $\boldsymbol{k}_{01}$ is the wave vector at the minimum of the energy parable at the conduction band and $\boldsymbol{k}_{02}$ at the maximum of $E(\boldsymbol{k})$ in the valence band.

The effective mass is a tensor due to the directional dependence of the potential

$$m^* = \frac{\hbar^2}{\left(\frac{\mathrm{d}^2E}{\mathrm{d}k_i\mathrm{d}k_j}\right)}. \tag{2.6}$$

with $(i, j = x, y, z)$. Here, the energy bands (potential energy) are approximated by parables. Because the energy of the valence band is bent downwards, the effective mass of a hole is negative [17].

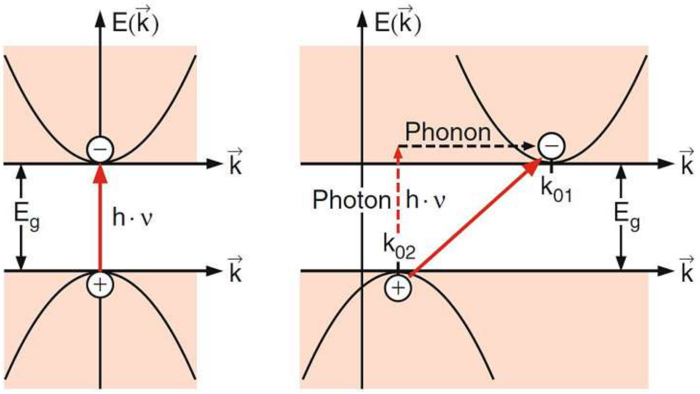

Figure 2.1: One-dimensional display of the semiconductor band structure in an energy momentum diagram. The transition of an electron to the conduction band in a direct (left) and indirect (right) semiconductor [17].

In Fig. 2.1, the difference between direct (GaAs) and indirect (Si) semiconductors becomes obvious. If a photon is absorbed by the semiconductor (which will be explained in more detail later on), an electron is transferred to the conduction band. This transition is more probable if the minimum of the parable in the conduction band lies directly over the maximum of the parable of the valence band so no change in $\boldsymbol{k}$ is necessary. This is the case in so-called direct semiconductors. In indirect semiconductors the maxima are not directly above each other ($\boldsymbol{k}_{01} \neq \boldsymbol{k}_{02}$) so a photon and a phonon - lattice vibration (for the $\boldsymbol{k}$ transition) are needed. This explains why in indirect semiconductors transitions are less probable. In application, this means that solar cells of indirect semiconductors have to be much thicker than the ones of direct semiconductors because a photon has to enter deeper into the material until an absorption is happening [17].

Doping of Semiconductors

To increase the conductivity of a semiconductor, it is doped with impurities. Taking silicon (Si) as an example, it has four valence electrons which are all covalently bonded to their nearest neighbouring atoms. If atoms with five valence electrons (like phosphorus) are inserted into this lattice, one electron is not bonded strongly because it has no place in the covalent bondings. Therefore, it can be removed easily and can be looked at as a free electron moving through the lattice. So much less energy is needed to transfer this electron into the conduction band. As now much more electrons are available than holes, such a semiconductor is called n-type semiconductor, and the electrons are the majority carriers (holes are minority carriers). The impurities (here phosphorus) with more electrons than the lattice atoms are called donors N_D. The energy levels of the donors lie a little below the lower border of the conduction band of the semiconductor (see Fig. 2.2a). Therefore, the Fermi energy is raised in an n-type semiconductor: by replacing n with N_D in Equation 2.1, the gap from the Fermi energy to the conduction band now becomes [17, 19]:

$$E_F - E_c = kTln\left(\frac{N_D}{N_c}\right). \tag{2.7}$$

The second possibility of doping is with atoms with three valence electrons (acceptors), like boron. Here a place in the covalent bonding stays free which is positively charged and can easily capture electrons. In such p-type semiconductors, holes are the majority carriers. The acceptors' N_A energy levels lie a bit above the valence band and the Fermi energy is lowered (see Fig. 2.2b). So the gap is calculated to be:

$$E_v - E_F = kTln\left(\frac{N_A}{N_v}\right) \tag{2.8}$$

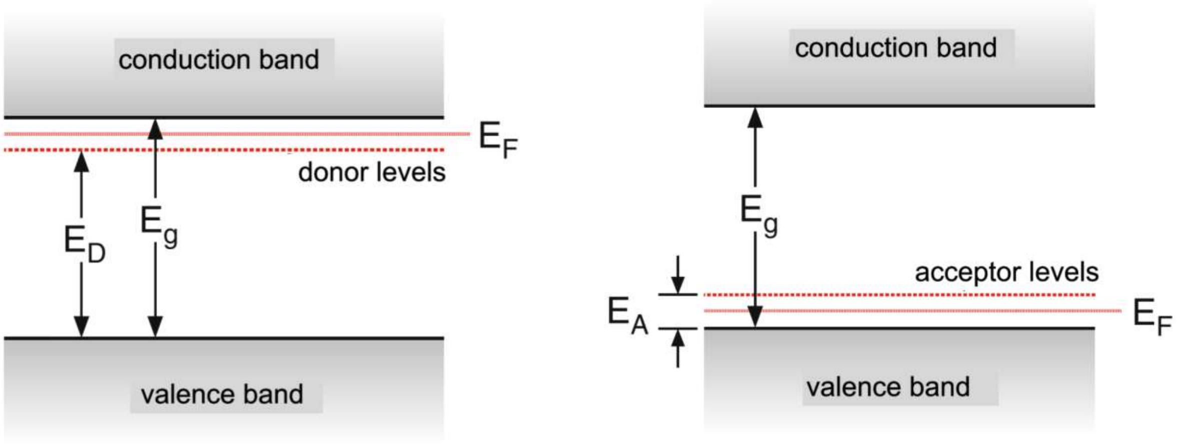

(a) N-type semiconductor with donors' energy levels. (b) P-type semiconductor with acceptors' energy levels.

Figure 2.2: Band structure of doped semiconductor, modified from [17].

Does the imbalance of majority carriers in doped semiconductors effect their electric charge? No, because due to the doping with acceptors also less positive charged nuclei exist. So overall the semiconductor is neutral. The same accounts for n-type semiconductors, which have more positive charged nuclei to compensate the additional electrons [19].

2.1.2 Generation and Recombination

A constitutional principle of semiconductors is the Electron-Hole Pair (EHP) generation. In a thermal equilibrium the generation of EHPs is equal to their recombination, so the carrier density stays the same: $np = n_i^2$. The possible generation and recombination processes will be discussed in the following. In solar cells, the semiconductor is under illumination, which is a non-equilibrium state. This special process will be discussed in Section 2.1.5.

Generation Processes

Different processes can generate electrons which are then moved into the conduction band, where they can act as free carriers. Thermal generation was already discussed and happens at all temperatures above 0 K. Here the energy for the transition of the electron comes from phonons interacting with the host atom. Besides phonons also incoming photons can generate EHPs, which is called photogeneration. It is the main mechanism in solar cells. An incoming photon transfers its energy to an electron and moves it to the conduction band if this energy is higher than the bandgap. The principle behind is the photoelectric effect [18].

The photoelectric effect describes that an absorbed photon gives its total energy to an electron of the absorbing material. The achieved kinetic energy of the electron only depends on the frequency of the photon ν and not on the intensity of the incoming light. It is described by $E_{kin}^{max} = h \cdot \nu - W_a$. With the Planck constant h and the work function W_a, which is the work needed to separate an electron from a metal (or semiconductor) where it was bonded. In semiconductor technology, it explains why only light above a certain frequency can move electrons into the conduction band. The intensity of the incoming light only influences the number of electrons transferred into the conduction band [17].

The transition to the conduction band (through photons or phonons) can either happen over the whole bandgap or with the help of impurities, which is then called impurity-mediated generation. As impurities have energy states within the bandgap, the energy needed for the transition is lower than for pure semiconductors [18].

Recombination Processes

Recombination of charges is the opposite process of generation and is important to keep the thermal equilibrium. Again different processes are possible (see Fig. 2.3): The first one is radiative recombination, where an EHP recombines over the whole bandgap which leads to photon emission with a frequency corresponding to the bandgap's energy. It is the ultimate physical limit of the efficiency of solar cells for direct-bandgap semiconductors. In reality (and also for indirect semiconductors) other recombination effects limit this efficiency. This is mostly the non-radiative (Shockley-Read-Hall) recombination. Due to impurities (intentionally from doping or unintentionally) so-called trap-states for both electrons and holes develop in the middle of the bandgap. There they can recombine and the energy is emitted through a phonon. Especially at surface areas or at boundaries many of these traps exist due to unpassivated bonds. In indirect semiconductors also Auger recombination is typical [18]. Here two electrons collide in the conduction band, which leads to one electron recombining with a hole and the other one gaining more kinetic energy from the collision. This kinetic energy is emitted through phonons and the electron returns to the border of the conduction band [18].

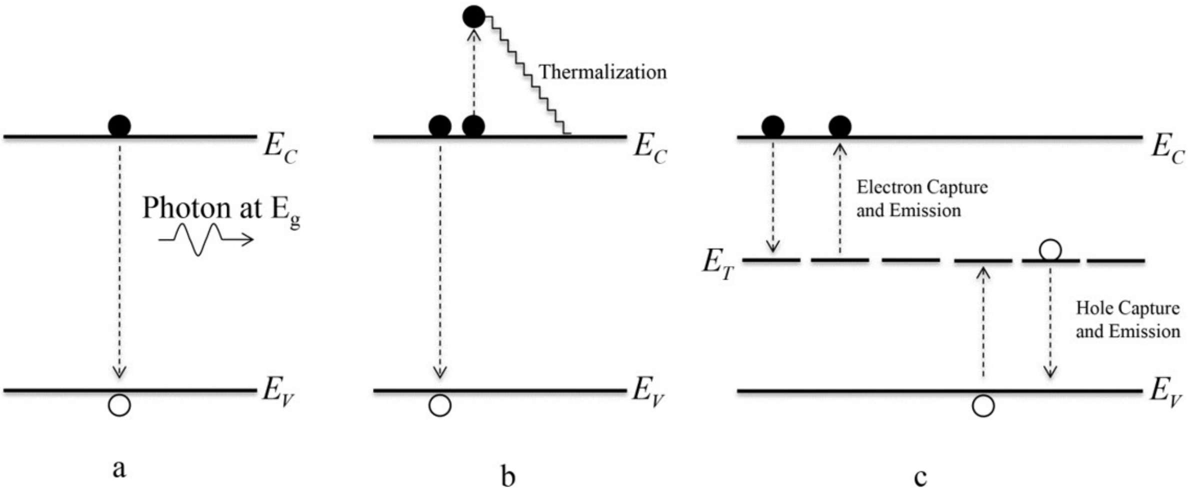

Figure 2.3: Recombination processes: (a) radiative recombination over the whole bandgap; (b) Auger recombination; (c) non-radiated (Shockley-Read-Hall) recombination [18].

2.1.3 Carrier Transport in Semiconductors

In a pure semiconductor charged carriers (electrons or holes) experience a force when an electric field $\boldsymbol{E}$ is applied. The free electrons in the conduction band drift to the positive electrode (anti-parallel to the electric field). Even the electrons in the valence band can drift if holes (free places) are available which can be used by the electrons. This can be interpreted as a drift of the holes parallel to the electrical field. Both parts lead to a drift current with the current density $\boldsymbol{j} = \sigma_{el} \cdot \boldsymbol{E}$, with the electrical conductivity σ_{el} of the semiconductor. It depends on the charge density $n \cdot q$ or $p \cdot q$ (with the electron charge q) and the mobility $\mu_n = \frac{q \cdot \tau_n}{m_n^*}$ or $\mu_p \frac{q \cdot \tau_p}{m_p^*}$ respectively. Here τ_n, τ_p is the average time between two collisions of electrons in the conduction or valence band [17]. As the electrons in the valence band only have p holes where they can move to, their mobility is much lower than the one for the electrons in the nearly empty conduction band. The total conductivity is temperature dependent because the carrier density increases exponentially with rising temperature (because more electrons move to the conduction band). The slight mobility decrease due to a shorter scattering time $\tau_{n,p}$ does not have a large effect. Overall, the drift current can be expressed as:

$$\boldsymbol{j}_{drift} = \boldsymbol{j}_n + \boldsymbol{j}_p = (n \cdot q \cdot \mu_n + p \cdot q \cdot \mu_p)\boldsymbol{E} = (n \cdot q\frac{q \cdot \tau_n}{m_n^*} + p \cdot q\frac{q \cdot \tau_p}{m_p^*})\boldsymbol{E}. \tag{2.9}$$

In doped semiconductors, the carrier density n (n-type) or p (p-type) is higher. This also influences the conductivity and is called *impurity conduction*. It occurs already at lower energies because the donor electrons move to the conduction band before the electrons from the valence band do [17, 18].

Moreover, diffusion current occurs in a semiconductor when a concentration gradient of carriers exist (which we will see later). Due to the random thermal motion, particles will always move to regions with lower concentrations. This is explained by Fick's First Law of Diffusion, which is true for any kind of mass flux. If the particles are charge carriers (like the electrons and holes) their diffusion results in a diffusion current:

$$\boldsymbol{j}_{diff} = \boldsymbol{j}_n + \boldsymbol{j}_p = qD_n\nabla n - qD_p\nabla p \tag{2.10}$$

It states that the diffusion current $\boldsymbol{j}_{diff}$ is proportional to the concentration gradient ∇n and

∇p. D_n and D_p are the diffusion coefficients which are related to the mobility according to the Einstein relationship: $D_{n,p} = \mu_{n,p}\frac{kT}{q}$ [18].

2.1.4 PN-Junctions

The functionality of a solar cell, and also many other semiconductor applications, is based on the presence of a pn-junction. Here an n-type semiconductor is brought in contact with a p-type semiconductor of the same lattice material. In the contact area, a large carrier imbalance emerges. In the n-type region, more electrons exist than in the p-type region, so they move to the area with lower concentrations. The same happens with holes in the other direction. This leaves uncompensated ionised donors on the n-side and acceptors on the p-side, which lead to a fixed charge on both sides in the so-called space charge region (or depletion region W_{dp}). This charge generates an electric field and consequently a drift current of the charge carriers. The drift current compensates the diffusion current and leads to an equilibrium [18].

Figure 2.4 presents the band diagram of a pn-junction. The Fermi level needs to be equal on both sides, so the conduction band and the valence band bend in the space charge region and form a potential barrier. It is denoted as V_{pn} (and also called built-in voltage) and can be calculated as the energy difference of the bandgap reduced by that of the gap to the Fermi level on the n-side $E_c - E_F$ and p-side $E_F - E_v$:

$$qV_{pn} = E_g - (E_c - E_F) - (E_F - E_v) = E_g - kTln\left(\frac{N_cN_v}{N_AN_D}\right) \tag{2.11}$$

using Equation 2.7 and 2.8. Moreover, Equation 2.3 can be used to write the voltage with the donor, acceptor and intrinsic density:

$$V_{pn} = \frac{kT}{q}ln\left(\frac{N_AN_D}{n_i^2}\right). \tag{2.12}$$

Equation 2.12 shows that the built-in voltage V_{pn} depends on the donor and acceptor density [18, 19].

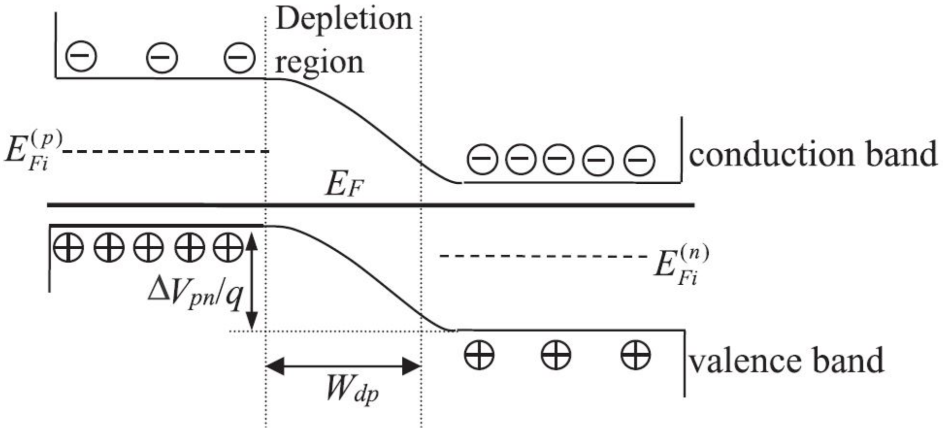

Figure 2.4: PN-junction with the aligned Fermi level [20].

An external voltage V_a applied on the pn-junction modifies the built-in voltage. If the positive pole is connected to the p-side, the built-in voltage is reduced: $V_{pn} - V_a$. It is assumed that the whole voltage applied drops in the space charge region, and the area beyond is quasi neutral. The built-in electric field does not change, nor does the drift current. But a high

diffusion current starts because more majority carriers can negotiate the potential barrier. This leads to an exponential increase of the current [18, 19].
If the voltage is applied to the n-side, the potential barrier increases. This eliminates the diffusion current and only minority carriers can contribute with a low drift current. This leads to a typical diode current characteristic presented in Figure 2.5a. If an ideal pn-junction is assumed, with quasi-neutrality (all voltage is dropped across the junction) and no mobile carriers present inside the depletion region, the applied voltage only changes the minority carrier distribution. So from the minority carrier diffusion equation (2.10) the ideal diode equation can be derived using an exponential ansatz (see [18, 19]):

$$j(V) = qn_i^2 \left[\frac{D_n}{N_A L_n} + \frac{D_p}{N_D L_p} \right] \left(e^{qV/kT} - 1 \right) = j_{0,diff} \left(e^{qV/kT} - 1 \right). \tag{2.13}$$

This equation describes the ideal current-voltage characteristic with the saturation current density $j_{0,diff}$ depending on the diffusion length $L_{n,p}$ (the average path length of a charge carrier before recombination). In reality, not all assumptions made are valid for solar cells, so a more complex equation is necessary to describe the current-voltage behaviour of solar cells (which can be found in [18, 19]).

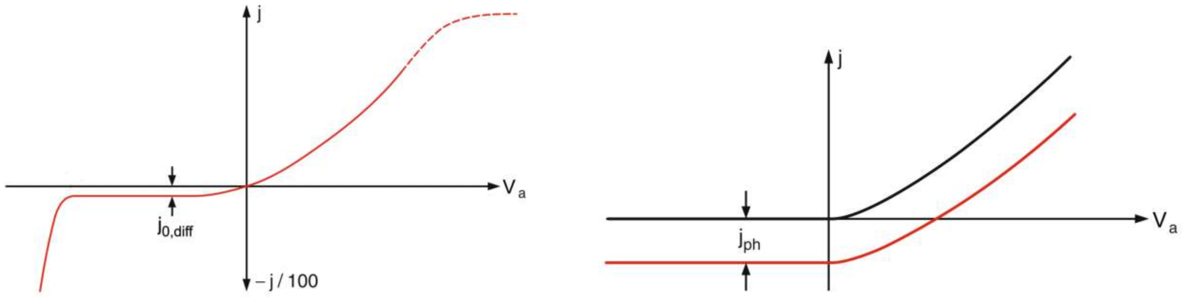

(a) Ideal diode characteristic with the small negative saturation current $-j_{0,diff}$ in the reversed biased part.

(b) Part of the diode characteristic of an irradiated diode.

Figure 2.5: Diode characteristics, modified from [17].

2.1.5 Solar Cells

A solar cell is a pn-junction with a large surface area. In the practice, the n-type semiconductor often faces the sun and the p-type layer is located on the backside. If the solar cell is irradiated by the sun, photons are absorbed. As described in Section 2.1.2, an absorbed photon with enough energy can move an electron into the conduction band and generate an electron-hole pair. So the density of holes in the valence band and of electrons in the conduction band increases which changes the built-in voltage on the pn-junction and reduces the potential barrier. The electricity production in the solar cell can be explained by the photovoltaic effect. If an EHP is generated in the space charge region, the electron is moved to the n-side and the hole to the p-side due to the internal electrical field. The same happens for the minority carriers if they are generated near the space charge region and diffuse to the border of this region. The majority carriers, however, are rejected by the internal field and the electrons stay at the n-side and holes at the p-side. This leads to the fact that the n-side gets negatively charged and the p-side positively, so an external electric field arises compensating the internal field. The external field can never become higher than the internal one, so the maximum voltage achievable by a solar cell (the open circuit voltage) is equal to the built-in voltage V_{pn}. If the n-side and the p-side are connected over a resistor, the carriers move over the external circuit and a current flows. This is called the photocurrent I_{ph} which reduces the diode current (see Fig. 2.5b). The diode equation (2.13) for the current density, j changes to:

$$j = j_{0,diff}\left(e^{qV/kT} - 1\right) - j_{ph}. \tag{2.14}$$

For an optimal function of the solar cell, the resistance must be chosen such, that the power becomes maximal. In the official electrical notation, the current of the solar cell is negative because it is produced by the cell and delivers energy into the circuit (see Fig. 2.5b). In the solar cell community however, the IV curve is plotted with a positive current [17, 21].

2.2 Spectroscopy

To characterise the chemical stability of the coating material on the backsheets, vibrational spectroscopic methods were used. These methods are common in the chemical analysis of polymers either for material identification or to detect material degradation. Hence, they are also applied in the PV sector for a detailed analysis of the polymer components of PV modules in product development, for quality assurance in the manufacturing process or for failure detection. This section will give an overview of the physical principles of vibrational spectroscopy. Then it will stress out the differences between infrared (IR), near-infrared (NIR), and Raman spectroscopy and the respective devices, as they were all used in this thesis.

2.2.1 Physical Principles

The basic principle of spectroscopy relies on the interaction between electromagnetic waves and matter. The relevant part of the electromagnetic spectrum extends from the long-wavelengths, low-energy radio waves to γ-rays with short wavelengths and consequently high energy (see Fig. 2.6). Depending on the wavelength of the incoming wave it interacts with different levels of the radiated matter. Of the various interactions, we are here interested in the structures of organic/polymer molecules which can be identified by their molecular vibrations. These can be exited and hence detected by light in the infrared range [22, 23].

The fundamental principle of matter-wave interactions is that a photon (with frequency ν) that is absorbed by an atom or molecule can put this atom/molecule in a higher energy state E_i if the energy conservation law is fulfilled: $E_i - E_k = h \cdot \nu_{ik}$. Here h is the Planck-constant. This shows that only specific frequencies can be absorbed by a specific atom or molecule which can be detected and recorded in a spectrum. However, not all the frequencies which are possible due to the energy conversion law are *allowed*, so further relations have to be considered for the absorption process. Besides the energy, also the conservation of the angular momentum and principles of symmetry need to be fulfilled. These rules give the conditions for the selection rules to a higher energy state. They can be derived from the time dependent Schrödinger equation which is beyond the scope of my thesis but can be found in [17]. Here only the selection rules for the molecular vibrations will be considered in the following [17, 23].

To aid intuition, let us go back to classic mechanics. The vibration of a simple molecule consisting of two atoms can be explained by the model of a harmonic oscillator. In a classic mechanic's model, the atoms having the masses m_1, m_2 are linked via a spring. During the oscillation, potential and kinetic energy are constantly transferred into each other. The frequency of this oscillation can be derived from a differential equation to $\nu = \frac{1}{2\pi}\sqrt{\frac{f}{\mu}}$ with the reduced mass $\mu = \frac{m_1 m_2}{m_1 + m_2}$ of the two atoms and the strength of the bond f. This shows already how the

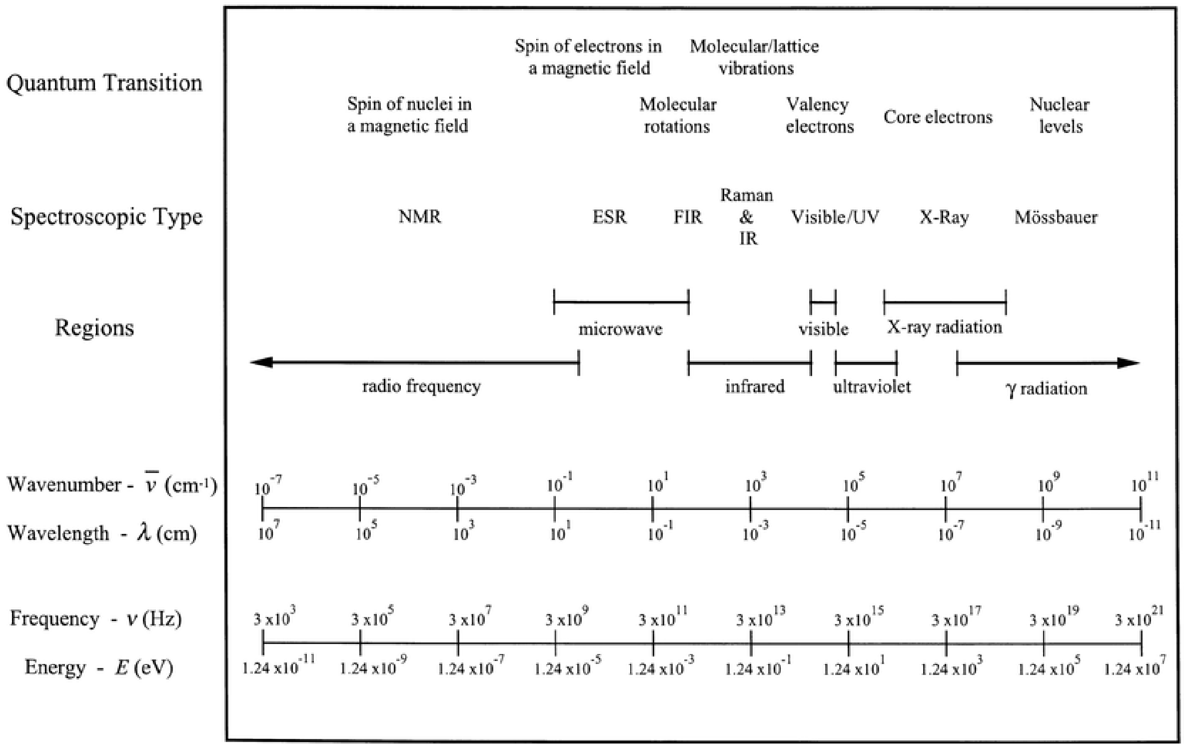

Figure 2.6: Correspondence of quantum transitions with parts of the electromagnetic spectrum [24].

vibrational frequency depends on the atoms' masses and their bonding force of the investigated molecules and makes clear that they can give unique information about these structures [23].

For a more exact explanation of the motion of a molecule, a quantum mechanical explanation is required. Again the harmonic oscillator describes the system at the start. Hence, now the Schrödinger equation is used:

$$-\frac{\hbar}{2m}\frac{\mathrm{d}^2\psi}{\mathrm{d}x^2}+V(x)\psi=E\psi \tag{2.15}$$

with the reduced Planck-constant $\hbar$, the harmonic potential $V(x)$ and the wave function ψ. Now the energy levels of the **harmonic oscillator** can be derived to [17]

$$E=\hbar\omega\left(v+\frac{1}{2}\right)=h\nu\left(v+\frac{1}{2}\right). \tag{2.16}$$

Here the vibrational quantum number v is an integer and the energy levels are equidistant. For a transition into a higher energy level the selection rule for the vibrational quantum number of $\Delta v=\pm1$ appertains. For a complex organic molecule, the description with a harmonic oscillator is not fitting except for small deflections, because the attractive force in a molecule is not proportional to the distance between the atoms. When the atoms are getting too close to each other, repulsive forces have an effect and, thus, have to be taken into account. Additionally, when the atoms are too far away and over a certain spatial limit (the dissociation energy E_D) the bond breaks. Hence, the potential energy is better described by a Morse potential (see Fig. 2.7), although it is still not fitting perfectly. The advantage is, that again the Schrödinger equation can be solved and the energy of the vibrational levels calculated to

$$E_{\mathrm{vib}}(v)=\hbar\omega\left(v+\frac{1}{2}\right)-\frac{\hbar^2\omega^2}{4E_{\mathrm{D}}}\left(v+\frac{1}{2}\right)^2. \tag{2.17}$$

The differences between the energy levels are now no longer equidistant but decrease with increasing quantum numbers. Moreover, the selection rules change, and in an **anharmonic oscillator** transitions also to higher energy states are possible: $\Delta v = \pm 1, 2, 3, \ldots$. These vibrations to higher levels are called overtones of the corresponding ground transitions [17, 23].

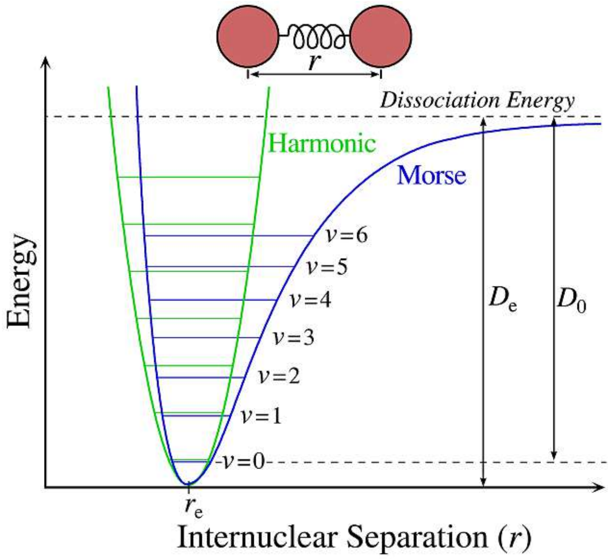

Figure 2.7: Morse potential of a two atomic molecule in comparison with the harmonic potential and their respective energy states [25].

Molecules are not only vibrating but also rotating. So the rotation has an impact on the vibrational energy levels too. In a first step, this motion is explained by a rigid rotator. The rotational energy is $E_{\text{rot}} = \frac{1}{2}I\omega^2$ with the angular velocity ω, the moment of inertia $I = m_1 r_1^2 + m_2 r_2^2 = \mu r^2$. Again the energy eigenvalues can be derived from the Schrödinger equation to:

$$E_{rot} = \frac{\hbar^2}{2I} J(J+1) \tag{2.18}$$

with the rotational quantum number J. For the transitions to a different energy level the selection rule is $\Delta J = (0), \pm 1$ (here $J = 0$ to $J = 0$ is not permitted). For a rotation only (without vibration), this transition requires energy with wavelength in the micrometer range [17, 23].

A molecule can now be explained as a rotating oscillator because it is rotating and vibrating at the same time. The vibration frequency is higher than the rotation frequency, so during one rotation, the molecule is vibrating 10-100 times. Hence, the atoms' distance depends on the vibration state which is therefore influencing the moment of inertia and the energy levels. Hence, new selection rules pertain: $\Delta J = (0), \pm 1$ and $\Delta v = \pm 0, 1, 2, 3, \ldots$ [23].

A molecule with more than two atoms can execute several vibrations. Every atom has three degrees of freedom. In total, the molecule (with N atoms) has 3N-6 vibrational degrees of freedom (normal modes) because three are substituted for the translation and three for the rotation of the molecule. An exception are linear molecules because they only have two possibilities for rotation so 3N-5 are left for the vibration. The normal modes can be used as a coordinate system, where the coordinate Q_i gives the deflection of the atoms into the direction of the i-th normal vibration. In a quantum mechanic model, the single normal modes can be explained as vibrations in a harmonic oscillator. This is of course only true for small deflections because around the minimum the anharmonic potential corresponds to the harmonic potential (visible in Fig. 2.7). This simplifies the overall vibrational energy to $E_{\text{vib}} = \sum_i \hbar\omega_i \left(v_i + \frac{d_i}{2}\right)$ with

the vibrational quantum number of the i-th normal mode v_i and the degree of degeneracy d_i originating from vibrations with the same vibrational frequencies. When considering polymers consisting of many atoms, a lot of vibrations should be possible. However, as in the polymer structure several groups are repeating, this leads to a redundancy of vibrations. Hence, the spectra of polymers are not overcrowded with bands [22, 23].
The basic principles of vibrational spectroscopy are the same for all different techniques but still, considerable differences can be found in the excitation process, spectra range, and the setup of the used instruments. These differences will be explained in the following.

2.2.2 Infrared Spectroscopy

Infrared (IR) spectroscopy is based on the absorption of electromagnetic radiation in the mid IR region by matter (molecules). Each bonding between two atoms in a molecule makes a unique potential depending on the masses of the atoms and their distance. Moreover, the atoms are always oscillating (in the ground level) which can result in the movement of electrical charge if the atoms' charge is not distributed symmetrically or gets asymmetrically through the oscillation. This charge movement results in a dipole moment [23].

If IR radiation is interacting with the molecule of interest, vibrations that fit certain frequencies can be exited. This means the affected molecule parts are put into a higher vibrational energy level. However, for IR radiation this is only possible if the dipole moment p_{el} is changing through this absorption process. Which results in the condition $\dfrac{\partial p_{el}}{\partial Q} \neq 0$ for a possible transition in the normal coordinates of a molecule Q. Therefore, IR spectroscopy is sensitive to asymmetric vibrations of polar groups in a molecule [17, 22].

This condition and the selection rules derived in the section before, result in a unique infrared spectrum for each material. The material is irradiated with the whole mid-infrared range from 2.5 - 25 µm wavelength (4000 - 400 cm^{-1} wavenumber) with a suitable light source. At the frequencies/wavelengths where a transition is possible, light gets absorbed. Functional groups in molecules often have characteristic vibrations in a certain range of the IR spectra. So these functional groups can easily be detected [22].

Normally, the spectra are measured in transmission mode, $T = \frac{I}{I_0}$, meaning the ratio of the transmitted light through the material I and the incident light I_0. The x-axis' unit of the spectra is often given in wavenumber $\tilde{\nu} = \frac{1}{\lambda} = \frac{\nu}{c}$ because it is proportional to the frequency and hence also to the energy of the electromagnetic wave. Besides the qualitative analysis of an IR spectrum, also quantitative analyses are possible due to Lambert-Beer's law [23]: $I = I_0 e^{-\alpha(\nu) l}$ with the sample thickness l and the absorption coefficient α which depends on the frequency and the concentration of the material. It can also be written with the decadic logarithm $log(I) - log(I_0) = -a \cdot c \cdot l$ with a concentration-independent decadic absorption coefficient of the species a and the concentration c. For quantitative spectra analysis, the absorbance $A = -log(\frac{I}{I_0}) = a \cdot c \cdot l$ is given on the y-axis because A is direct proportional to the concentration. In a material with several absorbing species at the same frequency/wavenumber, the concentration of one species can be determined if the other concentrations are known [23].

For IR measurements in transmission mode, the sample needs to be prepared manually as a thin layer 20 - 50 µm (=bulk measurement). To avoid time-consuming sample preparation, alternatively, the attenuated total reflection (ATR) technique is often used in practice. Here the probe consists of a crystal with a high refraction index. If it is brought in close contact with the sample surface, which has a lower refraction index, the radiation reflects on the interface due to internal total reflection. However, an evanescent wave penetrates some wavelengths into the sample. Because the intensity of the radiation decreases exponentially in the optically thinner medium (the sample), this automatically provides a sample thickness of 0.5 - 3.0 µm (=surface sensitive measurement) [22, 23].

IR Spectrometer

A spectrometer is composed of the main parts: (i) IR source, (ii) wavelength selector, (iii) the sample cell, (iv) a detector, and (v) a data analysis tool. Nowadays, mostly Fourier-transformation infrared (FTIR) spectrometers with a Michelson interferometer are on the market. Figure 2.8 presents the most important parts of an FTIR spectrometer. A thermal radiation source is used which can be of different materials depending on the IR region. For mid-infrared mostly a globar made of silicon carbide (SiC) is utilized [23].

Then a semi-transparent mirror splits the polychromatic beam. The first part is reflected by a stationary mirror and the second one by a moving mirror. Depending on the distance of the second mirror specific wavelengths undergo constructive interference. As the mirror moves, all wavelengths get scanned. The recombined beam is sent through the sample, often several times when mirror optics are used [23].

The detector transfers the beam into a time-depending signal, which is proportional to the interference intensity. Thermal detectors using the pyroelectrical effect are common, for example deuterated triglycine sulfate detectors (DTSD). Another possibility are photo detectors. They work on the same principle described for solar cells in Section 2.1. In the mid IR range mercury cadmium telluride (MCT) detectors are used because their bandgap fits the IR range [23].

In a computer, Fourier-Transformation is applied to transform the signal into the emitted spectrum. This is then set into relation to a reference spectrum (background) to give the absorption of the sample [23].

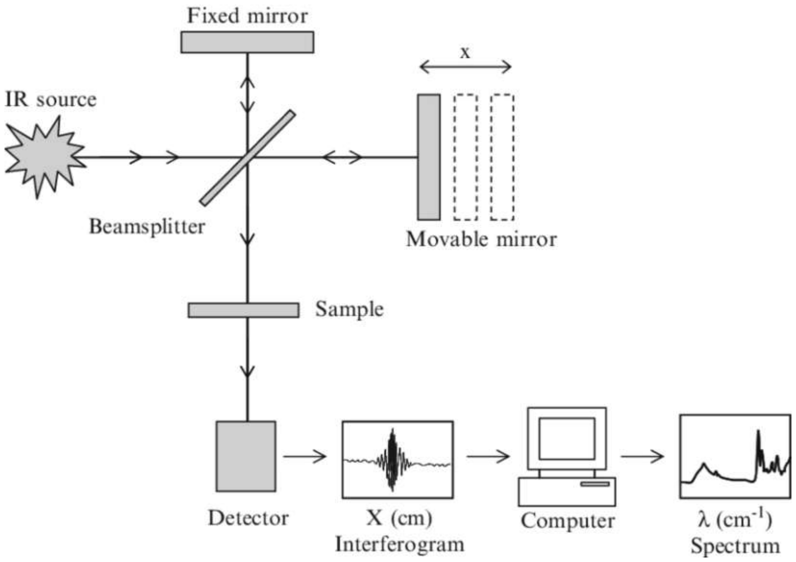

Figure 2.8: Sketch of a FTIR spectrometer and its most important parts [26].

2.2.3 Near-Infrared Spectroscopy

The basic principles of near-infrared (NIR) spectroscopy are the same as described in the IR section as it is also an absorption technique using a polychromatic light source. Though a different source is used which emits light in the NIR range. The biggest difference to mid-IR is that overtones of fundamental vibrations (i.e. transitions into higher energy states) or combination bands correspond to wavelengths in the NIR region (0.8 - 25 µm wavelength or 4000 - 12 500 cm^{-1} wavenumber). Besides the condition for the dipole moment $\frac{\partial p_{el}}{\partial Q} \neq 0$, the oscillator describing the bonding vibration needs to be mechanical anharmonic for a high intensity of the absorption bands. So the two masses of the participating atoms should be different. This pertains also in the mid-IR region, but is more important for the overtones because they have weaker intensity. Hence, mostly overtones coming from C-H, N-H, or O-H stretching vibrations are detectable. The bands are often overlapping and as they are mostly referring to only a number of bonds they cannot be used for detailed material specification. Still, identification is possible, if the NIR spectra are compared (automatically) to a database, where many spectra of different materials are stored. Also, quantitative analysis of complex molecules or a chemical intermixture is possible even though the bands are overlapping. This can be done with a multivariate chemometric analysis using a statistical model [22, 23].

It also has to be taken into account that the intensity of an overtone absorption band is a factor 10 weaker than the fundamental vibration. This can be an advantage because thicker samples can be measured and no detailed sample preparation is needed. The NIR spectra can be measured in transmission mode or in reflection mode. In reflection mode the beam enters the sample and only gets reflected by a material that is opaque in the NIR region, like e.g. a metal or a Si-wafer. It passes the sample two times and gets absorbed on the way. This can be used to investigate several layers of polymers without separating them (which would be necessary for the ATR IR technique) [22, 23].

NIR Spectrometer

A NIR spectrometer consists of the same parts as an IR spectrometer, but some principles work differently: (i) the polychromatic light source in the NIR range is often a tungsten halogen lamp. (ii) As wavelength selector monochromators are common. (iii) The sample cell is only needed for the transmission mode. (iv) To detect the wavelengths often line array detectors are used, which can be equipped with lead sulfide photo diodes which transform the electromagnetic wave into an electrical signal [23].

Although FT spectrometers can be found in the NIR range, dispersive spectrometers are more common, where the wavelengths are separated by a monochromator. It exists of two narrow slits, where the polychromatic beam is sent through at the beginning and the end. In between an optical system to guide the beam and the dispersive element are located. The dispersive element can either be a diffraction grating or a linear variable filter, which both separate the wavelengths spatially. A linear variable filter relies on the interference principle of thin dielectric layers, which eliminate all wavelengths except a small bandgap. The layers vary in thickness and therefore reflect the different wavelengths dependent on the axis of the filter [23].

2.2.4 Raman Spectroscopy

Raman spectroscopy is a scattering technique so it works differently than IR and NIR. If a molecule is irradiated with a monochromatic laser, it is excited into a high virtual energy state from where different relaxation pathways can happen. A part of the radiation is scattered elastically with the incident frequency (Rayleigh scattering) when the molecule relaxes back into the ground state. However, inelastic scattering (Raman scattering) is also possible if the molecule relaxes back to the first vibrational energy level and emits a lower frequency than the incident radiation. The frequency difference to the incident radiation corresponds to the energy gap of rotational-vibration energy states of the molecule. Hence, the molecule's vibrations can be monitored in the Raman spectrum as the so-called Stokes lines. Anti-Stokes lines are also detected (but less probable) if the molecule is in a higher vibrational energy state before interacting with the incoming radiation and relaxes to the ground state (see Fig. 2.9). As the Raman scattering is more unlikely than the elastic Rayleigh scattering, the Raman lines have less intensity and the Rayleigh line has to be filtered out to make spectral analysis possible. The x-axis of the Raman spectra is mostly given as a difference between the wavenumber of the incident and the scattered radiation, which means that 0 corresponds to the wavenumber of the laser [17, 22, 23].

If the energy of the laser is high enough to excite electrons of a molecule into a higher energy level, part of the radiation can be absorbed by the molecule. The excited electrons emit fluorescence radiation when they stepwise fall back to their ground level. This fluorescence has a much higher intensity than the Raman peaks and gives broad unspecific signals. Thus, the fluorescence overlaps with the specific Raman bands and makes their detection more difficult. Therefore, the energy of the laser should be smaller than the energy gap of the involved electrons. However, already small amounts of impurities or additives with fluorophoric groups can make fluorescence that overlaps the Raman lines. A solution would be the use of a laser with less energy, for example with wavelengths in the NIR range instead of the visible spectra. But as for the intensity of the Raman lines pertains: $I_{Raman} \approx \nu_0^4$ with the incoming frequency ν_0 a compromise has to be found between prevented fluorescence and the less scattering efficiency and therefore less intensity of the spectrum [22, 23].

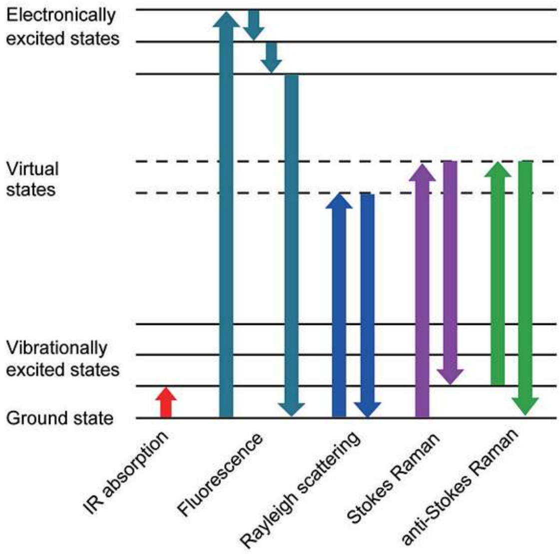

Figure 2.9: Comparison of different excitation effects: IR, Rayleigh scattering, Raman scattering (Stokes and anti-Stokes) and fluorescence. Figure modified from [27].

Raman spectra often differ significantly from IR spectra of the same molecules, although the same vibrations refer to the same wavenumbers in both spectra (see Fig. 2.10). This is due to different selection rules that Raman spectroscopy obeys. It can be explained classically with the fact that an incoming wave induces an electrical dipole moment that is proportional to the electrical field $\boldsymbol{E}$ of the wave and added to the permanent dipole moment $\boldsymbol{p}_{el}^0$ of the molecule:

$$\boldsymbol{p}_{el} = \boldsymbol{p}_{el}^0 + \tilde{\alpha} \cdot \boldsymbol{E} \tag{2.19}$$

with the polarisability tensor $\tilde{\alpha}$. The electrical dipole moment and the polarisation can be developed in a Taylor series in the directions of the normal modes of the molecular vibrations Q.

For small deflections we can use the approximation of harmonic oscillations and write the $n-th$ normal mode as $Q_n(t) = Q_{n0} \cdot cos(\omega_n t)$. If everything is inserted in (2.19), the time dependent electrical dipole becomes:

$$\boldsymbol{p}_{el} = \boldsymbol{p}_{el}^0 + \sum_n \left(\frac{\partial p_{\mathrm{el}}}{\partial Q_n}\right)_0 Q_{n0} \cos \omega_n t + \tilde{\alpha}(0) \boldsymbol{E}_0 \cos \omega t + \left(\sum_n \left(\frac{\partial \alpha_{ij}}{\partial Q_n}\right)_0 Q_{n0} \cos\left(\omega \pm \omega_n\right) t\right) \frac{\boldsymbol{E}_0}{2}. \tag{2.20}$$

Here the first term is the permanent dipole moment of the molecule, the second one is oscillating with the molecule vibration (responsible for the IR spectra), and the rest are the induced molecular dipole terms from the incoming wave. The oscillating dipole is radiating light in three different frequencies, the Rayleigh frequency (the third part in (2.20)), the Stokes $(\omega - \omega_n)$ and the anti-Stokes $(\omega + \omega_n)$ frequencies. It shows that the amplitude of these outgoing waves depends on the polarisation in the directions of the normal modes, which means that they are 0 if $\left(\frac{\partial \alpha_{ij}}{\partial Q_n}\right) = 0$. Hence, in the Raman spectra, only such vibrations are visible in which the polarisation is modulated. Contrary to the IR spectrum, symmetric vibrations can be detected with high intensity in the Raman spectrum, but asymmetric ones often not, if the polarisation does not change. This emphasises that both techniques are complementary and can be used together to identify a molecular structure in detail [17, 22].

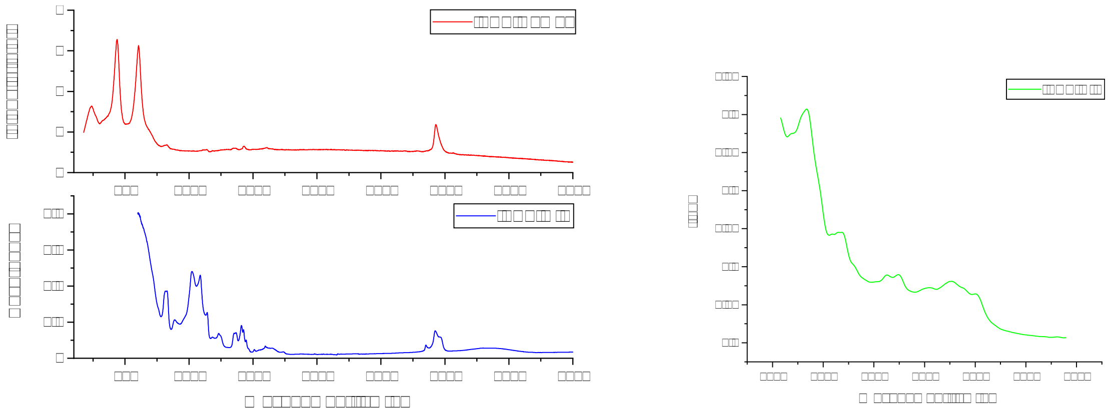

(a) Mid-infrared (MIR) spectrum in Absorbance and Raman spectrum.

(b) NIR spectrum

Figure 2.10: Comparison of the spectrum of different spectroscopic methods of a TPT (Tedlar©) backsheet.[1] All spectra show different bands of the same material.

Raman Spectrometer

A Raman spectrometer consists of the following parts: (i) a monochromatic laser; (ii) an optical system to guide the beam to the sample and focus it there; (iii) the sample cell; (iv) a dispersive spectral separator often with a diffraction grating; (v) a multichannel detector, mostly charge-coupled devices (CCD) and (vi) a computer to transform the electrical signal in a spectrum (see Fig. 2.11) [23].

In the Raman spectrometer the laser used for the excitation of the sample can have its wavelength either in the visible (400 - 800 nm) or in the near-infrared range (e.g. 1064 nm). The

---

[1] This graph and all graphs in the following were done in Origin [28] by myself.

optimum wavelength for excitation depends on the sample type and the problem of interest. For lasers in the NIR range also Fourier-transformation-Raman spectrometers exist, which work similar like the FTIR spectrometers. For lasers in the visible range dispersive multichannel Raman spectrometers are used. Here a diffraction grating splits the laser beam according to its wavelength. This makes an image on a focal plane, where a multichannel detector is suited. For that nowadays charge-coupled devices (CCD) are in use, which are based on a photosensitive semiconductor (mostly silicon). Each wavelength hits a dedicated pixel and is transformed into an electrical signal which gives the Raman spectrum [23, 29].

A large advantage of Raman spectroscopy compared to IR is that the laser signal can be transported through quartz light fibres to the sample and back which could be longer than 100 m. Moreover, direct contact of the probe with the sample material is not necessary as the spectrum is recorded in the focal point of the laser allowing measurements behind a transparent glass or film [29].

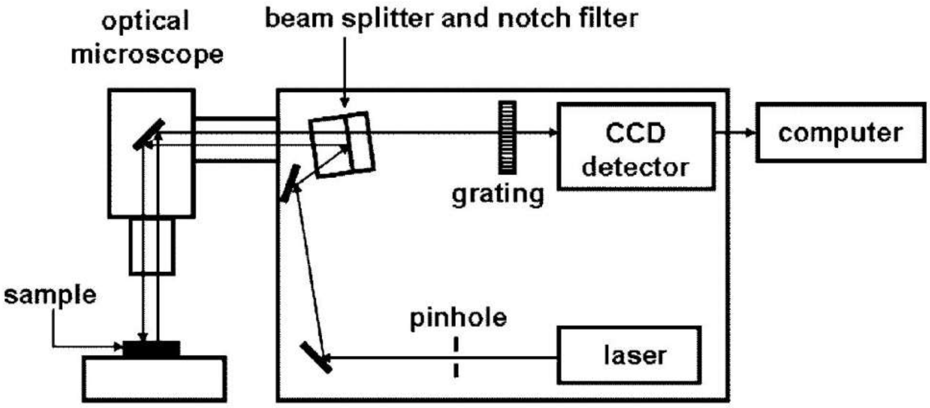

Figure 2.11: Sketch of a dispersive Raman spectrometer and its most important parts [30].

Chapter 3

PV Test Site

The PV test site under investigation is located on the foot of Bisamberg on the northern border of Vienna. Twelve PV modules are mounted on the roof of a small house, tilted by 6 degrees from the horizontal and orientated about 36 degrees away from the south to the west.

Originally, these modules had been part of a PV park in Ahlburg, Germany, where they were installed from 2012 to June 2021. Because the backsheets of the modules showed cracks, they were dismounted and replaced. 24 modules were chosen for repair tests within the research project PVRe^2, as described in Chapter 1. For the outdoor monitoring in the field, twelve modules without any *hotspots* [2] were selected for the repair process. The test site modules have the number 69Tx with x from 1-12 which will be called Module 1-12 from now on.

The modules were coated in the beginning of July 2021 and mounted on the roof shortly afterwards. Figure 3.1 shows a picture of the test site mounted on the roof. Furthermore, Figure 3.2 outlines the module assignment, their respective coating as well as the place of the pyranometer (P) and the temperature sensors (which will be described in Section 4.1).

Figure 3.1: PV test site with the twelve coated modules mounted on the roof.

---

[2] A hotspot occurs if the short circuit current of one single cell is lower than the operating current of the module. Then the power generated in the other cells is transformed into heat by the affected cell [31].

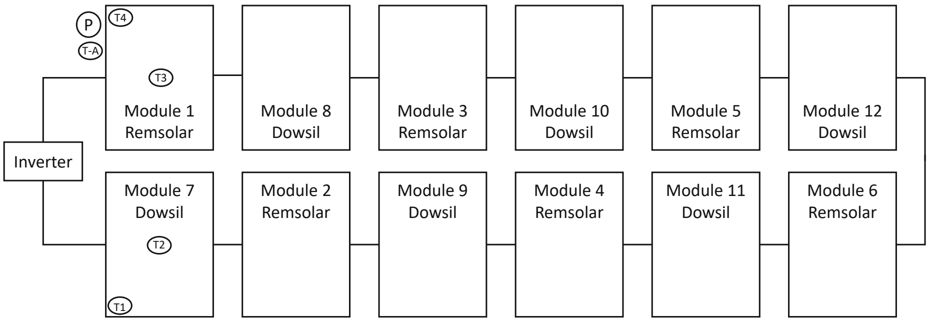

Figure 3.2: Arrangement of the modules on the test site with the two coatings (Remsolar and Dowsil) on the backsheet and the placement of the inverter, the pyranometer (P) and the five temperature sensors (T1-4 module temperature and T-A ambient temperature).

3.1 Modules

The modules are of the type Schott Power^{TM} Poly 240 [32]. Each module consists of 60 polycrystalline solar cells (15.6 cm × 15.6 cm) with three busbars each and a junction box IP65 with three bypass diodes. The modules initially had an efficiency of $\eta = 14.7\%$. The produced power at the maximum power point (P_{MPP}) has a temperature coefficient of $-0.45\,\%/\mathrm{K}$. An ethylene-vinyl acetate copolymer (EVA) encapsulant protects the solar cells on both sides. Solar glass on the front side and a polyamide polymer backsheet on the backside provide further protection and stability. The frame is made of aluminium with a total dimension of 165.2 cm × 99 cm × 3.5 cm [32]. Table 3.1 lists the module's electrical characteristics.

Table 3.1: Electrical characteristics (power P_{MPP}, voltage U_{MPP} and current I_{MPP} at the maximum power point; open-circuit voltage U_{OC} and short-circuit current I_{SC}) of the modules according to the type label.

P_{MPP}	$\geq 240\,\mathrm{W}$
U_{MPP}	$29.8\,\mathrm{V}$
U_{OC}	$37.2\,\mathrm{V}$
I_{MPP}	$8.1\,\mathrm{A}$
I_{SC}	$8.59\,\mathrm{A}$

3.1.1 Polyamide Backsheet

The main focus of this project lies on the polymer backsheet of these modules because of the detected failure (cracks) and the repair methods developed for this purpose. The backsheet used was a polyamide backsheet Icosolar AAA 3554 made by Isovoltaic with a thickness of $(0.35 \pm 0.05)\,\mathrm{mm}$ [33]. The co-extruded backsheet is built of three layers which all consist of polyamide-12 (PA12). Figure 3.3b shows the chemical structure of PA12. The core layer is modified with polypropylene (PP) and contains a silica filler (glass fiber) for better mechanical properties. Furthermore, the outer and inner layers contain a TiO_2 filler, which is added to achieve protection against UV light [34]. Figure 3.3a shows a microscopic picture of a cross-section of the backsheet as part of a PV module. Also the EVA encapsulant of the module is visible on the upper part.

Although PA12 is more robust against temperature and humidity changes than other polyamide

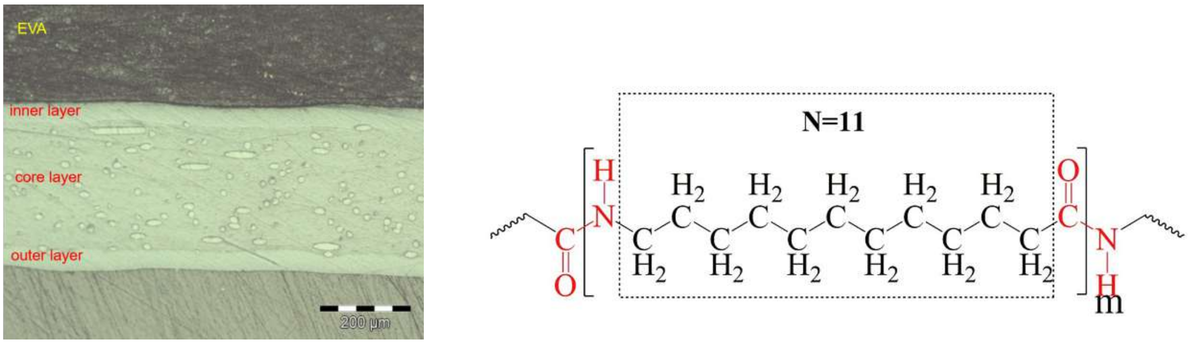

(a) Light microscope image of cross-section of the three layers of a PA backsheet as part of a PV-module [10].

(b) Chemical structure of polyamide 12 [35].

Figure 3.3: Polyamide backsheet information.

structures, ageing-induced changes can be detected, if the PA backsheet is exposed to strong environmental stresses in the field for several years or artificial weathering tests [10]. Besides the visible cracks in the backsheet which will be discussed in detail in Section 5.2.1, especially photo-oxidative degradation and chalking on the surface were detected. The exposure of the surface of the PA12 backsheet to high doses of irradiance in the presence of oxygen can trigger breakage of the polyamide chains, which is called photo-oxidation degradation. This surface effect can be detected by infrared spectroscopy, as photo-oxidation causes a carbonylband (C=O) at 1710 cm^{-1} to increase in intensity with increasing ageing [10].

The chalking is related to the TiO_2 particles. Although, they should protect the backsheet against UV light they can also form radicals under the impact of UV irradiation which can accelerate the polyamide degradation. Often chalking is a pre-sign for worse degradation effects like cracking [34].

Furthermore, cyclic amid oligomers may form crystalline deposits on the surface of the PA backsheets in accelerated ageing tests under damp heat conditions. During the building process of polyamide these cyclic oligomers develop. These structures are not fixed in the long PA polymer chains but can move freely in the material. Therefore, under extreme temperature and humidity conditions, they migrate to the surface, where they can be detected with the microscope [36, 37, 38].

3.2 Coating of the Modules

The method for repairing modules with cracked backsheets was developed within the project PVRe^2 [12, 15], where it was learned that the optimal repair process was to dismount the modules and apply the repair solutions on the backside of the flat-lying modules. For this project's test site, the modules were transported from Ahlburg to Vienna where they were coated in the laboratory. The first step of the repair procedure is to clean the backsheet mechanically with a slightly humid towel [12]. Here it is important that the towel is not too wet, because, otherwise water could enter through the cracks into the module. After letting the backsheet dry for a minimum of 24 hours, the coating can be started.

Regarding the coating, the proper layer thickness is decisive. On the one hand, the goal is to use a minimum amount of material to reduce the cost of the repair solution. On the other hand, it is mandatory to completely fill the cracks and provide a protective layer of minimum 50 µm on the whole backsheet. This protects the backsheet against further degradation of the polyamide and stops the oligomers from migrating to the surface. In the developing phase of the different coatings, a detailed microscopic analysis of cross-sections was done to see whether the cracks were completely filled with the coating. To do this, parts of the coated modules with deep cracks were cut out, embedded in an epoxy resin, polished and the cross-section was then analysed with a light microscope (see Figure 3.4) [12, 15]. Doing so, the coating thickness could also be measured and checked if it is sufficient.

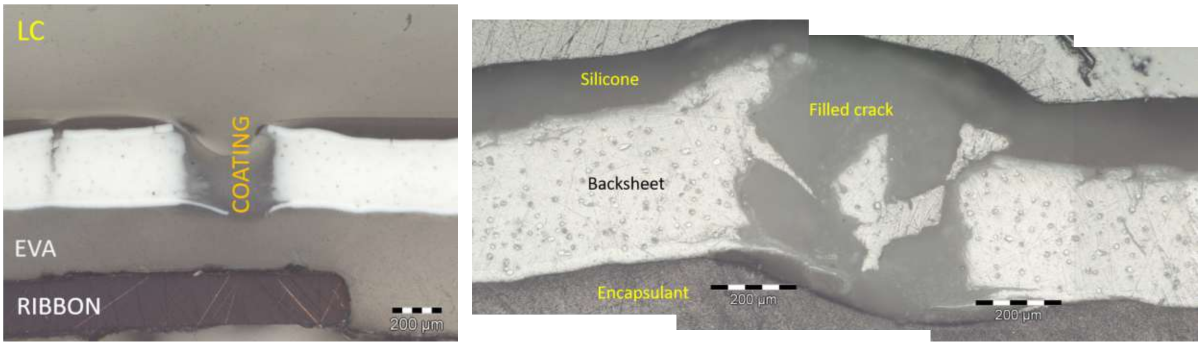

(a) Remsolar coating [16].

(b) Silicone coating [15].

Figure 3.4: Light microscope images of cross-sections of coated modules with deep cracks.

The example cross-section in Figure 3.4a shows that the crack is filled but the cover layer is not sufficient. The layer had a thickness of 16-61 µm [12] which is too thin on some parts, as for instance on the edge of the cracks, as degradation of the backsheet could take place again. To achieve a satisfactory thickness on the whole backsheet the needed amount of coating material for each module can be calculated. For that it is assumed that the cracks are rather small on the backsheet (which was the case for the considered modules) and not a big percentage of the coating goes into the cracks but forms an even layer. With a module backsheet area of $A = 1.59\,\mathrm{m}^2$ and a desirable average coating thickness of 75 µm, the coating volume is $122.5\,\mathrm{cm}^3$. Given the different material densities of the different coating solutions, the needed material can be calculated in grams, so it can easily be weighed before the coating. The coating processes with two different types of repair materials will be described separately in the following.

3.2.1 Remsolar Polyurethane Coating

For Modules 1-6 a polyurethane based coating PU 2K Remsolar developed by Rembrandtin Coatings GmbH was used. It was applied in two layers: first, a transparent crack filler and, secondly, a white (because it contains a filler) cover coating. Both of them are composed of a two-component system, a resin and a hardener (442). All materials are based on polyurethane but contain different amounts of solvent that evaporates a short time after the coating. In the first step of the coating process, the crack filler was mixed with the hardener and applied with a paintbrush on top of the cracks. All deep cracks have to be entirely closed so the cover coating can form an even layer. The cover coating was applied with a squeegee after letting the crack filler dry for around 15 minutes (see Fig. 3.5a).

To calculate the average coating layer several things have to be taken into account. First, the relative density of the two-component solutions has to be calculated, with the percentage mixing ratio. Furthermore, the solvent share must be considered, which reduces the amount of material on the backsheet when it evaporates. It is assumed that already the crack filler forms an even cover layer because not a big percentage goes into the cracks. Then both layers' thicknesses d can be calculated by:

$$d = \frac{V}{A} = \frac{m}{\rho A}. \tag{3.1}$$

Table 3.2 gives the values to calculate each layer thickness when initially 150 g for each layer were used. In total, the average coating layer is $d_{tot} = d_{fill} + d_{cover} = 58.0 + 50.1 = 108.1\,\mu\text{m}$. However, it must be mentioned that the layer thickness is only an average value because although, the squeegee was found to be the best tool for evenly coating it is still quite difficult to form a steady layer.

Table 3.2: Material characteristics of Remsolar coating, information taken from [39, 40, 41].

	crack filler	hardener	cover coating	hardener
material density	$1.1\,\text{g/cm}^3$	$1.16\,\text{g/cm}^3$	$1.45\,\text{g/cm}^3$	$1.16\,\text{g/cm}^3$
mixing ratio	100 : 14.1		100 : 7.7	
percentage of material	87,6%	12.4%	92.9%	7.1%
relative density	$1.11\,\text{g/cm}^3$		$1.43\,\text{g/cm}^3$	
material used	150 g		150 g	
solvent share	36.2% (47.59 g)	-	25.8% (35.93 g)	-
remaining material m	102.41 g		114.07 g	
layer thickness d	58.0 µm		50.1 µm	

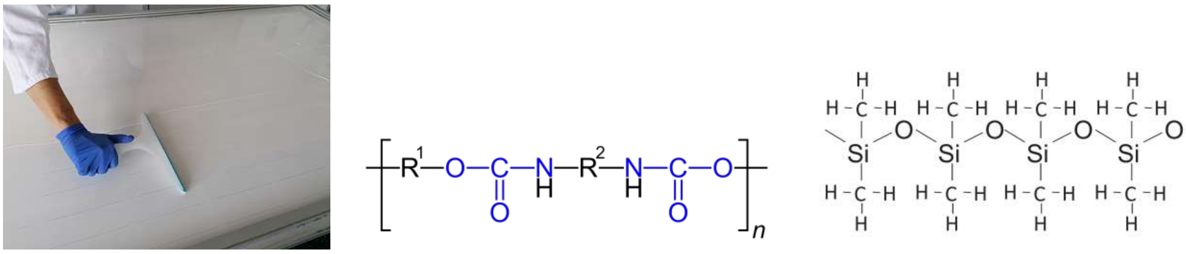

(a) Picture of distributing the Remsolar cover coating.

(b) Chemical structure of Polyurethane [42].

(c) Chemical structure of PDMS [15].

Figure 3.5: Coating procedure (a) and chemical structures of coating materials (b,c).

3.2.2 Dowsil Silicone Coating

Modules 7-12 were coated with Dowsil^{TM} 7094 flowable sealant developed by the Dow Chemical Company [43]. In contrast to the Remsolar product, it was applied only in one layer. It contains no evaporating solvent, and also only a single component that cures when exposed to ambient moisture. It consists of a polydimethylsiloxane (PDMS) polymer mixed with a filler (calcium carbonate particles). Figure 3.5c shows the chemical structure of PDMS with the Si-O-Si-O... backbone and the CH_3 groups bonded to the silicon. Because of the special type of PDMS, it is a flowable silicone that can be poured onto the backsheet of the flat module and spread evenly with a squeegee [15].

For each module 160 g of the Dowsil coating was used. With the density of the coating of $\rho = 1.3\,\text{g/cm}^3$ [43] the thickness of the coating can be calculated again using Equation 3.1 to:

$$d_{sil} = \frac{160\,\text{g}}{1.3\,\text{g/cm}^3 \cdot 15\,919\,\text{cm}^2} = 77.3\,\mu\text{m}. \tag{3.2}$$

3.3 Inverter

Figure 3.2 displays that all the modules are connected serially as a string to one inverter, a Fronius Symo 3.0-3-M [44]. The three-phase inverter is located inside the building beneath the PV modules. It has a DC input voltage range from 150 - 1000 V, a maximum input current of 16 A and a maximum PV generator power of 6 kWp. The efficiency depends on the operation point and can vary between 79.8% and 98%. The Fronius Symo also provides a Modbus TCP SunSpec interface, which will be used later in the project for the continuous data monitoring of the modules' produced power and energy [44].

Chapter 4

Monitoring Setup

The purpose of the work is to gather information about the test site's electrical performance as well as to analyse the long-term stability of the developed repair solutions for the backsheets of the PV modules. On the one hand, a monitoring system was developed to analyse how the coating was affecting the electrical performance of the modules. We measured

- the electrical characteristics of the modules
- the temperature
- the incident irradiance

at the site to allow for calculating the nominal power. This was complemented with measurements of the insulation resistance and the I-V curve of the modules.

On the other hand, the material stability of the coatings on the modules was monitored. For this purpose we did

- adhesion testing
- Raman spectroscopy
- infrared (IR) spectroscopy
- near infrared (NIR) spectroscopy
- microscopic measurements

All measurements were done on one representative module for each coating, i.e. Module 1 for the Remsolar and Module 7 for the Dowsil coating. Figure 3.2 shows that both are on the border of the test site and therefore best accessible from the edge of the roof.

4.1 Electrical Setup

The goal is to continuously gather information on the performance of the test site and the meteorological conditions at the place. Therefore, we installed temperature sensors and a pyranometer and connected them to a Raspberry Pi 4. The data was gathered using the programming tool Node-RED and stored in a local InfluxDB database. In Grafana, the data was visualised and could be downloaded in a customised way for further analysis. The electrical data of the modules themselves was directly gathered from the inverter via a Modbus TCP protocol and also sent to the database with Node-RED. Furthermore, the data was sent to a publicly open database with a Message Queuing Telemetry Transport (MQTT) broker system, to grant other project partners access. Since February 2022 the data is and will be continuously collected.

4.1.1 Raspberry Pi

We decided to gather the data with a Raspberry Pi 4 Model B (RPI). It is a single-board computer with 4 GB RAM. With a screen, a mouse, and a keyboard connected, it can be operated like a normal computer. It also has a general-purpose input/output (GPIO) header

containing 40 metal pins for different purposes. These can be used to connect external sensors to the RPI. Any pin can be used as an input or output pin. Figure 4.1 shows the different functions of the pins [45].
For the setup of the RPI, the operating system Raspberry Pi OS (which is based on Debian Linux) was installed on an SD card using Raspberry Pi Imager. After inserting the SD card into the RPI, the system could be set up. Then the needed programmes Node-RED, InfluxDB, Grafana, and the MQTT broker were installed and set up.

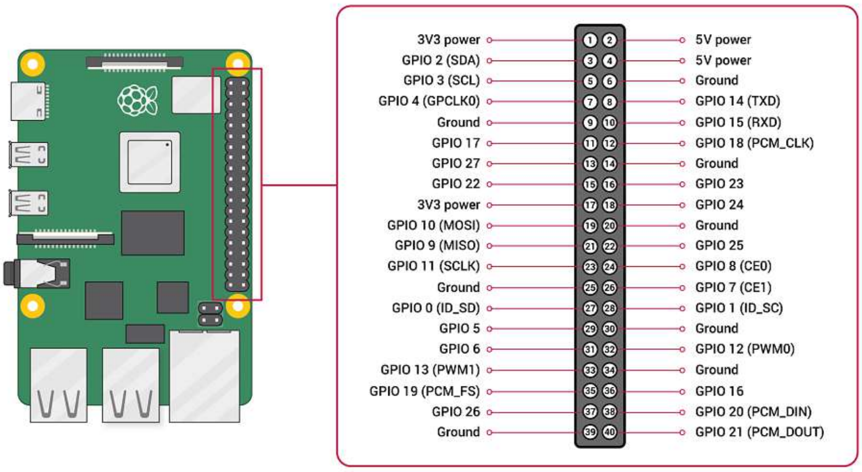

Figure 4.1: Raspberry Pi 4: GPIO header pin assignment [46].

Node-RED

For programming the data gathering by the RPI we used the tool Node-RED [47]. It works on flow-based programming, with JavaScript as a programming language. The single nodes work like so-called "black-boxes" which change given data in a specific way and send it to the next node via a message. Some important nodes are already pre-installed. A wide set of additional nodes are available for installation [47].

I installed Node-RED on the RPI and configured it to automatically restart on boot. This is important so the measurement will continue automatically, even if the RPI is rebooted by hand or after a blackout. Via the browser of the Raspberry Pi, Node-RED can then be accessed on the address: `http://localhost:1880`. Here all the programming was done. The gathered data, which will be described in the following sections is processed and then sent to InfluxDB. Furthermore, the data is published on an open server (`opendata.technikum-wien.at`) using an MQTT broker.

InfluxDB

InfluxDB is a time-series database that is suitable for time-stamped data originating from various sensors. Because the Raspberry Pi has only a 32-bit system, the InfluxDB version 1.8 had to be used. After the installation it was also configured to automatically restart on boot. Then the Database *testanlage* was created. The data is stored directly on the RPI in the folder */var/lib/influxdb/data*. This was done in Node-RED using the node `InfluxDB out`, where each measurement gets an identifying name. When setting up the node for the first time the server had to be initialised. There the InfluxDB version, the host and port `http://localhost:8086` and the desired database (*testanlage* in this case) had to be selected.

To avoid unnecessarily huge log files, the *influxd.conf* file needed to be adapted to handle the numerous measurements taken at ever 10 seconds. In the default setting, every entry in the database is logged with a line in the syslog file of the RPI. Therefore, the syslog file can get very big. To avoid such a situation, $suppress\text{-}write\text{-}log = true$ was set inside the *influxd.conf* file under the *http* section. The writing is no longer logged, only error messages are. The syslog file stays therefore much smaller.

Grafana

Grafana is an open-source application to query and subsequently visualise data of different data sources. Raw data can be accessed easily, analysed with simple statistics, and then visualised in many different ways. In the project, it makes the data stored in InfluxDB accessible and understandable [48]. After Grafana was installed on the RPI and autostart enabled it could be accessed on the address: `http://localhost:3000`. Then, an account was created and a dashboard set up where all the data is presented. To connect to the InfluxDB database it needed to be added as a data source. After InfluxDB was selected as database type, the URL was set to `http://localhost:8086` and the database name *testanlage* was entered as well as user information of the RPI. With these pre-settings done, queries could be added to the dashboard with all different measurements gathered by InfluxDB. Besides the graphic presentation, data can also be downloaded as a csv-file for further analysis, which will be described in Section 5.1.

Message Queing Telemetry Transport (MQTT)

To make the data gathered on the RPI also available for all project partners, it is sent to a publicly accessible MQTT broker system (`opendata.technikum-wien.at`). Mosquitto was installed and enabled on the RPI, so the RPI can publish data on the broker. I programmed the publishing in Node-RED with a `mqtt out` node. In the beginning, the appropriate server was selected, the port set to `8883`, and a new topic was initialised to *PVRe2Bisamberg*. Every measurement was then assigned a subtopic which was added with a slash behind the topic. So each measurements got its own `mqtt out` node next to the `InfluxDB out` node (see Figures 4.3-4.8). Every client who is subscribed to the correct topic receives the data from the broker in real-time.

4.1.2 Temperature Sensors

The temperature of the modules had to be monitored, because the power of PV modules is temperature dependent and the modules heat up during operation, especially at high irradiance. As a direct measurement at the operating cells is not possible, the most accurate temperature can be obtained via a sensor on the backside of the modules. The module temperature is of special interest in this project, because it gives us also the temperature of the coating. Therefore, five temperature sensors were mounted at the test site. One monitors the ambient air temperature and the others measure the backsheet temperature of two modules with different coating (Module 1 and Module 7). On each module two sensors were mounted, one in the middle and one on the corner of the backsheet.

DS18B20 digital thermometers are used because they communicate over a 1-wire bus which is suitable for the Raspberry Pi. They have an accuracy of ±0.5°C in a temperature range between -10°C and 85°C. Because the sensors per se are not waterproof but they are expected to be in operation outside for several years, they had to be made waterproof (encapsulated). The detailed preparation and mounting of the sensors as well as the connection to the RPI is described in follow up work [49].

Figure 4.2 shows the sensors mounted on Module 1 and Module 7 for the module temperature and Sensor 5 for the ambient temperature. As adhesive tape is not sticking on silicone wooden sticks press the sensors against the coated backsheet of Module 7.

(a) Sensor 4 mounted on the corner of Module 1 (Remsolar).

(b) Sensor 1 mounted on the corner of Module 7 (Dowsil).

(c) Sensor 5 measuring the ambient temperature.

Figure 4.2: Three of the five temperature sensors mounted on the testsite.

Node-RED Programme

To continuously measure the temperature of each sensor a programme in Node-RED was written. Figure 4.3 shows an overview of the used nodes. First, the specific sensor ID, which every sensor has from the manufacturer, was assigned in a `sensor-ds18b20` node. In this node the periodicity of the data gathering was set to 10 seconds. Next a `switch` node working like an *if* loop filters the gathered values. It processes only values smaller than 85 and deletes the value 85 (because this is the default response value) and undefined expressions. Then a `join` node combines the data of all five sensors so they can be written in a common measurement in the database. To save data storage space, a `filter` node only forwards the values if they change. Besides the InfluxDB and the open MQTT broker, the temperature values are sent to the debug sidebar (with the `debug` node), where a direct check on the values is possible. In the `influxdb out` node the server was set to the settings described in Section 4.1.1 and a new measurement *temperatur* was created. The same was done for the `mqtt out` node, where the topic was set to *PVRe2Bisamberg/temp*.

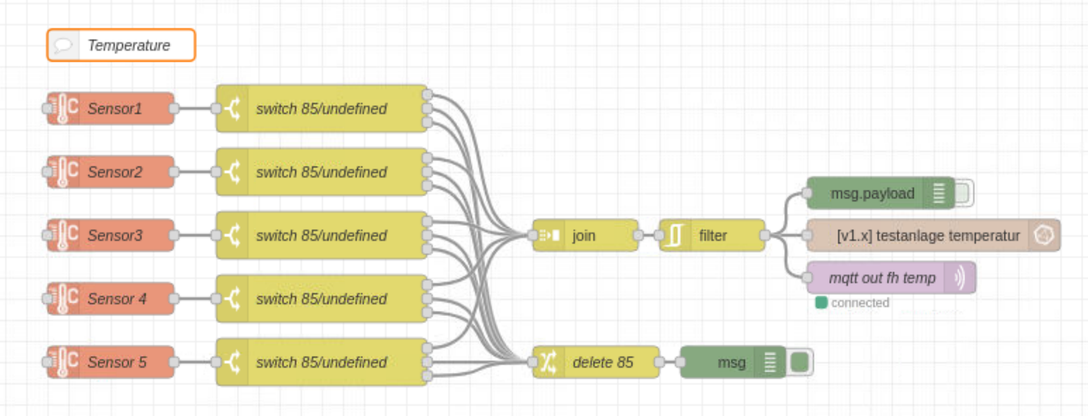

Figure 4.3: Node-RED flow for the temperature measurement.

4.1.3 Plane-of-array Irradiance Measurement

A pyranometer LP PYRA 03 [50] measures the irradiance (direct and diffuse) using a thermopile sensor at the test site. Figure 4.4 shows that the pyranometer is mounted directly next to Module 1 in the plane-of-array. The sensor consists of a matt black thermopile sensitive surface and a glass dome around it. Absorbed radiant energy is heating up the center of the thermopile, creating a temperature difference to the body of the pyranometer. This results in a potential difference (Seebeck effect) that can be measured. The sensitivity of the sensor is defined by the manufacturer to be $S_{pyra} = 15.54\,\mu\mathrm{V\,W^{-1}\,m^2}$. Hence, the measured voltages (U) can be transformed into the incident irradiance (E_e)

$$E_e = \frac{U}{S}. \tag{4.1}$$

The pyranometer has a measuring range of 0 - 2000 $\mathrm{W/m^2}$ and a spectral range between 300 and 2800 nm. According to ISO 9060:2018 it is inside the spectral flat class C [50].

Figure 4.4: LP PYRA 03 pyranometer mounted next to Module 1, parallel to the module plane (plane-of-array irradiance), with the test site in the background.

A precise calibration was done with the pyranometer before it was set up [49], which resulted in an uncertainty of the sensitivity of $\sigma_{E_e} = 3.11\%$.

The LP PYRA 03 has a 4-pole connector from where the cable leads to the Raspberry Pi. Because it is a passive element, it does not need a power supply [50]. However, the RPI only has digital input pins so it cannot read the generated voltage of the pyranometer directly. Therefore, an analogue-digital converter (ADC) has to convert the signal. Here a Texas Instruments ADS1115 [51] was used. It has a resolution of 16 Bits and a programmable gain amplifier (PGA), so low (as needed for the pyranometer) voltages can be converted. The ADC was connected to the RPI and a python script was written to read the irradiance from the pyranometer using the ADS1115 (see detailed description in [49]).

Then the continuous data gathering was done in Node-RED (see Figure 4.5). In the flow an `inject` node is triggering an `exec` node every ten seconds, which executes the command `python3 adc1115_pyranometer.py`. With the command, the Python programme, which calculates the irradiance from the measured voltage, is executed. Then a `function` node is changing the string into a number so it can be sent to the output nodes. Here the measurement of the InfluxDB was set to *Einstrahlung* and the MQTT subtopic to */irradiance*.

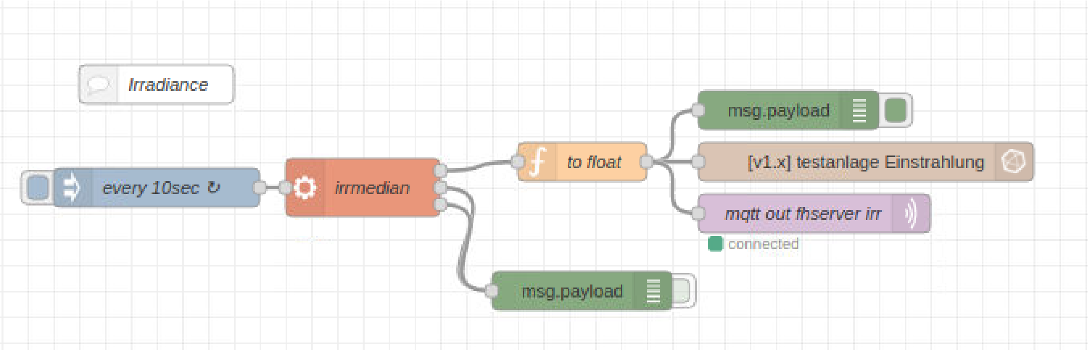

Figure 4.5: Node-RED flow for the irradiance measurement.

4.1.4 Modbus TCP

The electrical characteristics of the PV modules installed in the test site are the main data gathered and analysed. The Fronius Symo inverter used at the test site supports the Modbus TCP protocol with Sunspec profile [52, 53]. Therefore, many different characterisation data can be received and saved. All data is measured by an internal measuring device of the inverter with an accuracy of 3% [54]. The Modbus protocol is working with a master-slave communication. Here the inverter is the slave and the RPI the master. The data transfer works via an IP address because both systems are registered in the same WI-FI network [52]. The data of interest can be requested by a specific register address, which is defined by the SunSpec Alliance and available in the Modbus register - SunSpec Maps, which can be downloaded on the Fronius Homepage [55]. In this project only the *Inverter_register_map_float* is used. Various electrical data of the test site is available in different data types: unsigned integer in 16, 32, and 64 bit format as well as floating point 32 bit.

We decided to gather the following data of the test site:

- generated power of the modules [W] in DC (before conversion);
- generated power of the modules [W] in AC (after the inverter);
- produced energy per day [Wh];
- total AC current [A] after inverting (only the current and no total voltage is available);
- DC voltage [V] at maximum power point (MPP);
- DC current [A] at MPP.

In the following, the programmed flows are described in detail.

Node-Red Flows

To read the Modbus TCP data, the `node-red-contrib-modbus` package was installed. For each data of interest, a `Modbus-Read` node reads the data from the specified address. Because the register address is saved in an array and the first entry is the [0] element of the array, all address values entered in Node-Red are the address value stated in the *Inverter_register_map_float* (and in this section) minus 1. Furthermore, the function code was set to Read Holding Registers and the poll rate to 10 seconds. To get the data from the inverter, the Fronius Symo was selected as a server and initialized with its IP Address and the right port.

First, the total power of the test site (Address 500) is read. The values are directly given in Watts so no transformation or scaling is necessary. Because the `Modbus-Read` node sends an array with the data stored in the elements, a `function` node reads the zeroth entry. This is then only forwarded by a `filter` node if it changes. Then the value is sent to the InfluxDB measurement *leistung* and the MQTT subtopic */powertot*.

Figure 4.6 shows that the setup to record the produced energy per day (Address 502) is similar. It is also given directly in [W/h]. However, here the poll rate is set to once per hour because this value is only slowly increasing during the day and is not needed for precise calculations later on. The rest of the flow is the same as above but with the InfluxDB measurement *Energietag* and the MQTT subtopic */energyday*.

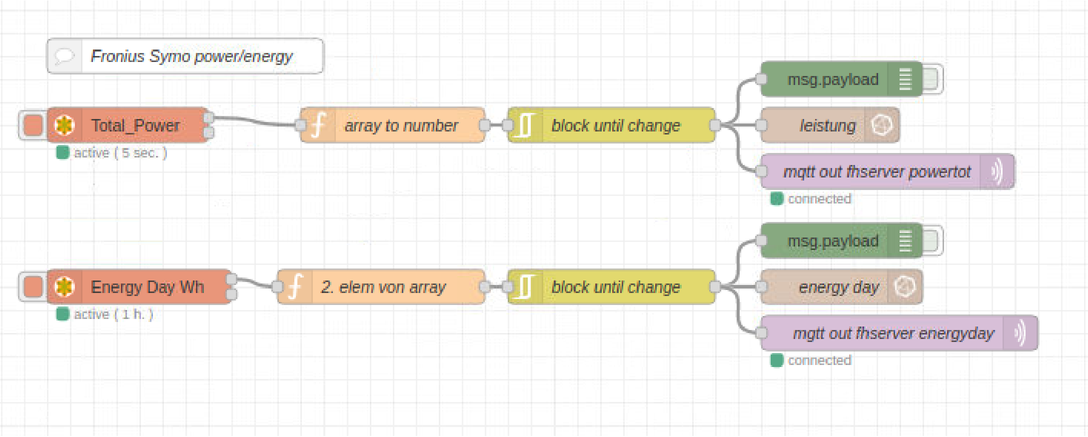

Figure 4.6: Node-RED flow for the total power and energy production of the test site.

The DC power of the test site (Address 40108) is of interest because it gives more precise information of the exact power of the modules without the inverter losses. However, according to the register map, it is not available in unsigned integer but in floating point 32 bit. Because a Modbus holding register stores all values in 16 bit, a 32 bit value is stored in two registers. Therefore, after setting the address, the quantity needs to be set to 2. Furthermore, the `Modbus read` node sends the values in a data array but also in a buffer (as raw values in hexadecimal notation). To read other data types than unsigned integers, the raw values need to be read, which is done with the second output of the node. Here the Modbus response value (buffer) is sent first. To read the floating point value, in the `function` node the buffer is changed to a decimal number as in the following:

```
const buf = Buffer.from(msg.payload.buffer);
const value = buf.readFloatBE();
msg.payload = value;
return msg;
```

Now this number can be processed like above with a `filter` node and sent to the InfluxDB measurement and MQTT subtopic which are both called *DCpower* (Fig. 4.7). The data type of the AC total current value (Address 40072) also is a floating point 32 so it is processed exactly the same way and sent to *ACtotCurrent* (InfluxDB) and */ACtotcurrent* (MQTT).

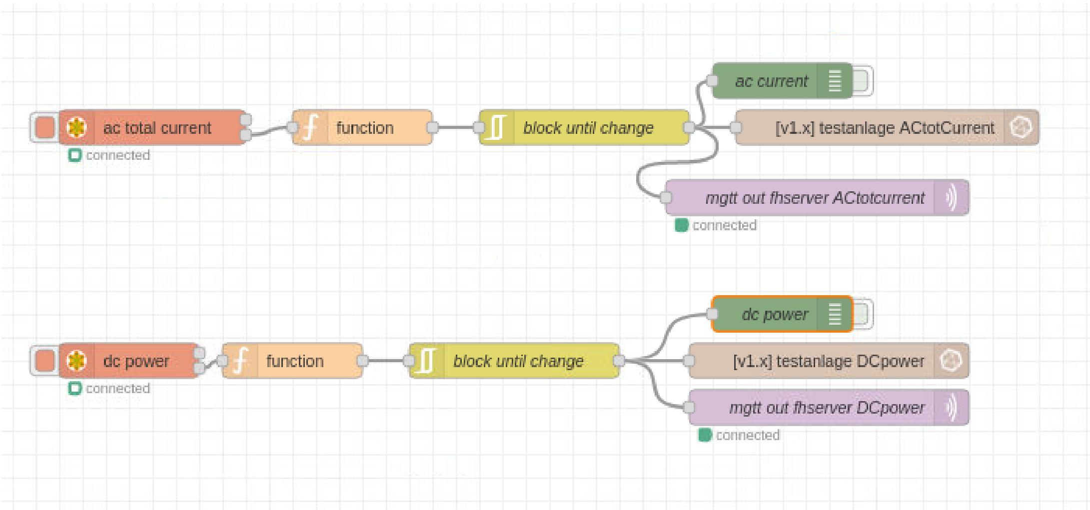

Figure 4.7: Node-RED flow for the DC produced power by the test site, and the AC total current value.

The remaining values of interest are voltage and current at the MPP. The unsigned integer values can not be directly used. They need to be multiplied with a scale factor, which is also readable from a specific address. First, the DC voltage (Address 40284) is read, where the `function` node only needs to select the zeroth entry of the data array. Then another `Modbus read` node reads the voltage scale factor (Address 40267). This is given in the data type sunssf which is a 16 bit two's complement integer [53]. Therefore, in the `function` node the buffer is read and then the scale factor (which is the exponent of 10) changed to a multiplier (sf):

```
const buf = Buffer.from(msg.payload.buffer);
const value = buf.readInt16BE();
sf = Math.pow(10, value);
msg.payload = sf;
return msg;
```

Both values are then joined in an array, so they can be used for common calculations in another `function` node, where they are addressed and multiplied. The correct voltage value is now again blocked until it changes and sent to the *S1_DCV* measurement and the MQTT subtopic */DCvoltage*.

Exactly the same procedure is applied for the DC current value at the MPP (Address 40283), where the current scale factor (Address 40266) is applied. The assigned measurement in InfluxDB is called *DC-current-s1* and the subtopic in MQTT */DCcurrent* (see Fig. 4.8).

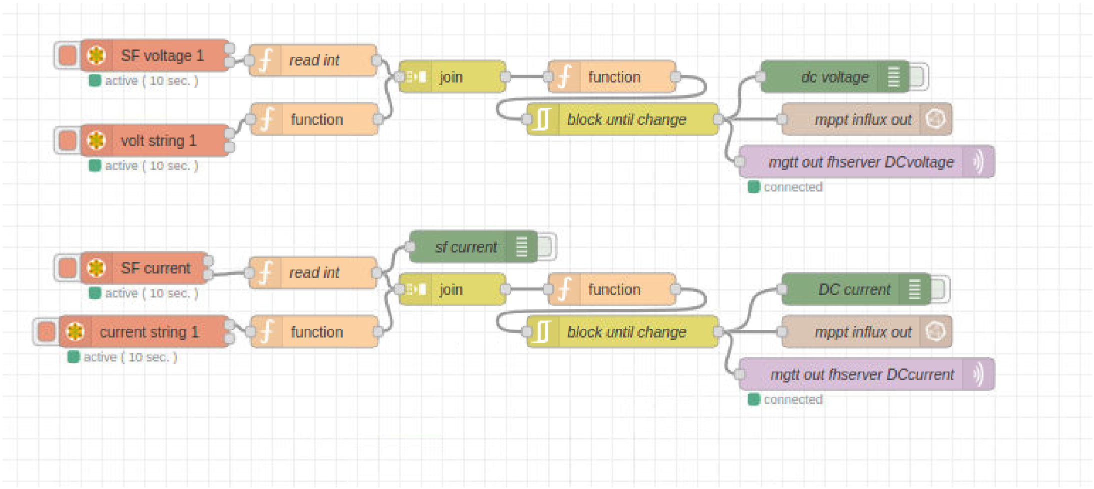

Figure 4.8: Node-RED flow for reading the voltage and current at the maximum power point (MPP).

4.1.5 Electrical Characterisation

The backsheet of the module has several functions, as giving mechanical stability and protection against environmental impact and it should be an electrical isolation between the active PV elements (silicon cells, connecting wires) and the environment. On the one hand, it keeps the active elements mechanically protected and moisture-safe, so they are not corroding. On the other hand, it protects the outside (people, animals) against an electric shock by the voltage produced in the solar cells. One of the biggest problems of the PV modules with cracked backsheets is the failure in the wet leakage test (IEC 61215-2 norm module quality test (MQT) 15 [14]). For the test, the modules are brought in wet environment. Then the positive terminal of a DC voltage source is connected to the shorted output terminals of the module and the negative one with the water. After the DC voltage supply applies 500 V for two minutes, the insulation resistance is measured. To pass the test, the measured insulation resistance R_{ISO} must be bigger than $40\,\mathrm{M\Omega\,m^2}$ [14]. For the test site modules ($A = 1.635\,\mathrm{m^2}$) this results in a insulation resistance bigger than $24.5\,\mathrm{M\Omega}$ per module. If the modules are mounted, the test can also be done with only wet backsheets.

Another parameter of interest is the I-V curve of the coated modules. If the test site is in operation, the inverter is automatically tracking the MPP, so the modules generate the maximum power. Therefore, it is only possible to request data via Modbus TCP at the MPP, such as the power (P_{MPP}), voltage (U_{MPP}), and current (I_{MPP}). As a consequence, the I-V curve can only be measured when the modules are disconnected from the inverter. The instrument used, PV-Engineering PVPM 1040C [56], can automatically measure an I-V curve of one module or several modules connected to a string. From the measuring points it calculates the characteristic data with an accuracy of ±1%. The device presents the P_{MPP}, U_{MPP}, I_{MPP}, U_{OC}, I_{SC}, fill factor FF as well as the internal series resistance R_S and internal parallel resistance R_P, which are also stored for later use. Also the peak power P_{pk} is available with a accuracy of ±5%. To make the values comparable, they can be calculated under Standard Test Conditions (STC): irradiance $E_0 = 1000\,\mathrm{W/m^2}$, module temperature $T_0 = 25°\mathrm{C}$, and spectrum AM=1.5. Therefore, the device includes a Pt1000 temperature sensor. For the irradiance, an external solar radiation sensor SOZ-03 (accuracy of ±5%) which consists of a silicon reference solar cell is used. The accuracy of the I-V curve measurement gets the better, the higher the irradiance is, hence the measurements are preferentially done during summer months [56].

4.2 Material-stability Setup of the Coating

The second main part of this project is dealing with the characterisation of the stability/ageing behaviour of the coating on the backsheets. First, the adhesion of the coating to the weathered backsheet was tested with a specific tape. Moreover, visual inspection with the naked eye and a light microscope was done on a two-monthly basis. Additionally, spectroscopic measurements of IR, NIR, and Raman spectra were performed on a two-monthly basis with portable spectrometers. The advantage of portable devices is that all measurements can be done non-destructively and directly at the test site. The spectra are taken to recognise degradation effects on the coating material.

Section 2.2 describes the theory of the different spectroscopic methods. For comparison, the spectroscopic measurements were also performed on an uncoated reference module of the same PV park (65T2), which will be called *Reference module* in the following. Moreover, the original state of the coating on an aluminium foil and the original state of the backsheet material were measured for comparison. In the following sections, all measurement methods and devices used will be explained in detail. The measurement analysis, as well as the respective results, are presented in Section 5.2.

4.2.1 Adhesion Check-up

To test the adhesion of the coatings on the modules, Tesa Tape 4651 was stuck on the coatings in strips, 15 cm long and 2.5 cm wide. After pressing them there with the ball of the hand and waiting for three minutes, the strips were slowly removed. Finally, the strips were inspected to see whether parts of the coatings had been chipped off. This was not the case. For Remsolar-coated modules we can state that the adhesion of the coating is good. For Dowsil-coated modules the outcome is not so informative, as we observed earlier that adhesive tapes do not stick well to silicone materials.

4.2.2 Visual Inspection

When visiting the test site, the first step was a visual examination of the coated backsides of the modules with the naked eye. Pictures were taken with a camera to record changes in the surface morphology of the coating over time. To investigate the surface in more detail, pictures were also taken with a portable light microscope. Here a PCE-MM 800 digital microscope was used (see Fig. 4.9a). It is directly connected to a laptop via the USB-port and pictures can be taken with the associated software *Measurement*. The microscope can be used with a 20× or 200× magnification. For most pictures, the smaller magnification (20×) was used. Table 4.1 gives an overview of the sample measurements.

Table 4.1: Light microscopic images

Date	Module	Material	Measuring point
Reference measurements			
original state	coating on aluminium foil	Remsolar	distributed places
original state	coating on aluminium foil	Dowsil	distributed places
original state	backsheet	PA	distributed places
13.01.2022	uncoated ref. Module	PA backsheet	busbar/cell
03.03.2022	fresh coated ref. Module 65T6	Remsolar	busbar/ cell
Measurements at the test site			
10.11.2021	Module 1	Remsolar	busbar/cell
10.11.2021	Module 7	Dowsil	busbar/cell
14.01.2022	Module 1	Remsolar	busbar/cell
14.01.2022	Module 7	Dowsil	busbar/cell
23.02.2022	Module 1	Remsolar	cell
10.03.2022	Module 7	Dowsil	busbar

4.2.3 Infrared Spectroscopy

The infrared measurements were done with a handheld Fourier transform infrared (FTIR) spectrometer, A_2 Technologies EXOSCAN [57] (see Fig. 4.9b). A diamond ATR-crystal is brought in direct contact with the sample surface (in this case the backsheet or the coating). The ATR (attenuated total reflection) technique is a surface sensitive method, where only the top 1.5-2.5 µm of the sample are investigated. As a detector a DTSD is used. All techniques are explained in Section 2.2.2.

(a) Measurement with the light microscope on the Remsolar-coated backsheet of Module 1.

(b) Measurement with the EXOSCAN FTIR-spectrometer on the Dowsil-coated backsheet of Module 7.

Figure 4.9: Measurement devices at the test site

For the measurement, the Exoscan instrument was connected to a laptop with the programme *MicroLab PC*. A method *PVRe2 Testanlage* was created with a measurement range of 650 - 4000 cm^{-1} and a spectral resolution of 8 cm^{-1}. Moreover, the number of scans was set to 12 and the valid time for a background scan to one minute. Before each measurement, the crystal was cleaned and a background spectrum collected, with the crystal being not in contact with the sample. Table 4.2 gives a summary of the FTIR measurements performed.

Table 4.2: FTIR measurements

Date	Module	Material	Measuring point
Reference measurements			
original state	coating on aluminium foil	Dowsil	distributed places
original state	coating on aluminium foil	Remsolar	distributed places
original state	backsheet	PA	distributed places
14.01.2022	uncoated ref. Module	PA backsheet	hotspot/crack (busbar)/cell
03.03.2022	fresh coated ref. Module 65T6	Remsolar	over cell
Measurements at the test site			
10.11.2021	Module 1	Remsolar	over cell
10.11.2021	Module 7	Dowsil	over cell
14.01.2022	Module 1	Remsolar	over cell
14.01.2022	Module 7	Dowsil	over cell
10.03.2022	Module 65T6 (1 week in the field)	Remsolar PU	over cell
10.03.2022	Module 1	Remsolar	over cell
10.03.2022	Module 7	Dowsil	over cell

4.2.4 Raman Spectroscopy

The Raman spectroscopic measurements were done with a portable **B&WTEK** i-Raman Plus [58]. The model BWS465-532S excites the Raman signal with a laser at 532 nm. The spectrometer range is 65 - 4200 cm^{-1} with a resolution of 4 cm^{-1} at 614 nm. As a detector, a high quantum efficiency CCD array is used. Figure 4.10 shows the probe connected to the laser with a specific fibre-optic cable. Hence, the Raman device can be 1-2 m away from the sample. In contrast to the ATR technique of the FTIR (which needs direct contact), the maximum Raman signal occurs in the focal point of the laser probe ($\sim$ 1 cm distance to sample surface). So when different spacers are used, also layers beneath transparent material can be measured. For example, the encapsulant of the PV module under the front glass can be inspected, as shown in Figure 4.10b.

For the measurement, the corresponding software BWSpec was used. When the Raman device is turned on, the laser intensity, the integration time and the multiplier can be set. This specifies how long and with which intensity the excitation of the sample is done for the spectrum. In order to make the spectra taken after increasing natural weathering comparable, the setting should stay the same. However, this is sometimes not possible because high fluorescence requires lower intensity or measuring time. Table 4.3 states the measurement dates but also specifies the integration times used. In all measurements, the multiplier was 5 and the laser intensity is 100%. A dark scan was necessary before the measurement. Because the Raman instrument did not work on the general measurement date in January, spectra were instead taken in February.

Table 4.3: Raman measurements with a laser intensity of 100% and a time multiplier of 5.

Date	Module	Material	Measuring point	Integ. Time
Reference measurements				
original state	coating on aluminium foil	Dowsil	distributed places	3 sec
original state	coating on aluminium foil	Remsolar	distributed places	3 sec
original state	backsheet	PA	distributed places	3 sec
13.01.2022	uncoated ref. Module	PA backsheet	under label - busbar/cell	5 sec
13.01.2022	uncoated ref. Module	PA backsheet	weathered - busbar/cell	2 sec
03.03.2022	fresh coated ref. Module 65T6	Remsolar	over cell	3 sec
Measurements at the test site				
10.11.2021	Module 1	Remsolar	over cell	3 sec
10.11.2021	Module 7	Dowsil	over cell	3 sec
23.02.2022	Module 1	Remsolar	over cell	3 sec
23.02.2022	Module 7	Dowsil	over cell	3 sec
23.02.2022	Module 1	encapsulant	over cell	5 sec

(a) Raman laser and laptop running the measurement software BWSpec.

(b) Laser probe measuring the encapsulant of the modules using a specially designed spacer.

Figure 4.10: Measurement with the Raman laser at the test site.

4.2.5 Near Infrared Spectroscopy

The NIR spectroscopic analysis of the coating was performed using a trinamiX near-infrared (NIR) spectrometer (Model SYS-IR-R-P) [59]. Figure 4.11 shows that the device is rather small and measuring in the field is convenient. The spectral range is 1400 - 2500 nm which corresponds to 4000 - 7143 cm^{-1}, the resolution is 1% of the wavelength. An especially by trinamiX created miniaturised infrared detector Herzstück^{TM} detects the reflected light, which is then transformed into an electrical signal. Because of the long wavelengths involved, not only surface material can be inspected but the light can enter the material deeper until it is reflected by opaque material e.g. the Si-cell. For additional comparison, spectra were therefore taken of the EVA encapsulant of the modules.

The measurement operates with a mobile device using the trinamiX Software App. The spectrometer was connected via Bluetooth and, after calibration with a dark measurement and a reflectivity standard, is ready for use on the sample. Table 4.4 gives a summery of all NIR measurements. Of each measurement place and material (backsheet, coating, encapsulant), ten spectra each were collected for better accuracy.

Table 4.4: NIR measurements

Date	Module	Material	Measuring point
Reference measurements			
original state	coating on aluminium foil	Dowsil	
original state	coating on aluminium foil	Remsolar	
original state	backsheet	PA	
13.01.2022	uncoated ref. Module	PA backsheet	cracks/hotspots
13.01.2022	uncoated ref. Module	PA backsheet	busbar
03.03.2022	fresh coated ref. Module 65T6	Remsolar	thick & thin coating layer
Measurements at the test site			
10.11.2021	Module 1	Remsolar	
10.11.2021	Module 7	Dowsil	
14.01.2022	Module 1	Remsolar	
14.01.2022	Module 7	Dowsil	
14.01.2022	Module 1	EVA encapsulant	front side - cell
14.01.2022	Module 7	EVA encapsulant	front side - cell
10.03.2022	Module 65T6 (1 week in the field)	Remsolar	thick & thin coating layer
10.03.2022	Module 1	Remsolar	
10.03.2022	Module 7	Dowsil	
10.03.2022	Module 1	EVA encapsulant	front side/ cell
10.03.2022	Module 7	EVA encapsulant	front side/ cell

Figure 4.11: Measurement with the NIR-spectrometer on the Remsolar-coated Module 1.

Chapter 5

Measurement Results and Interpretation

This chapter deals with the analysis of the measurement results and their interpretation. First, we discuss the electrical measurements of the whole test site and then, second, the ageing behaviour of the coating on the backsheets of the modules.

5.1 Analysis of the Electrical Characterisation

The analysis starts with the initial electrical measurements of the test site, the wet leakage test and the I-V curves. Then some representative days and times were chosen to analyse the continuously recorded data.

5.1.1 Wet Leakage Test

Regaining the electrical insulation properties was the foremost aim for the coating of the cracked backsheets. Tests on reference modules with cracked backsheets of the very same PV park in Germany done in the PVRe^2 project had shown that the insulation resistance is often 0 or 0.1 Ω.

Each reference module was tested in a tank with 9 litres of water according to the MQT 15 test [14]. After coating Modules 1-12 and installing them at the test site, the MQT 15 test was repeated. As we did the test in the morning at the end of November the coated backsheets were wet by dew. This was sufficient for the test, so no water tank was necessary and the mounted modules could directly be tested. The representative modules Module 1 (Remsolar) and Module 7 (Dowsil) showed more than 200 MΩ insulation resistance, which was the upper detection limit of the used measuring device and sufficient by far to pass the test ($> 24.5\,\mathrm{M\Omega}$ for $A = 1.653\,\mathrm{m}^2$). We also measured the whole string of all twelve modules two times and recorded an insulation resistance of 84 MΩ and 112 MΩ. Here $> 2.0\,\mathrm{M\Omega}$ for $A_{total} = 19.62\,\mathrm{m}^2$ would have been sufficient to pass the test. Therefore, it can be stated that both coatings restored the insulation resistance of the modules.

5.1.2 I-V Curve

Directly after the modules had been mounted at the test site in July 2021, I-V Curve measurements were done with the setup described in Section 4.1.5. Table 5.1 presents the measured and calculated data of the whole string of all 12 modules as well as Module 1 and Module 7 separately. All values have an uncertainty of ±1%, except for the irradiance with ±5%.

Table 5.1: Characteristic electric data of the coated modules as derived from the I-V Curves

	String (all 12 modules)	Module 1, M1	Module 1, M2	Module 7, M1	Module 7 M2
E_{eff} [W/m^2]	797	771	794	775	770
T_{mod} [°C]	50.2	51.8	52.1	50.8	51.2
P_{MPP}[W]	1875.1	151.8	155.7	154.7	153.3
U_{MPP}[V]	306.0	25.3	25.3	25.5	25.5
I_{MPP}[A]	6.13	6.00	6.16	6.07	6.00
U_{OC}[V]	389.1	32.4	32.5	32.6	32.6
I_{SC}[A]	6.79	6.52	6.71	6.56	6.51
FF [%]	73.33	73.63	73.50	73.84	73.89
R_S [Ω]	6.26	0.53	0.53	0.52	0.53
R_P [Ω]	3548	345	342	311	336
P_p [W/m^2]	2618.4	220.6	220.1	222.9	222.4
η [%]	13.3	13.5	13.5	13.6	13.6

From the measured P_{MPP} at specific meteorological conditions (given in Table 5.1) the nominal power P_p, at STC conditions could be calculated by the following equation:

$$P_p = P_{MPP} \cdot \frac{E_0}{E_{eff}} \cdot [1 + \kappa_{MPP} \cdot (T_0 - T_{mod})] \tag{5.1}$$

with the irradiance $E_0 = 1000\,\mathrm{W/m^2}$, the temperature $T_0 = 25°\mathrm{C}$ and the relevant temperature coefficient $\kappa_{MPP} = -0.0045\,\mathrm{K^{-1}}$. The results are presented in the bottom row of Table 5.1. Compared to the initial values for each module ($P_{Pinitial} = 240\,\mathrm{W}$), the nominal power of a single module was reduced only by 8.4% (after nine years in the field and the repair process). The remaining efficiency of a module was calculated by dividing the nominal power through the module area ($A = 1.635\,\mathrm{m^2}$) and the standard irradiance: $\eta = \frac{P_p}{A \cdot E_0}$.

Besides the characteristic data also all data points of the I-V curves of the modules were available. For each curve, 100 data pairs were recorded. Figure 5.1 shows the curves as taken in July 2021. In follow up work the curves are compared to I-V curves of the uncoated reference modules at standard test conditions [49].

Moreover, the I-V curves were measured in July 2021 because high irradiance is necessary. To analyse how the coating of the backsheets is influencing the module performance not only at the MPP but along the whole I-V curve, measurements should be repeated at least once per year.[3] For continuous analysis, the data gathered every ten seconds at the MPP was used because it is available all around the year.

---

[3] The I-V measurement was repeated one year later in July 2022. Comparison at STC showed no changes of the electrical parameters beyond the measurement uncertainty, see [49].

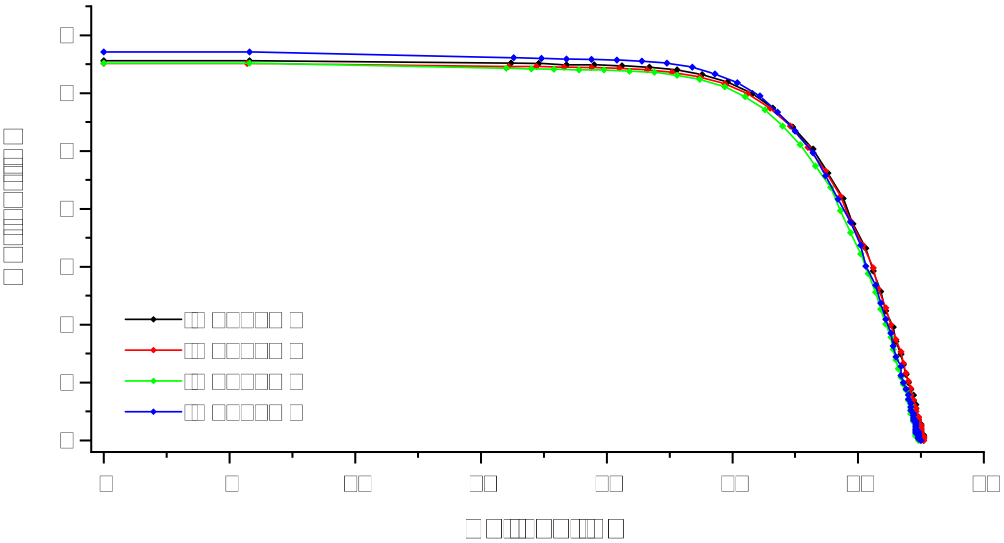

Figure 5.1: I-V curve measurements of Module 1 (Remsolar) and Module 7 (Dowsil) in July 2021 at the meteorological conditions stated in Table 5.1.

5.1.3 Analysis of the Continuously Gathered Data

As described in Section 4.1 characteristic data of the test site and the meteorological conditions were measured every 10 seconds and stored in the InfluxDB database. For further analysis, the data can be visualised, averaged, and downloaded as a csv-file from Grafana. To analyse the performance of the test site over one day in detail, 21.03.2022 between 06:00 and 18:00 was chosen as a representative day. To smooth statistical fluctuations, the median over one minute was calculated by Grafana for all gathered data. These values were downloaded in a csv-file and used for further calculations with Excel.

Temperature and Irradiance

First, the temperature sensors at the backsheet were checked. The graph of all five sensors over the whole day was analysed (Fig. 5.2). Sensor 1 shows a temperature line more similar to the ambient temperature than to the other backsheet temperatures. Therefore, it was concluded that the sensor had fallen down on the roof. Sensor 4 recorded a temperature a bit lower than the other backsheet-mounted sensors and followed some ambient-temperature changes and was rather noisy. One interpretation could be that the sensor was sticking to the coated backsheet but there was still a small gap was in between the sensor and the coating.

Therefore, only the output of Sensors 2 (Module 7) and 3 (Module 1) was used for further calculations. The largest difference between ambient temperature and average module temperature was 10.75°C at 12:53. This difference, however, can get much larger in summer when the irradiance is higher.

It can be said that the temperature measurement with the DS18B20 T-sensors works well. However, a better construction should be found for the sensors measuring the Dowsil-coated modules to achieve continuous data. Furthermore, the sensors should be checked at least monthly whether they still stick to the coating properly.

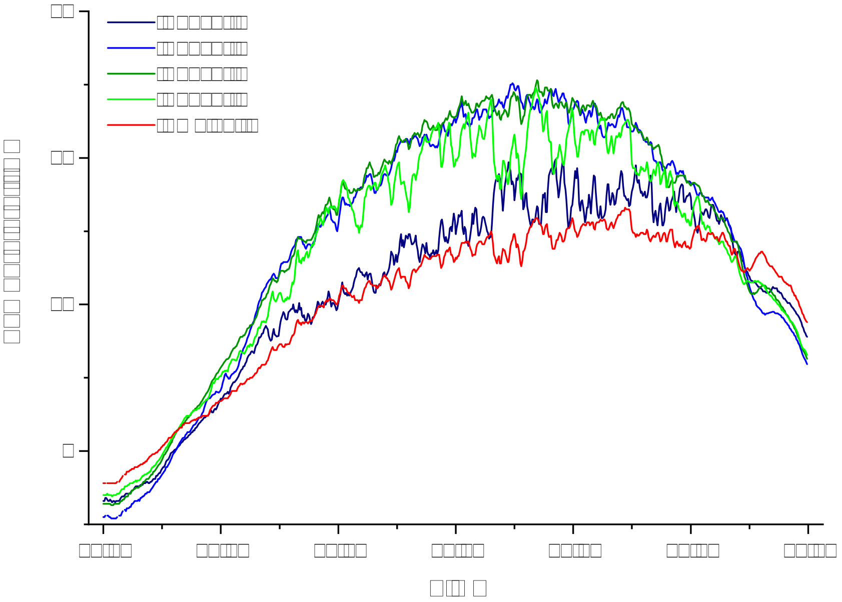

Figure 5.2: Temperature profile of all five temperature sensors (Sensor 1 and 2 on Module 7; Sensor 3 and 4 on Module 1) on 21.03.2022.

Figure 5.3 shows the irradiance on that day. It was compared to open source data of two different pyranometer. Data by ZAMG (Zentralanstalt für Meteorologie und Geodynamik) was used because averaged data over 10 minutes is available open source [60]. The nearest measuring station (Stammerdorf) is only 1.2 km away from the test site, which makes the data well comparable. Nevertheless, the data can only be compared on days with a clear sky (which 21.03.2022 was), because otherwise the clouds passing over the sky would corrupt the data. The second pyranometer is from another ZAMG station in Vienna (Hohe Warte - 6.6 km away). The small negative peak at 16:50 in the irradiance of the test site originates from the tall, thin chimney next to the test site, which throws a shadow on the pyranometer for around 15 minutes every day. Otherwise, the measured irradiance of the test site lies in between the graphs of the two official measuring stations and the error bar (3.11%) is sufficient. This shows that the data gathering with the pyranometer LP PYRA 03 and the analogue-digital-converter ADS1115 works well. Therefore, it can be used for further calculations without any doubts. Figure 5.4 shows the measured irradiance in comparison with the generated power; the maximum value at that day was 731 W/m^2 at 12:11.

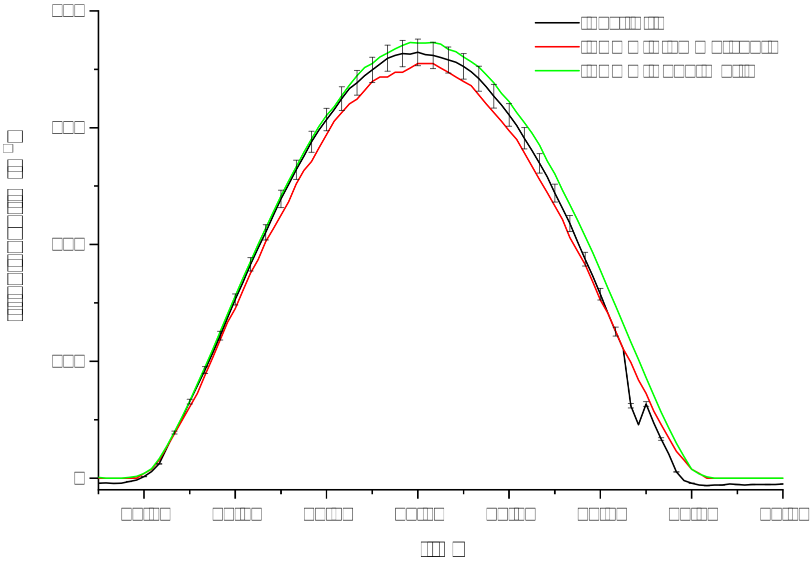

Figure 5.3: Irradiance at the test site in comparison to two ZAMG monitoring stations on 21.03.2022.

Generated Power of the Test Site

The first step was to compare the generated power before (DC) and after (AC) the conversion at the inverter (see Figure 5.4). The loss factor of the conversion is the efficiency of the inverter. According to the datasheet of the inverter [44], the efficiency depends on the generated power. Between 1000 and 2000 W generated power the efficiency should be between 95.5% and 96.5%. With less generated power, the efficiency decreases abruptly. This feature could be observed when analysing the data during the whole day. The relative difference between DC and AC power was calculated by

$$\Delta_{DC-AC} = \frac{DC - AC}{DC} = 1 - \frac{AC}{DC}. \tag{5.2}$$

The mean was calculated to 0.0451 for the time between 10:00 and 15:30 because the power was between 1000 and 2000 W in this time intervall (see Fig. 5.4). This results in an efficiency of the inverter of 95.49%, which fits quite well to the datasheet values. When the test site produces only around 100 W DC power, the efficiency of the inverter is only around 66.3%. Figure 5.5 shows the progression of the efficiency over the whole day, with the abrupt decrease visible.

As for the calculation of the efficiency similar numbers (DC, AC) are subtracted the uncertainty of these values cannot be ignored. Hence the uncertainty of the inverter measurement of 3% for the DC and AC power should be used for error propagation of Equation 5.2:

$$\sigma_\Delta = \sqrt{\sigma_{AC}^2 \cdot \left(\frac{1}{DC}\right)^2 + \sigma_{DC}^2 \cdot \left(\frac{AC}{DC^2}\right)^2}. \tag{5.3}$$

In the time interval (10:00 - 15:30) the uncertainty of the calculated mean was derived to be 0.042. Here the error of the mean was calculated with the square route of the mean of the variance of the single data points plus the variance of the mean:

$$\sigma_{\bar{\Delta}} = \sqrt{\sum_{j=1}^{m} \frac{\sigma_{\Delta_j}^2}{m} + \sum_{j=1}^{m} \frac{\left(\bar{\Delta}_j - \bar{\Delta}\right)^2}{m}} = 0.042. \tag{5.4}$$

This point out that the uncertainty is as large as the value itself, so the efficiency of the inverter needs to be looked at with caution. However, Figure 5.5 shows that the calculation of the mean seems reasonable. It can be assumed that the uncertainty of 3% is rated rather large and that the actual values are more precise than given.

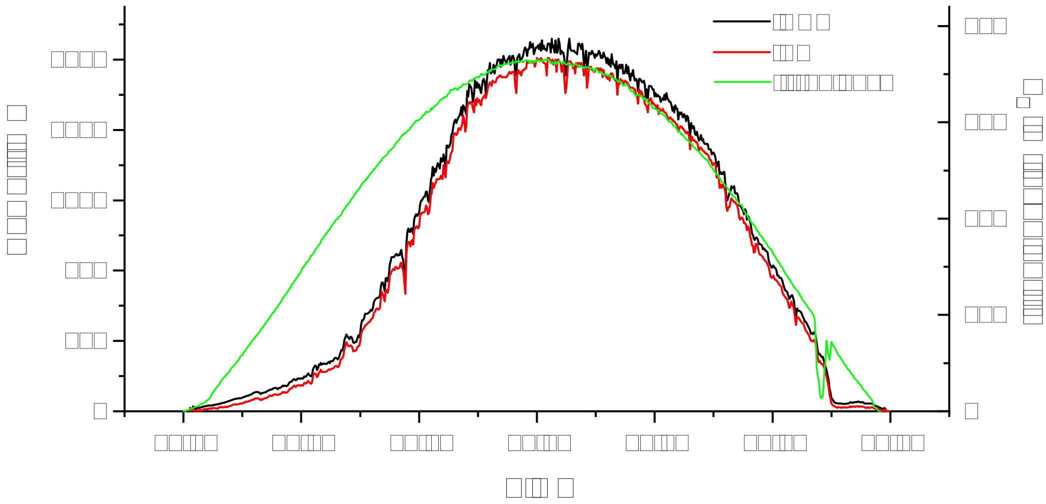

Figure 5.4: Comparison of the generated power before (DC) and after (AC) conversion of the inverter. The comparison with the irradiance shows the power that could have been produced without any shading.

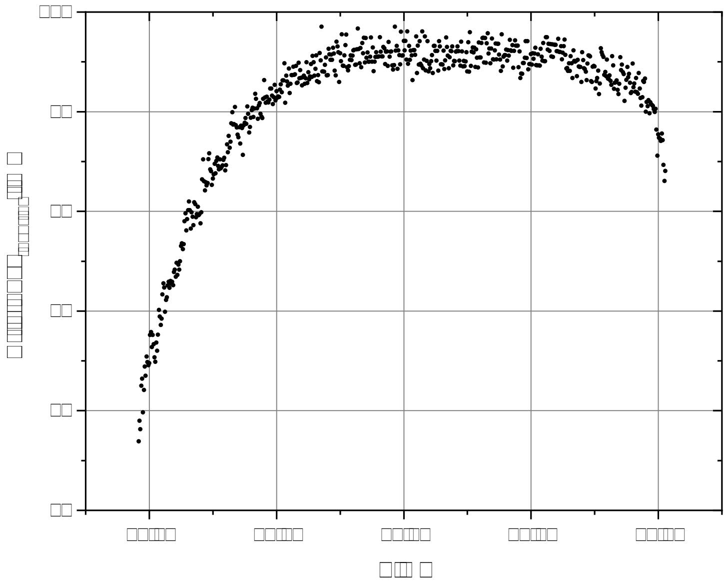

Figure 5.5: Efficiency of the Fronius inverter dependent on the generated power.

Partial Shading of the Test Site - Loss of Produced Energy

Another noticeable effect in Figure 5.4 is that the test site produces less power in the morning hours than in the afternoon. This originates in the partly shading of the test site by a tree in the east of the test site. As the pyranometer is not shaded, it shows how much power could have been generated in these hours. To calculate the energy loss due to the shadow, the irradiance was multiplied with a factor so the AC power and the irradiance curve overlap in the early afternoon. For 21.03.22 this factor was determined to be 2.75. Then Origin was used to calculate the produced energy according to the AC power curve and the irradiance curve. With the available peak analysis tool in Origin, the integral of both curves was calculated between 6:00 and 18:00. The integral of the AC power curve was 11.41 kW h. This coincides almost perfectly with the *energy per day* value (11.4 kW h) read from the Modbus protocol. However, the integral of the irradiance curve was 14.29 kW h, which is quite a big difference. These values are only estimations, but it can be stated that due to the shadow quite a lot of energy ($\sim 20\%$ on 21.03.2022) is not produced during each day. The amount changes during the year, so the difference should also be calculated during other times of the year. Especially because the tree was still without leaves on 21.03.2022.

Therefore, a comparison was made with a winter day. The first really sunny day since the installation of the data gathering was 13.02.2022. According to the *energy per day* value, the generated energy on this day was 6.87 kW h. The integral of the AC curve gave the value 6.88 kW h and the one of the converted irradiance curve (this time with a factor of 2.9) 8.25 kW h. So even in winter about 1.37 kW h (16.6%) were not produced. The same should be done in summer when the tree is full of leaves and the irradiance and the sun hours per day are higher.

In general, it is evident that the shadow on the test site is a problem for optimum energy yield. Moreover, the fact that the data in the mornings is corrupted affects the evaluation of the daily performance of the coated modules. Thus, this shading has to be considered for all further calculations and estimations.

Calculation of the Nominal Power

Additionally, the nominal power of the test site on 21.03.2022 was calculated to the minute. The produced power of the modules (DC) P_{MPP}, the measured irradiance E_{eff}, and the average module temperature of Sensors 2 and 3 (T_{mod}) were inserted in Equation 5.1. Then the uncertainty of the nominal power could be calculated with error propagation by the following equation:

$$\begin{aligned}\sigma_{Pp} &= \sqrt{\sigma^2_{Pmpp}\left(\frac{\partial Pp}{\partial p_{mpp}}\right)^2 + \sigma^2_{Eeff}\left(\frac{\partial Pp}{\partial Eeff}\right)^2 + \sigma^2_{Tmod}\left(\frac{\partial Pp}{\partial Tmod}\right)^2} \qquad (5.5)\\ &= \left\{\sigma^2_{Pmpp}\cdot\left[\frac{E_0}{E_{eff}}\cdot\left(1+\kappa_{mpp}\left(T_0-T_{mod}\right)\right)\right]^2\right.\\ &\left.+\,\sigma^2_{Eff}\cdot\left[P_{mpp}\cdot(-1)\frac{E_0}{E^2_{eff}}\cdot\left(1+\kappa_{mpp}\left(T_0-T_{mod}\right)\right)\right]^2+\sigma^2_{Tmod}\cdot\left[P_{mpp}\cdot\frac{E_0}{E_{eff}}\cdot\kappa_{mpp}\right]^2\right\}^{1/2}.\end{aligned}$$

The uncertainties of the used values are $\sigma_{Pmpp} = 3\%$, $\sigma_{Eeff} = 3.11\%$ and $\sigma_{Tmod} = 0.5°\mathrm{C}$. Shortly after sunrise and before sunset, when the incidence angle of the sun onto the modules was quite flat, the power production of the modules was low. However, the pyranometer could still detect irradiance at these angles. Therefore, in these hours the calculation of the nominal power was not reasonable. For 21.03.2022, calculations were therefore only done between 07:30 and 16:30. Figure 5.6 shows the calculated values in this time interval. Without any losses, the nominal power should always result in the same value and the plot should be a straight line. Because of the smaller efficiency of the inverter at lower generated power, this maximum value cannot be achieved at smaller irradiance. Moreover, also the modules have less efficiency in these cases (97% of the normal efficiency at $200\,\mathrm{W\,m^{-2}}$ [32]). The partly shading of the test site in the morning again has the greatest influence. This is the reason why the nominal power in the morning is much lower than in the afternoon, despite the same solar altitude. How the graph would look without the shading effect is drawn with a trend line in Figure 5.6.

The maximum DC power generated on this day was 2120 ± 64 W at 12:33, with the nominal power at STC of 2925 ± 127 W. As the uncertainty can get quite large, and also Figure 5.6 shows that the data has some outliers, it is more reasonable to calculate the mean in the time where the power/time plot has its plateau. Between 12:00 and 15:00 the mean was 2852 ± 133 W. Here the error of the mean was calculated like explained in Equation 5.4 to:

$$\sigma_{\bar{P}p} = \sqrt{\sum_{j=1}^{m} \frac{\sigma^2_{\bar{P}p_j}}{m} + \sum_{j=1}^{m} \frac{\left(\bar{P}p_j - \bar{P}p\right)^2}{m}} = \sqrt{15236 + 2333} = 133\,\mathrm{W}. \tag{5.6}$$

Calculating the nominal power is a good way to compare the efficiency of the test site over time. Comparing the calculated value at a day x to the one from the measurement at the installation day in July 2021 (Table 5.1) shows that the power did not decrease over time. It even had a lower value then, which can be attributed to the different and less accurate measurement procedure in July. To follow the efficiency of the test site, this procedure should be done on a regular basis. Therefore, also a Node-Red Flow should be programmed to automatically calculate the result, for example, once per day.

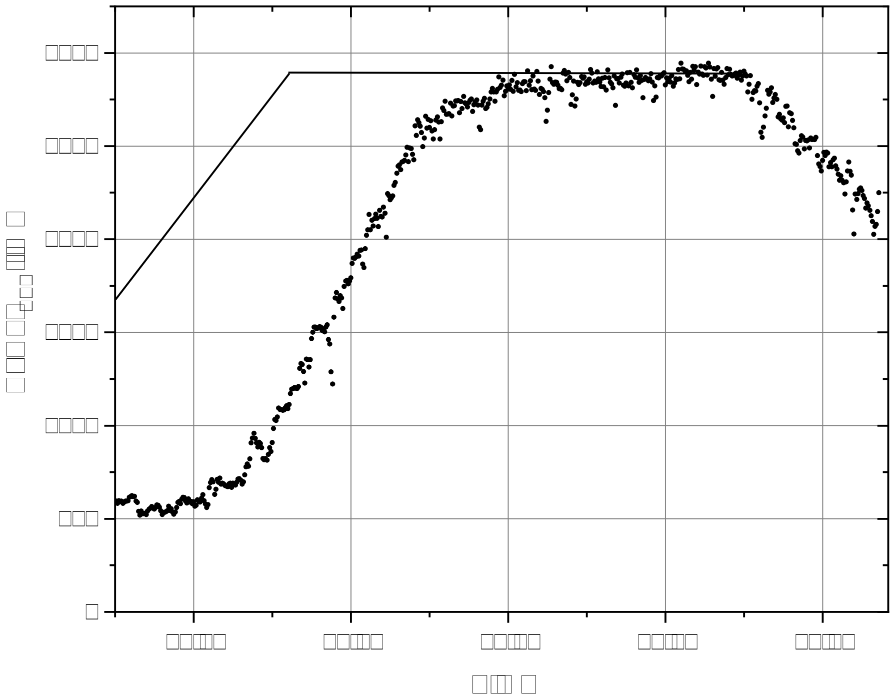

Figure 5.6: Calculated nominal power for every minute on 21.03.2021 between 07:30 and 16:30. The trend line presents how the data would look without the shading.

5.2 Analysis of the Coating-stability Measurements

As described in Section 4.2, various characterisation measurements were done on the uncoated and coated backsheets of the test modules to analyse the stability of the coating materials and their long-term reliability. Visual changes were documented and analysed with a light microscope, and chemical degradation was monitored with three different spectroscopic methods, NIR, IR, and Raman. For all of them, several spectra of each coating were taken on each measurement date, from which one representative spectrum was chosen for further analysis. For the data treatment, the Perkin Elmer Spectrum software [61] and Origin [28] were used.

5.2.1 Backsheet of the Uncoated Reference Module

As a reference, the backsheet of an uncoated but identically weathered reference module (65T2) taken from the same solar park was also characterised. The reference module was mounted close to the repaired modules in the solar park, therefore, it had the same age, induced stress on the module and bill of materials (described in Section 3).

Visual Inspection

The weathered (nine years in the field) polyamide (PA) backsheet showed visible degradation effects, like chalking, deep longitudinal cracks along the busbars and microcracks in between, comparable to [10]. Furthermore, there were even some areas with severe electrical defects detectable, called *hotspots* in the following. A hotspot occurs if the short circuit current of one single cell is lower than the operating current of the module. Then the power generated in the other cells is transformed into heat by the affected cell [31]. Chalking occurs because of the enrichment of the TiO_2 filler in the surface layer as the polymer has decomposed upon photodegradation [10, 34]. Figure 5.7 shows the different crack types recorded with the light microscope.

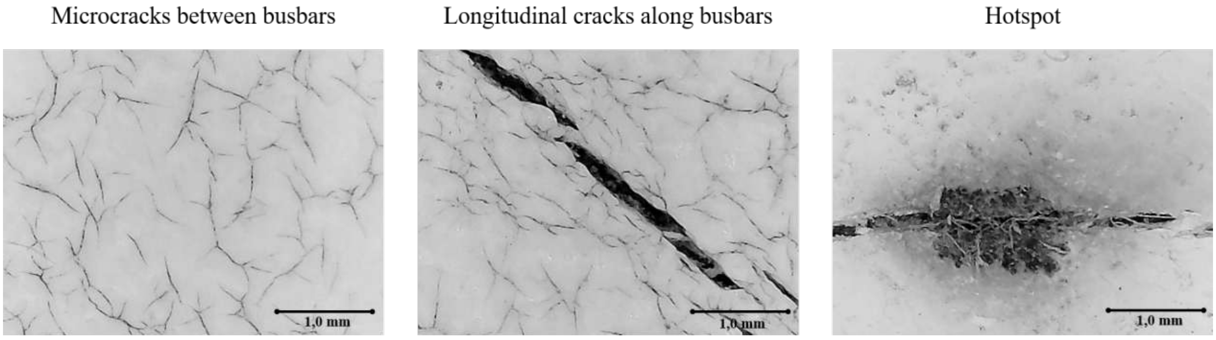
Microcracks between busbars

Longitudinal cracks along busbars

Hotspot

Figure 5.7: Uncoated reference module: light microscopic images of different crack types of the weathered PA backsheet.

Analysis of Raman Spectra

Table 4.3 shows the Raman spectra collected on the reference module. Because the label of the aged PV module was still sticking on the backsheet, it could be removed and an unweathered surface was exposed for reference measurements to analyse any weathering-induced differences. This area of the backsheet undergoes the same temperature stresses in the field but no irradiance can touch this small part of the backsheet. So if the spectrum of the surface under the label differs from the one on the irradiated backsheet, these material changes are due to the impact of the indirect sunlight. Figure 5.8 shows these spectra in comparison with measurements done on an unaged original PA backsheet.

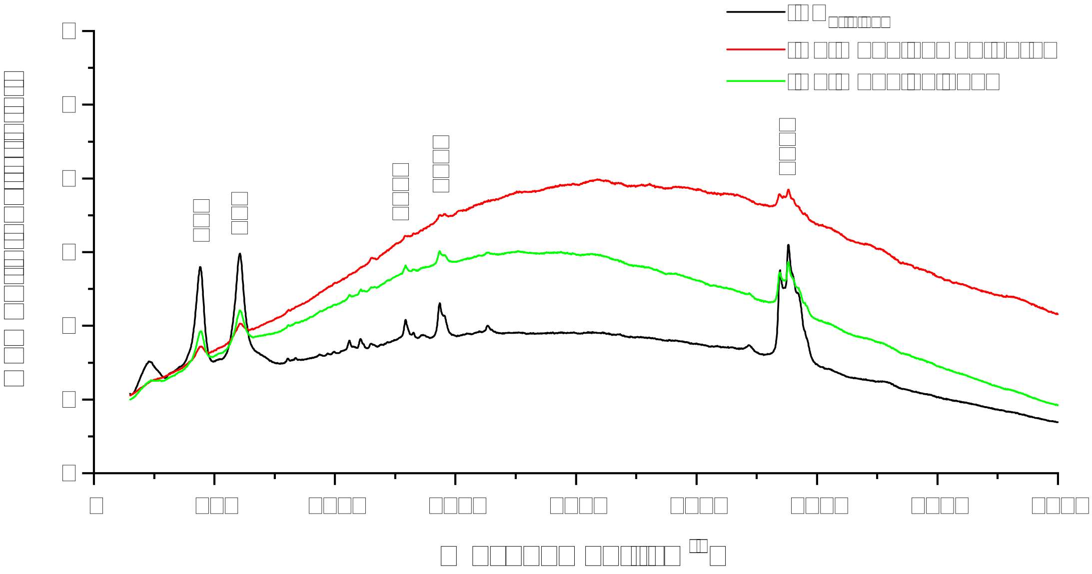

Figure 5.8: Raman spectra of the uncoated PA backsheet of the reference module weathered (red) and under the label (green) in comparison with the original PA backsheet (black).

The first noticeable difference visible in the spectra of the reference module backsheet compared to the original spectrum was the high overall fluorescence. This is typical for aged backsheets in the field because degraded polymers (backsheet and encapsulant) develop fluorophores [62]. This leads to a broad absorption resulting in a highly bent baseline (see Section 2.2). As depicted in Figure 5.8, the spectrum of the weathered backsheet has the most fluorescence, followed by the spectrum taken under the label. The unaged original backsheet though only has little fluorescence. Also the laser intensity has an effect because the fluorescence depends on the laser intensity and integration time applied as bleaching may take place.

To make the single bands better comparable, the first analysis step of the Raman spectra was a baseline correction (to remove the fluorescence). With all three available spectra analysis programmes, the Raman software BWspec, the Perkin Elmer Spectrum software, and Origin baseline correction can be performed and were compared. In the end, the best solution for a reliable baseline correction was obtained with the Perkin Elmer Spectrum software. In this way, the baseline could be fitted best without manipulating the data. Then, the spectra were normalised on the CH band (2882 cm^{-1}) for better comparison (see Fig.5.9a) and then the peaks analysed in Origin.

The second step of the analysis was the comparison of the visible bands. The TiO_2 peaks at 441 cm^{-1} and 606 cm^{-1} can only be analysed with Raman spectroscopy, because they are outside of the measurable IR range (see Section 4.2.3). To find out whether the amount of TiO_2 in the backsheet surface changed (which is assumed because of the chalking) the area and height of the peaks were compared to the CH peak at 2882 cm^{-1} [63]. This was done with the peak analysis tool in Origin (see Fig. 5.9b). Only the ratio of the peak area and height were compared on the different samples, because of the different spectra intensity. Table 5.2 shows that both, area and height ratio, increase from the unaged original backsheet (three different samples) to the shielded backsheet under the label and even more to the weathered backsheet (cell and busbar/crack). This means that the amount of TiO_2 in the surface near region decreases. This is the case because the chalk powder (mostly TiO_2 particles as described in Section 3.1.1) on the surface was washed away (or wiped off) so less TiO_2 remained in the material. Because the

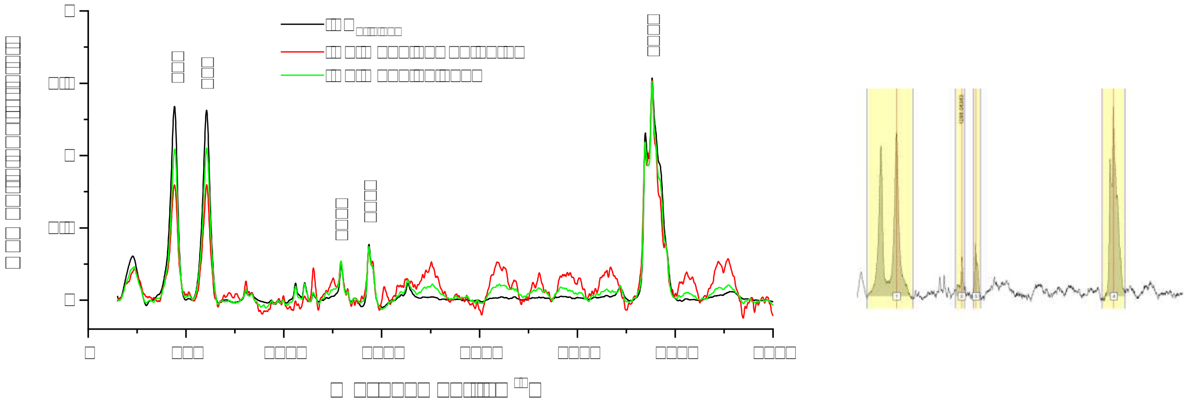

(a) Normalised Raman spectra, baseline corrected. (b) Peaks integrated in Origin.

Figure 5.9: Raman spectra analysis to compare the amount of TiO_2 in the backsheets.

chalking is linked with the crack formation in the backsheet this is a strong sign for a beginning degradation of the backsheet [34]. Also the CH peaks at $1293\,\mathrm{cm}^{-1}$ and at $1435\,\mathrm{cm}^{-1}$ were integrated in Origin and compared to the TiO_2 peaks. As the CH peaks originate from the PA-polymer, the same trend of decreasing TiO_2 was observed, but with less intensity.

Table 5.2: Analysis of the amount of TiO_2 in the backsheets (surface near region).

Measurement Place	Ratio Area $\frac{A(\mathrm{CH}_{2882})}{A(\mathrm{TiO}_2)}$	Ratio Height $\frac{H(\mathrm{CH}_{2882})}{H(\mathrm{TiO}_2)}$
$\mathrm{BS}_{original}$ B2a	0.65	0.96
$\mathrm{BS}_{original}$ B2b	0.68	1.00
$\mathrm{BS}_{original}$ B20b	0.66	0.98
Refmodule_label-bus1	0.87	1.26
Refmodule_label-bus2	0.79	1.16
Refmodule_label-cell	0.81	1.17
Refmodule_weathered-crack1	1.22	1.63
Refmodule_weathered-crack2	1.21	1.69
Refmodule_weathered-cell	1.08	1.63

In conclusion, it can be stated that Raman spectra are suitable for early degradation detection of weathered PA backsheets. The analysis of the amount of chalking on the backsheet works well and can be a pre-sign for crack formation. This could help to start a preventive repair process of affected modules which would give better repair results. Furthermore, the impact of the indirect irradiance on the degradation process is shown by analysing the shielded backsheet area under the label. This proves that not only temperature changes but also the irradiance has a significant impact on the degradation of the PA backsheet.

Analysis of Infrared Spectra

Also, infrared spectra of the uncoated but aged backsheet of the reference module were recorded and analysed. Here measurements were taken over the busbars (cracks), the hotspots, and the cells (see Tab. 4.2). These spectra are first compared visually. As described in Section 2.2 peaks of the polar C=O and N-H groups of the polyamide have higher relative intensity in the

IR spectrum than in the Raman spectrum. Therefore, IR spectroscopy can be used better to identify the polyamide or special additives as well as their chemical degradation. Figure 5.10 shows the characteristic bands of the PA backsheet visible in the IR spectrum. They can be associated with specific parts of the polyamide structure (see Table 5.3 [36, 63]).
To analyse how the PA backsheet changed after nine years in the field, the spectra of the backsheet were compared to a measurement of an unaged original backsheet. Because the intensity of the absorption bands can vary in dependence of the size of the contact area of the ATR-crystal on the backsheet surface, it is not possible to directly compare these spectra without normalisation. Unfortunately, for the spectra of the hotspot area the intensity of the peaks was much weaker than in the other spectra (see Fig. 5.10) as a small hole is burnt into the backsheet and, thus, it is not possible to attach the whole ATR-crystal flat on the backsheet.

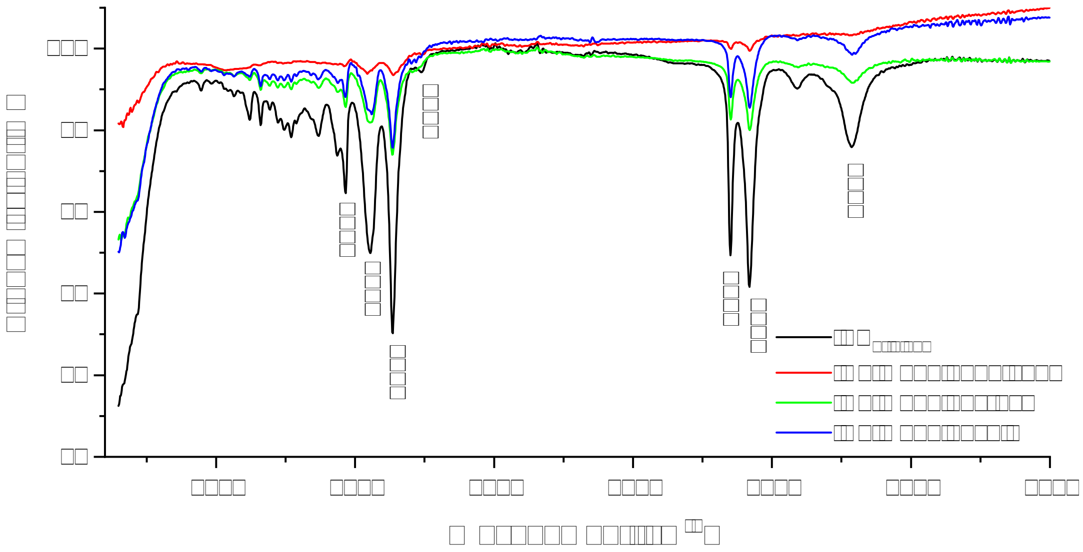

Figure 5.10: Infrared spectra of different sample positions of the uncoated but aged PA backsheet of the reference module compared to the original unaged PA backsheet (black).

Table 5.3: Assignment of the IR peaks of the PA backsheet [36][63].

Wavenumber [cm^{-1}]	Functional groups
1466	CH absorption
1553	amide II (NH stretching)
1635	amide I (C=O stretching)
1740	C=O carbonyl from additive in backsheet
2850	CH$_2$ streching
2917	CH$_2$ and CH streching
3280	NH streching

To analyse in detail the ageing-induced spectral changes of PA, especially in the crack area, these spectra were compared to a spectrum of the unaged original backsheet. Therefore, first the spectra were normalised to the amide I band at 1635 cm^{-1} to 60% transmission. This band was chosen because the amide I normally does not change upon weathering. The upper part in Figure 5.11 shows the differences in the spectra of the backsheet already more clearly. To get more detailed information a difference spectrum was calculated of the two normalised spectra. In this case, the crack spectrum was subtracted from the original one (see the lower part of Figure 5.11).

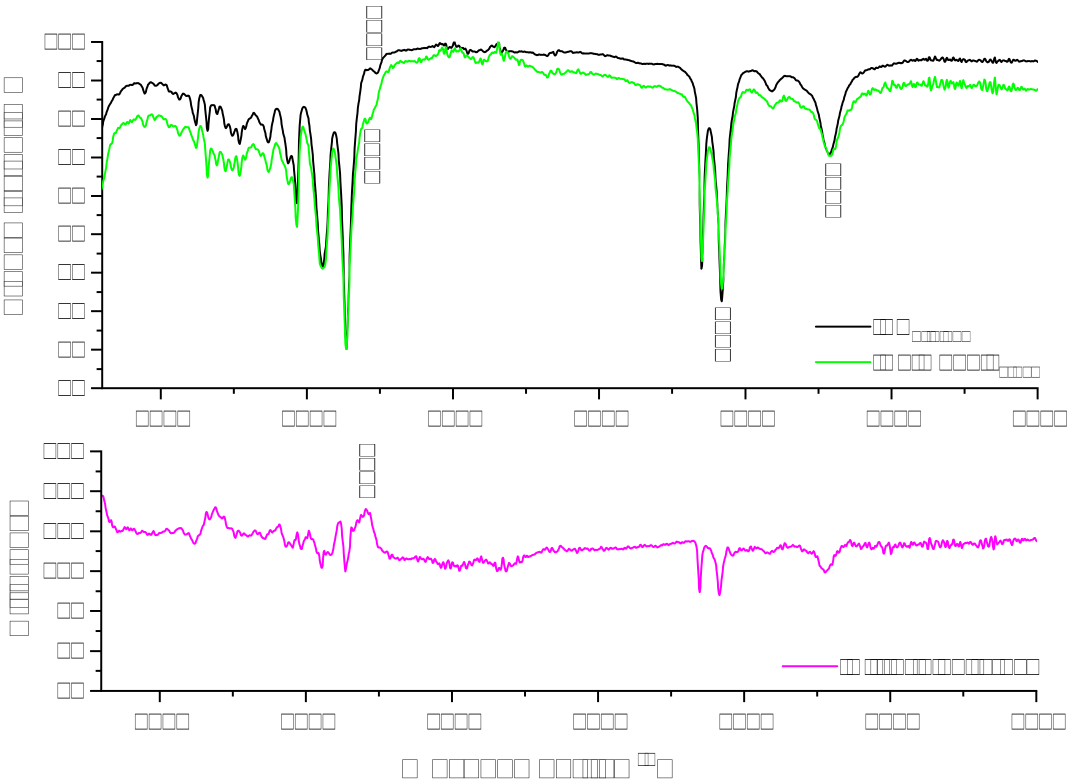

Figure 5.11: Difference spectrum of the infrared spectra in the crack area of the aged reference module's backsheet and the original unaged backsheet.

The difference spectrum shows an additional peak at 1710 cm^{-1} which is attributed to a carbonyl band (C=O stretching) that emerges by photo-oxidative degradation of polyamide, as described in Section 3.1.1 [10]. Moreover, the degradation causes some relative intensity changes, as the NH band at 3280 cm^{-1} or the CH_2 stretching bands.

In conclusion, the analysis of the infrared spectra allows for the detection of chemical changes in the polar groups. With the detection of additional bands, like the carbonyl band, chemical degradation of the backsheet material can be proven. Difference spectra are an important tool in making such small changes visible.

Analysis of Near Infrared Spectra

As the last step, the NIR spectra of the unaged and aged backsheets were analysed. Because of the longer wavelength of the light in the NIR range (Section 2.2), the NIR spectrum also shows information from deeper layers inside the module (the whole backsheet and encapsulant). However, as only overtones and combination bands of specific bands lie in the NIR range no sharp peaks are visible so specific band assignment is difficult.

The spectrum of the uncoated but aged backsheet was compared with the unaged original backsheet (see Fig. 5.12). The original backsheet was not measured as a part of a module but as single component lying on top of a solar cell, to reflect the NIR light. Therefore, the influence of the bands of the EVA encapsulant on the spectra of the weathered backsheet (as part of the reference module) had to be analysed. As shown in Figure 5.12 the spectrum of the aged backsheet does not differ from the one of the unaged original backsheet. Therefore, it can be safely assumed that the influence of the EVA is negligible.

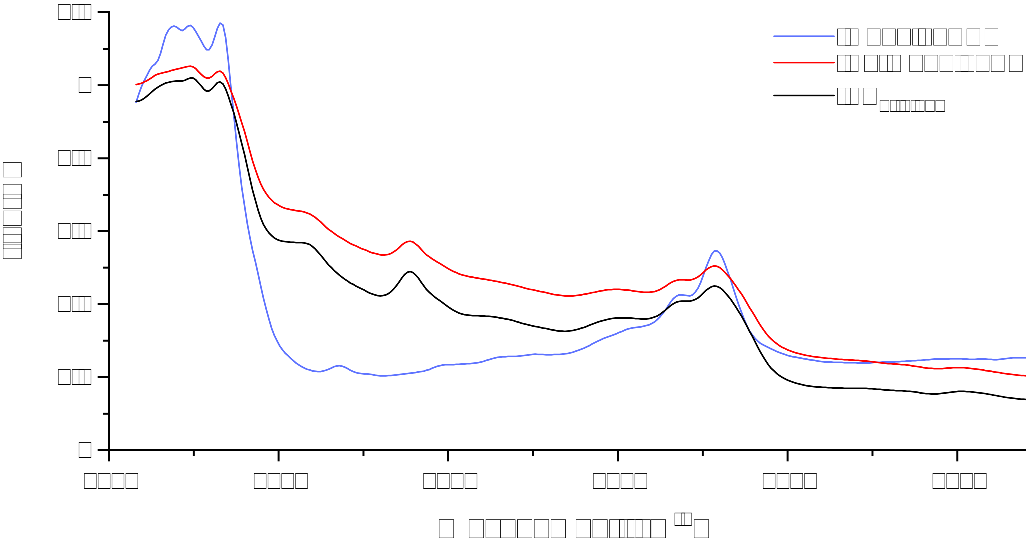

Figure 5.12: NIR spectra of the aged PA backsheet in comparison with spectra of the unaged original backsheet and the EVA encapsulant.

5.2.2 Analysis of the Remsolar Polyurethane Coating on the Backsheet

Visual Inspection

The first step in the material analysis of the Remsolar coating was the visual inspection of the coated backsheets. Module 1 of the test site was chosen as representative for all Remsolar-coated modules because it is easy to access on the edge of the roof. The whole backsheet area was checked with the naked eye for any abnormalities on a two-monthly basis. Additionally, we took light-microscopic images over the busbars and the cell (between the busbars)(see Table 4.1). Until mid January (six months after coating and installation at the test site) the coating did not show any visible changes. However, at the next inspection in the middle of February, at the coating on Module 1 some bubbles were detected, which looked like small black craters and could easily be detected with the naked eye and with a standard camera.

Further visual investigations of the whole test site showed that all Remsolar-coated modules exhibited such bubbles spread over the whole backsheet with different occurrence densities. To analyse the structure of the bubbles in more detail, light microscopic images were taken one week after the first detection. Figure 5.13 shows the light microscope images on the three analysis dates (in November, January, and February). Here in the two images on the left the coating looks rather intact although some small black dots were already visible. Therefore, it can be assumed that the bubbles started to grow already earlier, but were too small to be detected by the naked eye or were first mistaken for dirt particles in the light microscopic images.

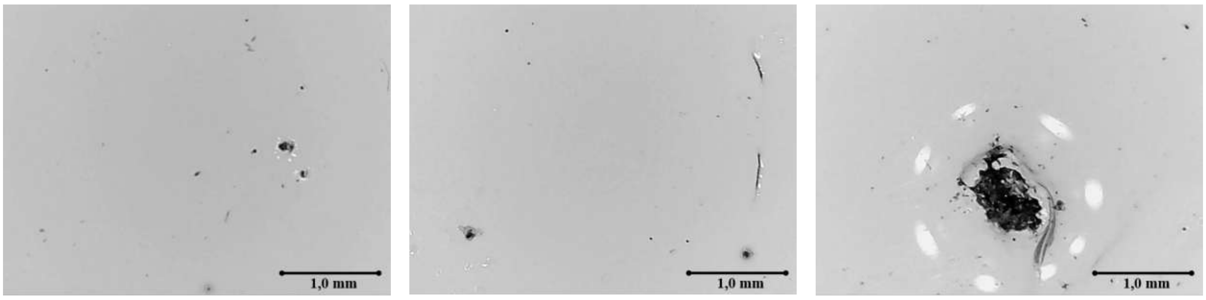

(a) Module 1 over busbar - 10.11.2021 (four months after coating)

(b) Module 1 over busbar - 13.01.2022 (six months after coating)

(c) Picture of crater (open bubble) - 23.02.2022 (seven months after coating)

Figure 5.13: Representative light microscopic images (20× magnification) of the Remsolar coating on the different measurement dates.

To get a better overview of the development of the dark spots, images of examples of many different sizes and growing states on different modules were taken with the 200× magnification of the microscope. Figure 5.14 shows a selection. A comparison with light microscopic images of the original coating on aluminium foil, where a thick coating layer ($\sim 0.8 - 1\,\mathrm{mm}$) was applied for specific measurements, (Fig. 5.15a) shows similarities with some bubbles formed in the beginning state at the coated backsheet (Fig. 5.14a). Therefore, we conjectured that bubbles inside the coating develop because of the solvent share in the coating, which could not evaporate completely, directly after the coating process when thick layers were applied. When these bubbles open on the surface they create a crater.

As there where several frost days in January 2022, we concluded that the tempertaures below freezing had favoured the bursting of the bubbles. Because of the outside environment of the test site, dirt can stick to the developed craters and create the black areas inside. Moreover, some of the bubbles even show a network of threads. This led us to the suggestion that some living organisms started to develop there, attracted by the warm and humid environment of the increased module temperature (Figure 5.14c).

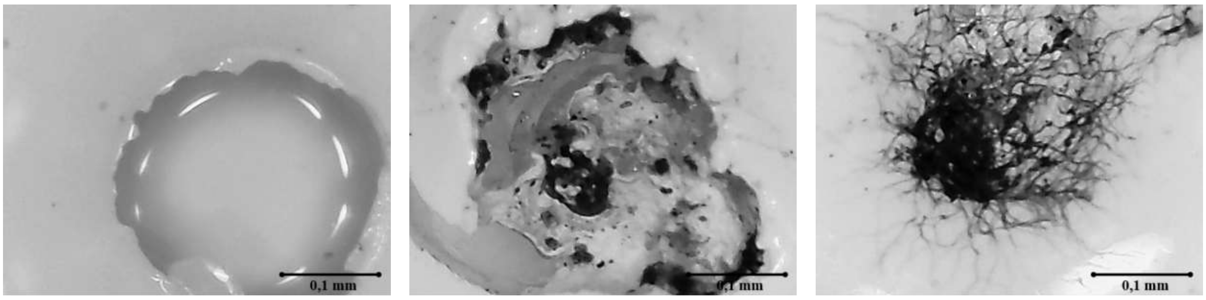

(a) Beginning state of bubble (still clean)

(b) Open bubble with dirt stuck inside

(c) Crater with net of threads

Figure 5.14: Light microscopic images (with 200× magnification) of different dark failure spots on the different Remsolar-coated modules.

For clarification, the coating manufacturer decided to analyse the bubbles in more detail in the laboratory to get insight into their origin and how they can be avoided in the future. Therefore, we dismantled Module 6 of the test site from which some squares of 10 cm × 10 cm with some significant failure dots were cut out and sent for analysis to the laboratory of Rembrantin. In a detailed internal material analysis, Rembrantin proved that the black spots inside the craters came from biological material and some inorganic particles.

To replace the dismantled Module 6 at the test site, we inserted an aged module 65T6 of the same solar park in Germany. We coated it freshly in the laboratory at the beginning of March with the same coating components and the same procedure as described in Section 3.2 for the other modules in July 2021. A module without any hotspots, but deeper longitudinal cracks was chosen. Even though all cracks are filled with coating, some deeper cracks were still visible after the coating procedure and a slight indentation was sensible. Still, Figure 5.15c shows that these cracks are completely sealed with the coating material. Nevertheless, some open bubbles could be detected in the cover coating right after the coating process (see Fig. 5.15b). Because the crack filler is transparent, the light microscope can still detect microcracks on the backsheet surface, although they are sealed with the crack filler and only the cover coating is missing. Therefore, we concluded that the backsheet of the module is completely repaired with Remsolar coating and the mounting on the test site could be done without any doubts.

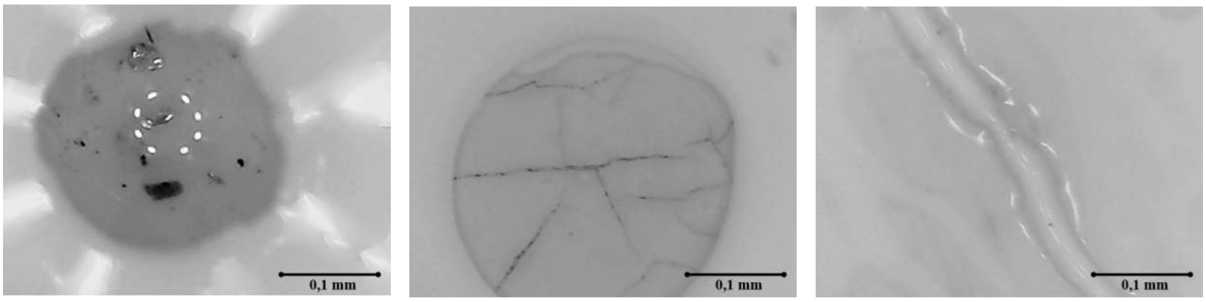

(a) Crater on coated aluminium foil (b) Failure on coated Module 65T6 (c) Sealed longitudinal crack on Module 65T6

Figure 5.15: Light microscopic images (with 200× magnification) of the original state of the Remsolar coating on an aluminium foil (a) and the aged but freshly coated Module 65T6 (b,c).

As a conclusion, it can be said that eight months after coating the sealing of the cracks is still warranted, which was the purpose of the coating. However, the developed craters represent a risk to the coating. Hence the material should be further developed into a solvent-reduced or solvent-free version. Furthermore, the cleaning process before the coating has to be done carefully to avoid dirt particles left on the aged backsheet, which could also be a starting point of the failure dots. It is also suggested to test the coating material with higher temperature changes including degrees below zero to analyse in detail the effect when the coating material is freezing.

Analysis of Infrared Spectra

Potential ageing-induced chemical changes in the coating were analysed by spectroscopic methods. First, the measured infrared spectra (Tab. 4.2) were examined. For identification of the type of polyurethane (PU) used for the coating the significant bands were compared with known spectral library data [22, 64]. Table 5.4 shows the attribution of the peaks in Figure 5.16. Because of the presence of peaks at $1240\,\mathrm{cm}^{-1}$ and $1729\,\mathrm{cm}^{-1}$, which are typical for an ester group, the coating could be identified as polyesterurethane. However, there is also a quite significant peak at $1100\,\mathrm{cm}^{-1}$ which is significant for an ether group. So the Remsolar coating is a polyether-ester-urethan and has both, ether and ester groups in between the PU groups (R_1 and R_2 in Fig. 3.5b).

Table 5.4: Significant IR bands of the Remsolar polyurethane coating [22, 63].

Wavenumber [cm^{-1}]	Functional group
1100	C-O-C symmetric stretching (ether)
1240	C-O-C asymmetric stretching (ester)
1460	asymmetric CH_3 deformation
1526	N-H bending
1690	C=O stretching (urethane group)
1729	C=O stretching (ester group)
2830 - 3010	CH_2 and CH_3 stretching
3340	NH stretching

Moreover, the changes in the spectra over weathering time were analysed. Unfortunately, there were no spectra available of the freshly coated modules for comparison. Therefore, the first idea was to compare the weathered coating with the freshly coated reference module 65T6 before it was mounted on the test site. However, when comparing the spectra of the freshly coated module one day after the coating (and also after one week mounted on the test site) the spectra were not identical to the ones of the previously coated Modules 1-6. With 65T6, there was still a peak visible typical for the unreached hardener at 2274 cm^{-1} which had disappeared in the other coatings already after some days (post-curing). Therefore, it was assumed that the composition of the coating used on this module must have been slightly different with respect to the hardener content due to evaporated solvent. Hence, the IR spectrum of the coating on aluminium foil was used as the original reference, because there the very same coating at the same coating time (July 2021) had been used.

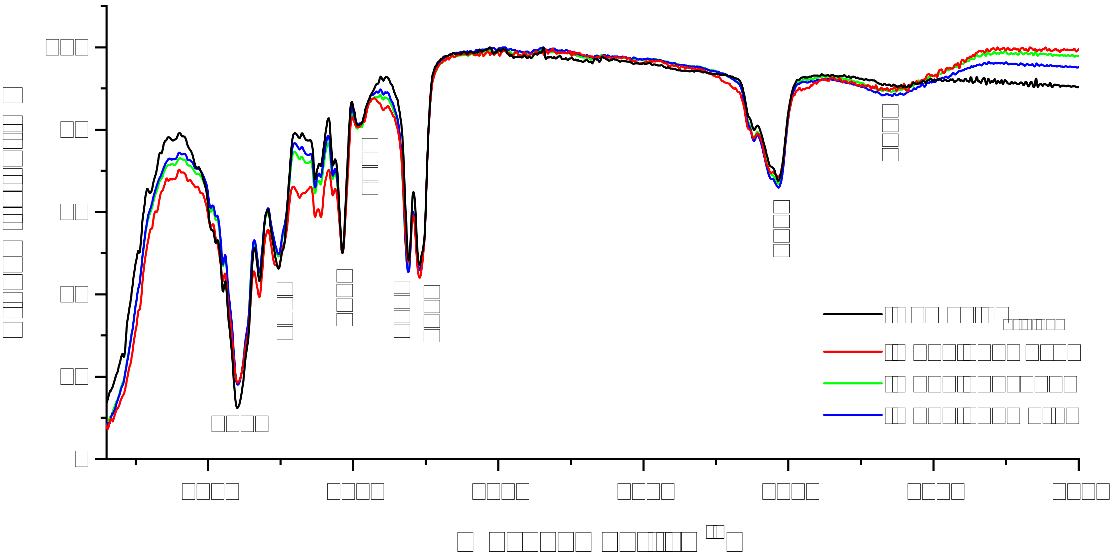

Figure 5.16: IR spectra taken in November 21, January 22 and March 22 of the Remsolar-coated Module 1, in comparison with the original unaged coating on an aluminium foil.

To make a direct comparison possible, the spectra were normalised by setting the peak at the band 1460 cm^{-1} of all the spectra to 50% transmission.

Some peaks in the spectra shown in Figure 5.16 show some slight changes. For example, the ratio of the height of the two C=O (1690 and 1729 cm^{-1}) peaks varies in some spectra of different dates. How significant are these variations? Before suspecting chemical changes in the coating between the different measuring dates, one must compare the ratio of the two C=O bands in the spectra taken on one single day. Figure 5.17 shows that even five measurements taken on different sample positions on Module 1 on the same day in November show some deviation despite normalisation. Especially, the ratio between the two C=O peaks varies. Therefore, it can be assumed that the slight changes in the spectra are not indicative for chemical changes of the coating meaning that the Remsolar coating did not undergo any chemical degradation until March 2022 (eight months after coating).

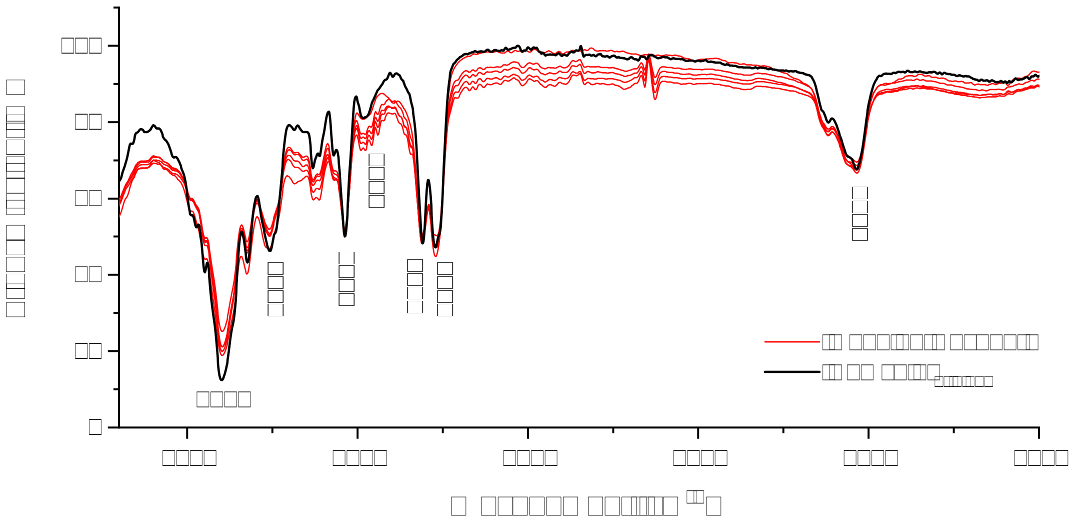

Figure 5.17: Comparison of five IR spectra (a-e) recorded on various measurement areas on the coated backsheet of Module 1 in November 2021 (red) and the original coating on an aluminium foil (black).

Analysis of Raman Spectra

Raman spectra were taken in the field and compared with those of the original state of the Remsolar coating on an aluminium foil. The spectra of the coated backsheets in the field exhibit strong fluorescence (Fig. 5.18). This stems from fluorophores formed upon ageing in the weathered coating [62]. Because of the broad fluorescence smaller peaks are not well resolved. Only the two high bands at 448 cm^{-1} and 610 cm^{-1} are well visible and show that the Remsolar coating has a TiO_2 filler, like the polyamide backsheet. In comparison, the original spectrum nearly has no florescences; hence all bands are better resolved. Because the intensities of all spectra are quite different, they cannot be compared without further data treatment.

To make the bands of the spectra comparable, several processes had to be done with the Perkin Elmer Spectrum Software. The first step was a baseline correction. As this often leads to rather noisy spectra with small prongs suddenly enlarged, it is hard to distinguish them from real peaks. Therefore, it was followed by a smoothing step. As the last step, the spectra were normalised (to the highest peak in the spectrum at 610 cm^{-1}). Figure 5.19 shows the resulting spectra of these analysis steps, where some smaller peaks are now also visible in the spectra of the coated Module 1.

Quite interesting is the peak at 3558 cm^{-1} because it is only visible in the spectrum taken

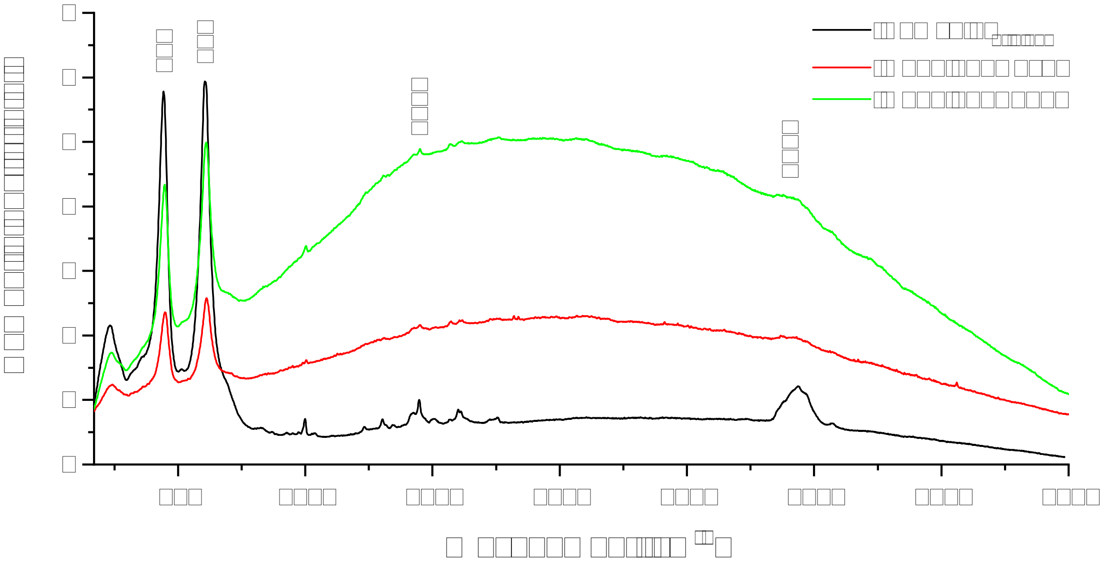

Figure 5.18: Raman spectra on the Remsolar-coated Module 1 in November 21 and February 22 in comparison with the original coating on aluminium foil.

in November. Comparison with the other spectra of this date showed that all of them have this peak so it is not a measurement error. Because of the shape and wavenumber, it was assigned to a free OH group [63]. On this date, the backsheets of the modules were all quite wet by morning dew and had to be dried before spectra could be taken. Probably some water remained on the coating and caused the peak. The other peaks fit to the poly(ester/ether)urethane spectrum and originate from the CH_2 and CH_3 stretching (2850-3030 cm^{-1}), the Urethane group (1611 cm^{-1}) and the CH_2 deformation (1447 cm^{-1}) vibration.

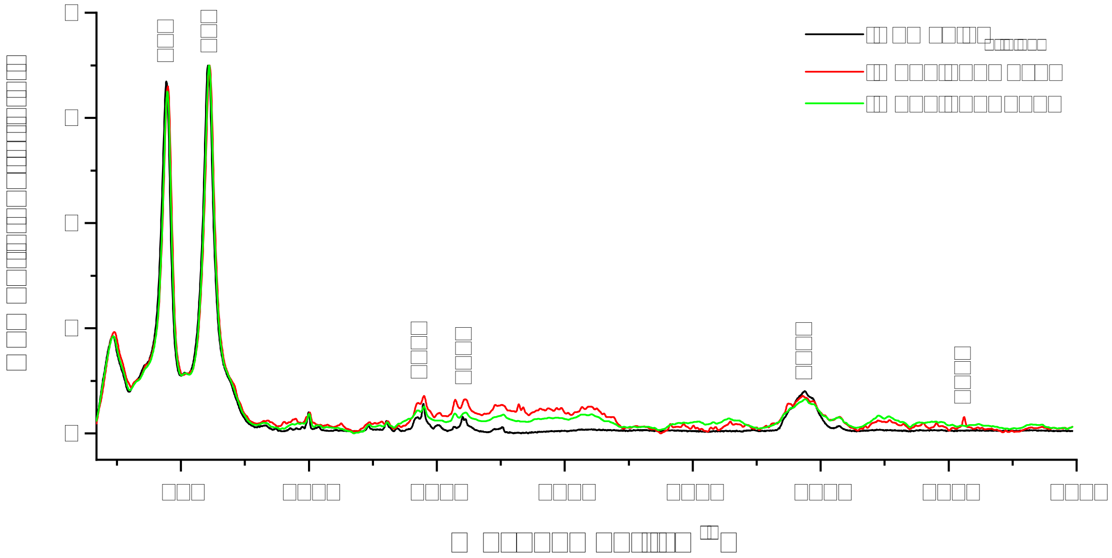

Figure 5.19: Baseline-corrected Raman spectra of the Remsolar coated Module 1 and the original coating (black).

Besides the OH peak in the November spectra, no big changes can be identified in the different Raman spectra. Therefore, the conjecture made after the IR analysis, that the coating did not undergo any chemical degradation, can be reinforced. Increased fluorescence, however, is an indication for ongoing ageing processes in the polymer.

Analysis of Near Infrared Spectra

The final spectroscopic analysis step of the Remsolar coating was the near infrared (NIR) spectra interpretation. Figure 5.20 shows the NIR spectra of Module 1. Again, one representative spectrum was chosen from, in this case ten measurements done on different sample positions. The spectra of the Remsolar coating on Module 1 on the different dates were again compared with the original coating on an aluminium foil. Moreover, they were compared with the spectrum of the uncoated aged backsheet of the reference module, because NIR can detect deeper layers. The first item observable was that the spectra of the coating on Module 1 did not change between November and March. Also, it can be stated that the contribution by the backsheet to the NIR spectra of Module 1 is rather small compared to that of the coating. Still small changes can be found compared to the original coating on the aluminium foil. For example, the small absorption around 5700 cm^{-1} (CH-overtones) originates from the backsheet. Also the band at 4890 cm^{-1} has a higher intensity than in the spectra of the coating on aluminium foil and originates from the backsheet.

This leads to the assumption that the TiO$_2$-filled Remsolar coating is, as the polyamide backsheet, rather opaque in the NIR range compared to other materials. Otherwise, it can be concluded that no hint for ageing-induced changes of the coating on the backsheet of Module 1 could be found eight months after coating.

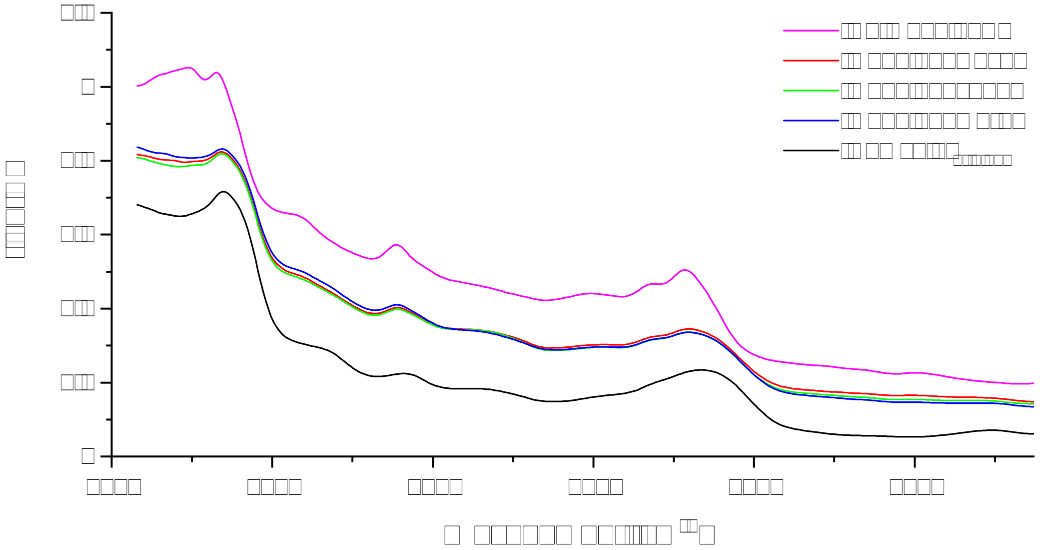

Figure 5.20: NIR spectra of the Remsolar coated backsheet in Module 1 in comparison with the aged backsheet of the reference module (pink) and the original coating on an aluminium foil.

5.2.3 Analysis of the Dowsil Silicone Coating

The same analysis process as described for the Remsolar coating was also applied to the Dowsil-coated modules. Here Module 7 was chosen as a representative because of its easy accessibility.

Visual Inspection

The first step again was the visual examination, which was verified with light-microscopic images of certain sample positions. In November (four months after coating) no changes or physical degradation effects were visible on the coating. However, we monitored a lot of dirt particles on the surface because of the sticky appearance of the silicone. These were of course also visible in the light-microscopic images. Furthermore, it was possible to detect the outlines of some longitudinal cracks under the coating because the silicone is slightly transparent, which was already shown in earlier work [15]. Figure 5.21 shows that the coating above is stable and not affected by the crack.

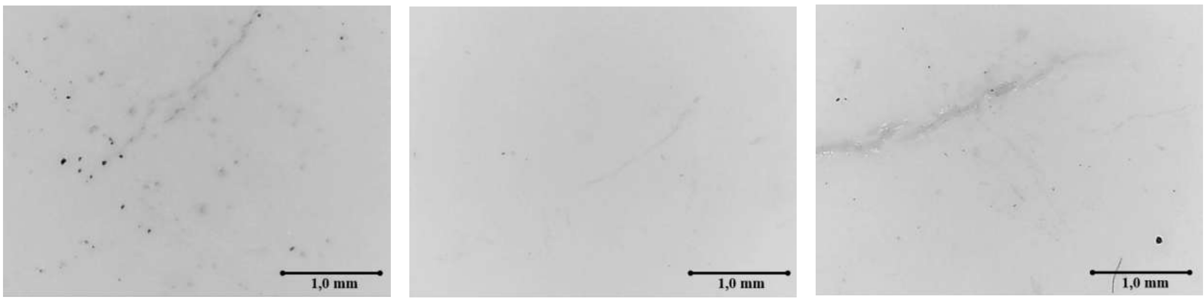

(a) 10.11.2021 - outline of filled crack under the coating.

(b) 14.01.2022 - outline of a microcrack under the coating.

(c) 10.03.2022 - filled crack along a busbar.

Figure 5.21: Light microscopic images of the Dowsil-coated Module 7, with outlines of filled backsheet cracks underneath the slightly transparent silicone coating (Dowsil). No ageing induced changes are visible in the coating as the small black dots are only dirt particles sticking on the surface.

However, in January (six months after coating) several small cracks in the coating along the busbars were visible with the naked eye on the examined Module 7 on that part of the module which protruded over the edge of the roof. This area is particularly exposed to the weather (wind, indirect irradiance, etc.), more than all other modules. Visual examination of all the other Dowsil-coated modules showed that only one other module (Module 9) was affected and there was only one single small crack. This indicates that the pronounced weather exposure made a difference in the probability of crack formation in the coating. Of the whole test site an area of less than 5% of the Dowsil coated backsheets is affected from small cracks. Fortunately, light microscopic images of the small cracks displayed that the backsheet cracks were still filled with coating, so the sealing of the backsheet was still guaranteed (see Figure 5.22). On the last examination day in March (eight months after coating)[4], the propagation of the small cracks had not continued and the backsheet cracks were still filled with coating.

For further development of the coating and its reliability, it is important to continue the examination whether the cracks in the coating are either growing in size or deepness over time. Moreover, the effect of temperature below freezing should be studied in more detail because the cracks in the coating started to grow only in the winter months. If the coating is used on PV modules installed in the field, the higher wind load on the backsheets also needs to be considered, as the cracks only grew in the exposed area of the test site.

---

[4] Also later investigations in July 2022 (one year after the coating process) showed that the backsheet cracks are still filled.

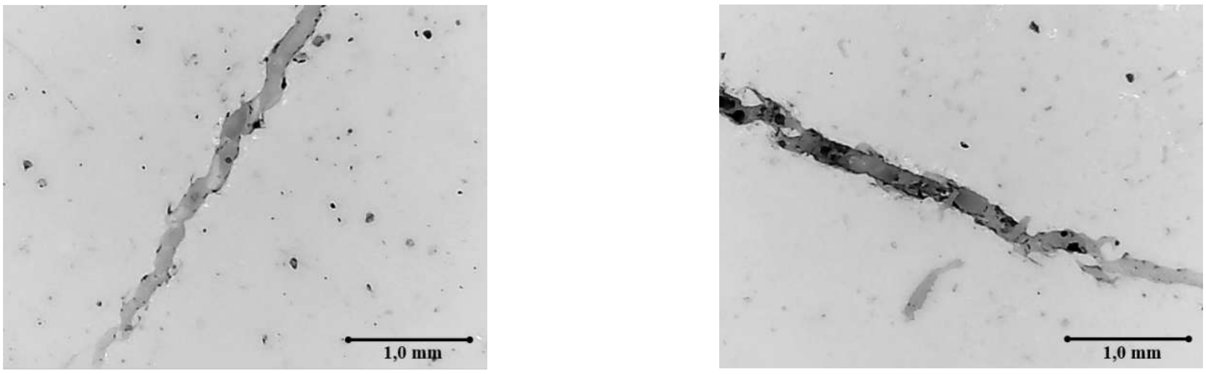

(a) 14.01.2022 - small crack along a busbar, filled with coating.

(b) 10.03.2022 - another small crack along a busbar, filled with coating.

Figure 5.22: Light microscopic images of examples of small cracks on the part of the Dowsil-coated Module 7, which protrudes over the roof and is particularly exposed to weather. All the identified cracks are still filled with coating so the backsheet's sealing is still guaranteed.

Analysis of Infrared Spectra

The visual examination is followed by spectroscopic analysis of potential chemical changes of the coating. First, the IR spectra of the Dowsil coating (see Table 4.2) are used again to characterise the chemical structure of the coating: all peaks could be attributed to silicone (polydimethylsiloxane = PDMS) and $CaCO_3$ as filler. Table 5.5 shows the dedicated functional groups to the significant peaks of the spectra depicted in Figure 5.23.

Table 5.5: Significant IR bands of the Dowsil silicone coating [63, 65].

Wavenumber [cm^{-1}]	Functional group
787	$Si\text{-}(CH_3)_2$
873	$\text{-}CO_3$
1010-1080	Si-O-Si
1259	$Si\text{-}CH_3$
1449	$\text{-}CO_3$
2966	C-H in CH_3

Then, the spectra of the coated backsheet recorded after increasing weathering time were compared to the spectrum of the original coating on an aluminium foil. To make comparison possible, Perkin Elmer Spectrum Software was used to normalise the spectra for the peak at $1259\,cm^{-1}$ to be 35% of transmission. After normalisation (Figure 5.23) only small differences, especially in the relative intensity of the $CaCO_3$ peaks at $873\,cm^{-1}$ and $1449\,cm^{-1}$ were observed. As these differences are also visible in spectra measured on the same day on different sample positions of the modules backside, they were attributed to a inhomogeneous distribution of the filler particles in the coating with no relation to ageing.
Hence it can be stated that no evidence for chemical degradation was detected in the IR spectra of the Dowsil coating eight months after coating.

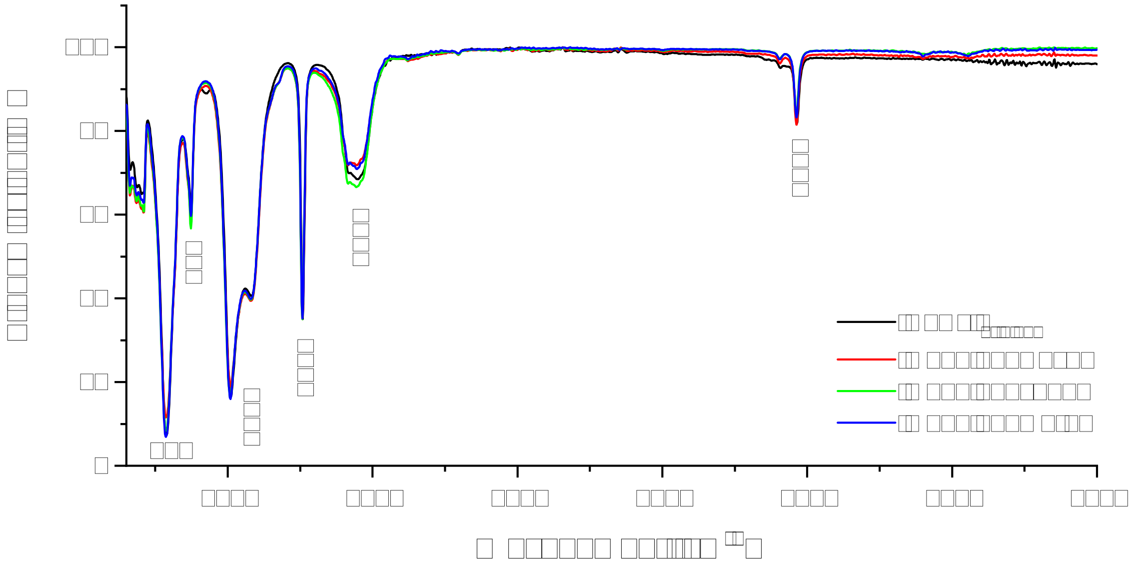

Figure 5.23: Infrared spectra of the Dowsil-coated Module 7 in November 21, January 22 and March 22 in comparison to the original Dowsil coating on an aluminium foil (black).

Analysis of Raman Spectra

Figure 5.24 shows the comparison of the Raman spectra recorded of the Dowsil coating on Module 7 in November 2021 and February 2022 with the original coating on an aluminium foil. Again fluorescence plays a major role in the spectra of the weathered coating making it difficult to compare the different peaks in detail. For better analysis, Perkin Elmer Spectrum Software was used for baseline correction and smoothing of the spectra. Figure 5.25 shows the resulting spectra with differences in the region of 446 cm^{-1} and 610 cm^{-1}. These bands were not visible in the spectrum of the original coating but are quite prominent in both, the November and February measurement of the coated backsheet. Comparison with the Raman spectra of the polyamide backsheet without coating (Fig. 5.8) shows that these are the very positions of the TiO_2 bands. This means that the Dowsil coating is transparent for the used Raman laser and absorption of the material beneath the coating (the backsheet) can also be detected. This is due to the fact that the portable Raman spectrometer with the external probe does not allow for highly confocal measurements, as e.g. a Raman microscope. Therefore, also layers above and below the focal point may contribute to the spectrum. Also the shoulder at 2850 cm^{-1} is attributed to the CH band and the second peak at 1440 cm^{-1} to the CH bending vibration of the backsheet.

Furthermore, a peak at 3560 cm^{-1} is only visible in the spectrum measured in November. This is comparable to the results of the Remsolar coating (see Section 5.2.2 Raman) and is assigned to free OH-bands from water molecules from the wet coating surface.

The remaining of the peaks in Figure 5.25 originate from the Dowsil coating and did not change significantly over time in the field and compared to the original condition. The peak at 489 cm^{-1} comes from the Si-O stretching, the ones at 2907 cm^{-1} and 2967 cm^{-1} from the CH_3 stretching. The $CaCO_3$ filler absorbs at 710 cm^{-1} and 1088 cm^{-1} [63].

In conclusion, fluorescence plays an important role in the Raman spectra of the Dowsil coated backsheet. Partly, this effect can be explained by the impact of the polyamide backsheet on the spectra. But also the coating itself developed higher fluorescence with increasing weathering time. Otherwise, no chemical degradation of the Silicone coating could be detected eight months

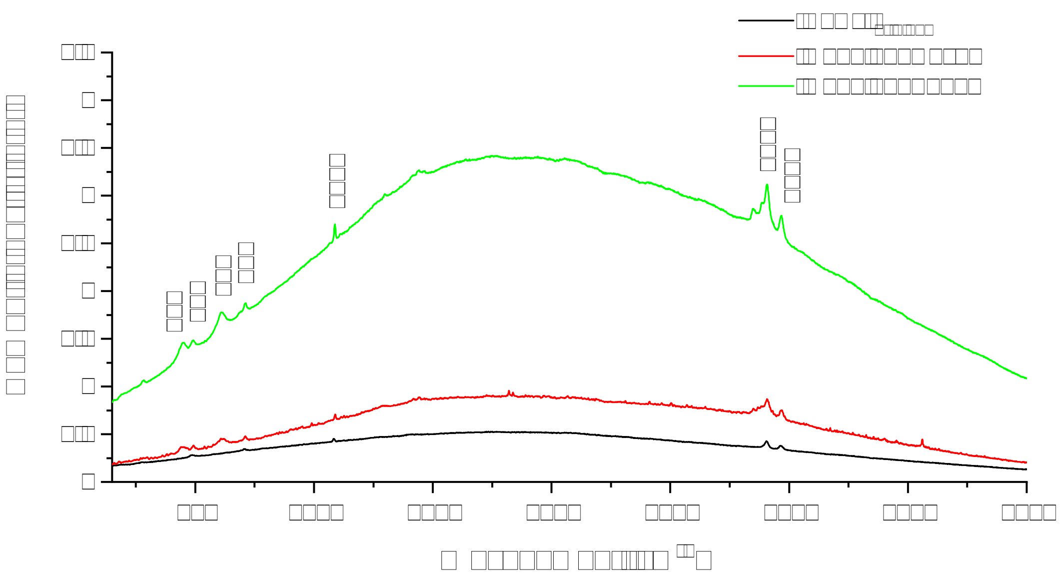

Figure 5.24: Raman spectra of the Dowsil-coated Module 7 in November 21 and February 22 in comparison with the original Dowsil coating on an aluminium foil.

after coating.

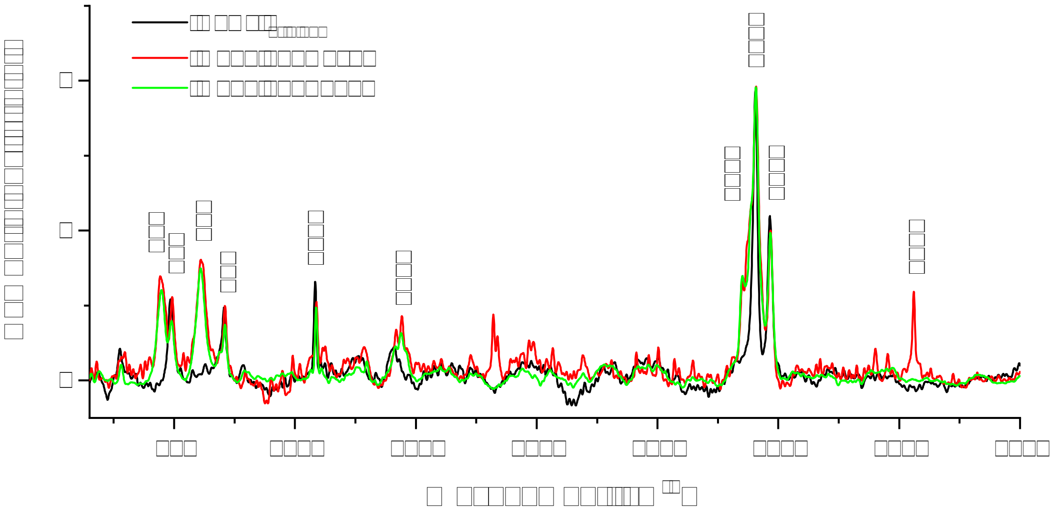

Figure 5.25: Baseline corrected, smoothed and normalised Raman spectra of the Dowsil coating on Module 1 and on the aluminium foil.

Analysis of Near Infrared Spectra

As a final step, the NIR spectra of the Downsil coated backsheet of Module 7 were analysed. As stated before compared to the surface-sensitive measurements with ATR in the mid-IR region, also deeper layers contribute to the NIR spectra. One representative spectrum was chosen from each measurement day and sample for presentation. Figure 5.26 shows the spectra of the coated Module 7 in comparison to the NIR spectra of the original coating (on aluminium foil) and the uncoated backsheet of the reference Module. The spectra recorded in November, January, and March did not show any spectral difference. The contribution of the underlying backsheet to the three spectra recorded of the coating is quite strong. The main spectral features in the spectrum of the PA backsheet are also detectable in the NIR spectra of the coated backsheet of Module 7. This shows that the Dowsil coating is quite transparent in the NIR range.

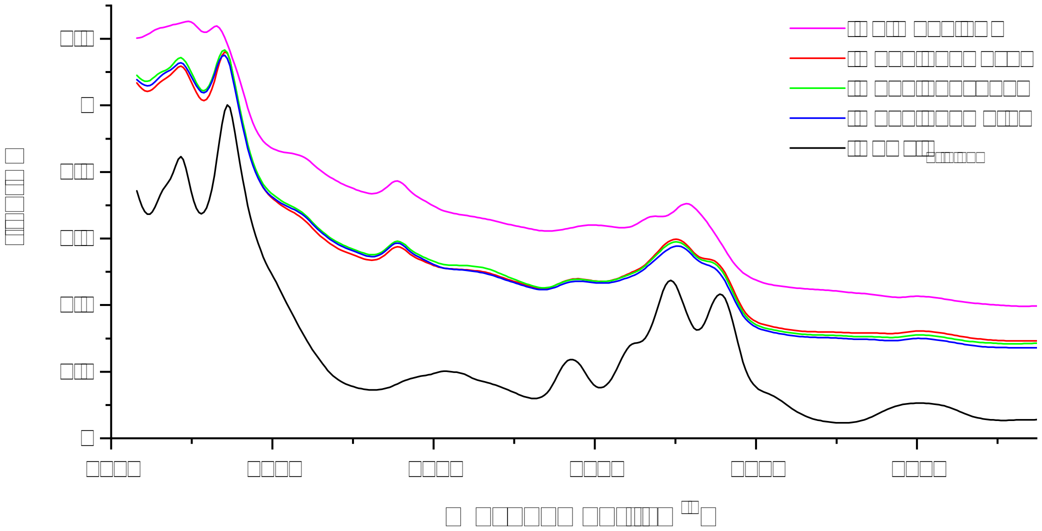

Figure 5.26: NIR spectra of the Dowsil coating in comparison with the uncoated backsheet of the reference module (pink) and the original coating on an aluminium foil (black).

Chapter 6

Conclusion and Outlook

Electricity production from photovoltaics will play a key role in the energy transition of the near future. Although the production and installation of PV modules started to rise already significantly in the last years, still some problems are pending concerning the reliability of some components used in the PV modules. Regarding the repairability of PV modules, especially of cracked backsheets, the R&D project PVRe^2 played an important role in developing possible repair solutions. The main focus lay on modules with polyamide backsheets as they are most affected of cracks. Due to the cracks the backsheets do no longer act as an electrical insulator which presents a safety risk. The insulation should therefore be regained by the coating. As backsheet repair with a coating directly applied in the field is a rather new idea, long-term reliability monitoring of the repaired modules is required. Previous research has identified two suitable coating systems, a polyurethane-based (Remsolar) and a silicone-based (Dowsil) coating. The coatings seal the backsheet cracks completely and form an even cover layer over the whole backsheet to protect it from further degradation. Though, only long-term analysis in the field can give the required feedback for further optimisation steps.

With the monitoring system built up and programmed within this thesis, the two coating types applied to the modules at the test site could be investigated electrically and material wise on a eighth-month basis.

The first part of the work concerned the monitoring of the **electrical performance**. At our pre-tests we could observed, that by closing the deep cracks in the backsheet with the coating, the electrical insulation had been regained, which was an important first step and necessary to safely use the modules at the test site. Two more question remained to be answered:

- Is the coating affecting the electrical power and insulation resistance of the modules?
- How does the electrical performance of the modules change over time?

With the help of a detailed analysis of the power output, which could be done using the monitored environmental conditions in the field (irradiance, module and ambient temperature), it could be stated that the coating was not influencing the electrical performance directly after the coating process or until eight months in operation. After the deep longitudinal cracks had been completely sealed, the degradation of the backsheet stopped and the seal prevented the module from further degradation, which in a next step could have affected the electrical performance.

The second question can only be answered partly. Testing done directly after the coating, revealed a nominal power decrease of the modules of only 8.4% compared to the initial value (label), which fits a normal power loss of modules nine years in the field. However, for long-term analysis, the measurements should be continued for several years to allow for the calculation of annual degradation rates. Moreover, an automatic measurement of the generated power of the whole test site gives a continuous update of the performance.

In the second part, the **coating stability** was monitored and analysed in detail. Here the following questions were posed:

- After what time in the field is the coating changing visually?
- Is the coating chemically stable over time or does it change, and if so, how?
- Does the adhesion of the coating on the backsheet material change over time?

Both coatings applied on the backsheet of the modules were very stable and all cracks could be sealed completely, which was proved by microscopic images. Only in small parts of the coating visual changes were discovered. The Remsolar coating developed some bubbles after seven months in the field, after some cold weeks with degrees below zero. The coating fulfils its purpose as the cracks in the backsheet are still sealed, despite the visible change. However, product development of the coating to wardo a solvent-free solution is recommended. This could not only prevent the start of some bubbles, but is also desirable due to environmental reasons and health standards for the coating workers. Moreover, an improved coating has to be tested again in climate chambers with higher temperature changes including degrees below zero for better mimicking the real influences in the outside environment. The same testing procedure should be applied to the Dowsil coating, where no bubbles occurred but on one module small cracks developed six months after coating, also in the winter. As they could only be detected in areas not protected by the roof, this should especially be considered for field installations of PV modules. For further monitoring of the test site, it is important to follow up on these small cracks in detail and ensure that the cracks in the backsheet remain sealed. Otherwise, most parts of the silicone-coated backsheets did not change visually, apart from dirt particles sticking to the surface of the coating.

After eight months in the field, the chemical structure neither of the Remsolar coating nor of the Dowsil coating had changed (=high stability). This was concluded from a detailed analysis of the IR, Raman, and NIR spectra taken at various stages after the repair process. The only degradation effect visible was increasing fluorescence that could be detected in the Raman spectra, partly overlapping with the measured bands. As this is already happening with small impurities only and is a normal issue of backsheets in the field, it should not influence the chemical stability of the coating in the future.

Concerning the third question, it can be said that the adhesion of the coatings on the polyamide backsheet is good and stays unchanged over eight months of outdoor weathering. This was already tested in detailed pretests before, as part of the material development, as described in the introduction. Tests done as part of this master thesis emphasised this result.

The big question to be answered is:

- How long can the operating time of a module with a cracked backsheet be extended by the repair coating?

This is the most important question and the reason why this master thesis was initiated. As the modules with deep longitudinal cracks would have had to be disposed of due to safety reasons, the prolonged operating time only depends on how long the coating is stable, seals the cracks and, thus the insulation properties are fulfilled. Until now it can only be said, that these conditions are still fulfilled after eight months outdoors. The goal is to prolong this time to ten years which can be investigated with the built monitoring system within this master thesis. Hence, it is proposed to continue the detailed monitoring of the chemical stability on a two-monthly basis and the continuous data gathering of the electrical performance of the modules.

To conclude, the first important step was achieved by the outdoor analysis of the modules repaired with the developed coatings within this thesis. Based on the first results, it is proposed that the electrical performance should be monitored and analysed continuously either with an automatic calculation of the nominal power or with continuous calculations of the performance ratio of the test site. Of interest could also be a comparison with uncoated and hence unrepaired modules to get direct results on repair-induced performance differences. This can only be done at a fenced-off test site because the modules with the cracked backsheets have to be out of reach for uninformed persons due to safety risks. Moreover, in the future coating solutions should be developed not only for cracked polyamide backsheets but also for other backsheet materials. Although they are less affected, many backsheet materials can develop failures, as discussed in the introduction. Repair solutions for backsheet cracks of different materials prolong the operating time of PV modules in general and confirm the trust in the reliability of the electricity production through photovoltaics.

List of Figures

1.1 PV module structure and of defects affected PV module parts. 2
1.2 Different crack types in polyamide (PA) backsheets. 3

2.1 One-dimensional display of the semiconductor band structure in an energy momentum diagram. The transition of an electron to the conduction band in a direct (left) and indirect (right) semiconductor [17]. 8
2.2 Band structure of doped semiconductor, modified from [17]. 9
2.3 Recombination processes: (a) radiative recombination over the whole bandgap; (b) Auger recombination; (c) non-radiated (Shockley-Read-Hall) recombination [18]. 11
2.4 PN-junction with the aligned Fermi level [20]. 12
2.5 Diode characteristics, modified from [17]. 13
2.6 Correspondence of quantum transitions with parts of the electromagnetic spectrum [24]. 15
2.7 Morse potential of a two atomic molecule in comparison with the harmonic potential and their respective energy states [25]. 16
2.8 Sketch of a FTIR spectrometer and its most important parts [26]. 18
2.9 Comparison of different excitation effects: IR, Rayleigh scattering, Raman scattering (Stokes and anti-Stokes) and fluorescence. Figure modified from [27]. . . . 20
2.10 Comparison of spectra of different spectroscopic methods of a TPT (Tedlar©) backsheet. 21
2.11 Sketch of a dispersive Raman spectrometer and its most important parts [30]. . . 22

3.1 PV test site with the twelve coated modules mounted on the roof. 23
3.2 Arrangement of the modules on the test site with the two coatings (Remsolar and Dowsil) on the backsheet and the placement of the inverter, the pyranometer (P) and the five temperature sensors (T1-4 module temperature and T-A ambient temperature). 24
3.3 Polyamide backsheet information. 25
3.4 Light microscope images of cross-sections of coated modules with deep cracks. . . 26
3.5 Coating procedure (a) and chemical structures of coating materials (b,c). 27

4.1 Raspberry Pi 4: GPIO header pin assignment [46]. 30
4.2 Three of the five temperature sensors mounted on the testsite. 32
4.3 Node-RED flow for the temperature measurement. 32
4.4 LP PYRA 03 pyranometer mounted next to Module 1, parallel to the module plane (plane-of-array irradiance), with the test site in the background. 33
4.5 Node-RED flow for the irradiance measurement. 34
4.6 Node-RED flow for the total power and energy production of the test site. 35
4.7 Node-RED flow for the DC produced power by the test site, and the AC total current value. 36

4.8 Node-RED flow for reading the voltage and current at the maximum power point (MPP). . . . 37
4.9 Measurement devices at the test site . . . 39
4.10 Measurement with the Raman laser at the test site. . . . 41
4.11 Measurement with the NIR-spectrometer on the Remsolar-coated Module 1. . . . 42

5.1 I-V curve measurements of Module 1 (Remsolar) and Module 7 (Dowsil) in July 2021 at the meteorological conditions stated in Table 5.1. . . . 45
5.2 Temperature profile of all five temperature sensors (Sensor 1 and 2 on Module 7; Sensor 3 and 4 on Module 1) on 21.03.2022. . . . 46
5.3 Irradiance at the test site in comparison to two ZAMG monitoring stations on 21.03.2022. . . . 47
5.4 Comparison of the generated power before (DC) and after (AC) conversion of the inverter. The comparison with the irradiance shows the power that could have been produced without any shading. . . . 48
5.5 Efficiency of the Fronius inverter dependent on the generated power. . . . 48
5.6 Calculated nominal power for every minute on 21.03.2021 between 07:30 and 16:30. The trend line presents how the data would look without the shading. . . . 50
5.7 Uncoated reference module: light microscopic images of different crack types of the weathered PA backsheet. . . . 51
5.8 Raman spectra of the uncoated PA backsheet of the reference module weathered (red) and under the label (green) in comparison with the original PA backsheet (black). . . . 52
5.9 Raman spectra analysis to compare the amount of TiO_2 in the backsheets. . . . 53
5.10 Infrared spectra of different sample positions of the uncoated but aged PA backsheet of the reference module compared to the original unaged PA backsheet (black). . . . 54
5.11 Difference spectrum of the infrared spectra in the crack area of the aged reference module's backsheet and the original unaged backsheet. . . . 55
5.12 NIR spectra of the aged PA backsheet in comparison with spectra of the unaged original backsheet and the EVA encapsulant. . . . 56
5.13 Representative light microscopic images (20× magnification) of the Remsolar coating on the different measurement dates. . . . 57
5.14 Light microscopic images (with 200× magnification) of different dark failure spots on the different Remsolar-coated modules. . . . 57
5.15 Light microscopic images (with 200× magnification) of the original state of the Remsolar coating on an aluminium foil (a) and the aged but freshly coated Module 65T6 (b,c). . . . 58
5.16 IR spectra taken in November 21, January 22 and March 22 of the Remsolar-coated Module 1, in comparison with the original unaged coating on an aluminium foil. . . . 59
5.17 Comparison of five IR spectra (a-e) recorded on various measurement areas on the coated backsheet of Module 1 in November 2021 (red) and the original coating on an aluminium foil (black). . . . 60
5.18 Raman spectra on the Remsolar-coated Module 1 in November 21 and February 22 in comparison with the original coating on aluminium foil. . . . 61
5.19 Baseline-corrected Raman spectra of the Remsolar coated Module 1 and the original coating (black). . . . 61
5.20 NIR spectra of the Remsolar coated backsheet in Module 1 in comparison with the aged backsheet of the reference module (pink) and the original coating on an aluminium foil. . . . 62

5.21 Light microscopic images of the Dowsil-coated Module 7, with outlines of filled backsheet cracks underneath the slightly transparent silicone coating (Dowsil). No ageing induced changes are visible in the coating as the small black dots are only dirt particles sticking on the surface. 63
5.22 Light microscopic images of examples of small cracks on the part of the Dowsil-coated Module 7, which protrudes over the roof and is particularly exposed to weather. All the identified cracks are still filled with coating so the backsheet's sealing is still guaranteed. 64
5.23 Infrared spectra of the Dowsil-coated Module 7 in November 21, January 22 and March 22 in comparison to the original Dowsil coating on an aluminium foil (black). 65
5.24 Raman spectra of the Dowsil-coated Module 7 in November 21 and February 22 in comparison with the original Dowsil coating on an aluminium foil. 66
5.25 Baseline corrected, smoothed and normalised Raman spectra of the Dowsil coating on Module 1 and on the aluminium foil. 66
5.26 NIR spectra of the Dowsil coating in comparison with the uncoated backsheet of the reference module (pink) and the original coating on an aluminium foil (black). 67

List of Tables

1.1 Overview of repair materials (Abbreviations: 1-K: 1 component; 2-K: 2 components system; RT: room temperature). 5

3.1 Electrical characteristics (power P_{MPP}, voltage U_{MPP} and current I_{MPP} at the maximum power point; open-circuit voltage U_{OC} and short-circuit current I_{SC}) of the modules according to the type label. 24
3.2 Material characteristics of Remsolar coating, information taken from [39, 40, 41]. 27

4.1 Light microscopic images 39
4.2 FTIR measurements 40
4.3 Raman measurements with a laser intensity of 100% and a time multiplier of 5. . 41
4.4 NIR measurements 42

5.1 Characteristic electric data of the coated modules as derived from the I-V Curves 44
5.2 Analysis of the amount of TiO_2 in the backsheets (surface near region). 53
5.3 Assignment of the IR peaks of the PA backsheet [36][63]. 54
5.4 Significant IR bands of the Remsolar polyurethane coating [22, 63]. 59
5.5 Significant IR bands of the Dowsil silicone coating [63, 65]. 64

Abbreviations

1-K	One component
2-K	Two component
AC	Accelerated current
ADC	Analogue-digital converter
ATR	Attenuated total reflection
$CaCO_3$	Calcium carbonate
CCD	Charge-coupled device
CO^2	Carbon dioxid
DC	Direct current
DSTD	Deuterated triglycine sulfate detector
EHP	Electron-Hole Pair
EU	European Union
EVA	Ethylene-vinyl acetate
FT	Fourier-transformation
FTIR	Fourier-transformation infrared
Ge	Germanium
GND	Ground
GPIO	General-purpose input/output
IR	Infrared
MCT	Mercury cadmium telluride
MPP	Maximum Power Point
MQT	Module Quality Test
MQTT	Message Queuing Telemetry Transport
NIR	Near-infrared
PA	Polyamide
PDMS	Polydimethylsiloxane
PET	Polyethylene terephthalate
PGA	Programmable gain amplifier
PO	Polyolefine
PP	Polypropylen
PU	Polyurethane
PV	Photovoltaics
PVDF	Polyvinylidene difluoride
PVF	Polyvinyl fluoride
RPI	Raspberry Pi
RT	Room temperature
Si	Silicon
SiC	Silicon carbide
TiO_2	Titanium dioxide
UV	Ultraviolet
ZAMG	Zentralanstalt für Meterologie und Geodynamik

Bibliography

[1] Eurostat. *Renewable energy in 2020*. Jan. 2022. URL: `https://ec.europa.eu/eurostat/statistics-explained/index.php?title=File:Renewable_energy_2020_infographic_18-01-2022.jpg`.

[2] EuropeanComission. *REPowerEU with Clean Energy Factsheet*. May 2022. DOI: `doi:10.2775/528866`.

[3] P. Biermayr et al. *Innovative Energietechnologien in Österreich: Marktentwicklung 2021.* Vol. 21b/2022. Bundesministerium Klimaschutz Umwelt Energie Mobilität Innovation und Technologie, 2022.

[4] T. Dobra et al. *Environmental and economic assessment of repair solutions for cracked backsheets in photovoltaic modules.* In: *SEEP 2021*. Sept. 2021.

[5] K. P. Bhandari et al. *Energy payback time (EPBT) and energy return on energy invested (EROI) of solar photovoltaic systems: A systematic review and meta-analysis.* In: *Renewable and Sustainable Energy Reviews* 47.C (2015), pp. 133–141. DOI: `10.1016/j.rser.2015.02.05`.

[6] *Sustainable photovoltaics.* In: *Energy Research 4th call, Topic 5.5 Photovoltaics Project Nr.: 867267.* 2018.

[7] D. C. Jordan et al. *Compendium of photovoltaic degradation rates.* In: *Progress in Photovoltaics: Research and Applications* 24.7 (2016), pp. 978–989. DOI: `https://doi.org/10.1002/pip.2744`.

[8] J. Tracy et al. *Survey of material degradation in globally fielded PV modules.* In: *2019 IEEE 46th Photovoltaic Specialists Conference (PVSC).* 2019, pp. 0874–0879. DOI: `10.1109/PVSC40753.2019.8981140`.

[9] J. Svarc. *Solar Panel Construction.* Clean Energy Reviews. Mar. 2020.

[10] G. C. Eder et al. *Error analysis of aged modules with cracked polyamide backsheets.* In: *Solar Energy Materials and Solar Cells* 203 (2019), pp. 0927–0248. DOI: `https://doi.org/10.1016/j.solmat.2019.110194`.

[11] M. Halwachs et al. *Statistical evaluation of PV system performance and failure data among different climate zones.* In: *Renewable Energy* 139 (2019), pp. 1040–1060. ISSN: 0960-1481. DOI: `https://doi.org/10.1016/j.renene.2019.02.135`.

[12] Y. Voronko et al. *Repair options for PV modules with cracked backsheets.* In: *Energy Science and Engineering* 9 (June 2021). DOI: `10.1002/ese3.936`.

[13] Y. Lyu et al. *Drivers for the cracking of multilayer polyamide-based backsheets in field photovoltaic modules: In-depth degradation mapping analysis.* In: *Progress in Photovoltaics: Research and Applications* 28.7 (2020), pp. 704–716. DOI: `https://doi.org/10.1002/pip.3260`.

[14] *IEC 61215-2: Terrestrial Photovoltaic (PV) Modules – Design Qualification and Type Approval – Part 2: Test Procedures.* International Electrotechnical Commission, Feb. 2021.

[15] G. Beaucarne et al. *Repair and preventive maintenance of PV modules with degrading backsheets using flowable silicone sealant.* In: *Progress in Photovoltaics Research and Applications* (Oct. 2021). DOI: `10.1002/pip.3492`.

[16] Y. Voronko and G. Eder. *Repair of cracked backsheets: long term stability.* In: *EU PVSEC 2021.* 2021.

[17] W. Demtröder. *Experimentalphysik 3: Atome, Moleküle und Festkörper.* ger. Springer-Lehrbuch. Berlin, Heidelberg: Springer-Verlag Berlin Heidelberg, 2009. ISBN: 3642039111. DOI: `10.1007/978-3-642-03911-9`.

[18] A. Reinders et al. *Photovoltaic Solar Energy.* John Wiley & Sons, Ltd, 2017. ISBN: 978-1-118-92746-5.

[19] A. Goetzberger, B. Voß, and J. Knobloch. *Sonnenenergie: Photovoltaik.* 2nd ed. Teubner, Stuttgart, 1997. ISBN: 3-519-03214-7.

[20] R. Hui. *Chapter 4 - Photodetectors.* In: *Introduction to Fiber-Optic Communications.* Ed. by R. Hui. Academic Press, 2020, pp. 125–154. ISBN: 978-0-12-805345-4. DOI: `10.1016/B978-0-12-805345-4.00004-4`.

[21] M. Kaltschmitt, W. Streicher, and A. Wiese. *Erneuerbare Energien : Systemtechnik, Wirtschaftlichkeit, Umweltaspekte.* ger. Vierte, aktualisierte, korrigierte und ergänzte Auflage. Berlin, Heidelberg: Springer-Verlag Berlin Heidelberg, 2006. ISBN: 354028205X. DOI: `10.1007/3-540-28205-X`.

[22] H. W. Siesler. *Vibrational spectroscopy of polymers.* In: *International Journal of Polymer Analysis and Characterization* 16.8 (2011), pp. 519–541. DOI: `10.1080/1023666X.2011.620234`.

[23] H. Günzler and H.-U. Gremlich. *IR-Spektroskopie: eine Einführung.* ger. 4th ed.. Weinheim: Wiley-VCH GmbH & Co. KGaA, 2003. ISBN: 3527662855.

[24] C. Geiger. *An Introduction to Spectroscopic Methods in the Mineral Sciences and Geochemistry.* In: Jan. 2004, pp. 1–42. ISBN: 963 463 662 4.

[25] M. Somoza. *Morse-Potential.* Mar. 2006. URL: `https://de.wikipedia.org/wiki/Morse-Potential#/media/Datei:Morse-potential.png`.

[26] J. Ojeda and M. Dittrich. *Fourier transform infrared spectroscopy for molecular analysis of microbial cells.* In: *Methods in molecular biology (Clifton, N.J.)* 881 (Apr. 2012), pp. 187–211. DOI: `10.1007/978-1-61779-827-6_8`.

[27] H. Fujita et al. *Bright dots and smart optical microscopy to probe intracellular events in single cells.* In: *Frontiers in bioengineering and biotechnology* 6 (2018), p. 204. ISSN: 2296-4185. DOI: `10.3389/fbioe.2018.00204`.

[28] OriginLabCorporation. *OriginLab Data Analysis and Graphing Software.* URL: `https://www.originlab.com/`.

[29] R. L. McCreery. *Raman Spectroscopy for Chemical Analysis.* Vol. 157. Chemical Analysis A Series of Monographs of Analytical Chemistry ans its Application. John Wiley & Sons, 2000. ISBN: 0-471-25287.

[30] D. Regonini. *Anodised TiO2 nanotubes: synthesis, growth mechanism and thermal Stability.* PhD thesis. Jan. 2008.

[31] R. Moretón, E. Lorenzo, and L. Narvarte. *Experimental observations on hot-spots and derived acceptance/rejection criteria.* In: *SolarEnergy* 118 (2015), pp. 28–40. DOI: `doi:10.1016/j.solener.2015.05.009`.

[32] *Schott Power Poly Serie.* SCHOTT Solar AG. Mainz, Germany.

[33] *Datasheet ICOSOLAR AAA 3554.* Isovoltaic AG. May 2011.

[34] P. Gebhardt, L. P. Bauermann, and D. Philipp. *Backsheet chalking theoretical background and relation to backsheet cracking and insulation failures*. In: 2018.

[35] C. Zhou et al. *The methylene infrared vibration and dielectric behavior monitored by amide group arrangement for long chain polyamides*. In: *Polymer* 190 (2020), p. 122231. ISSN: 0032-3861. DOI: `https://doi.org/10.1016/j.polymer.2020.122231`.

[36] B. S. Chernev and G. C. Eder. *Spectroscopic characterization of the oligomeric surface structures on polyamide materials formed during accelerated aging*. In: *Applied Spectroscopy* 65.10 (2011), pp. 1133–1144. ISSN: 0003-7028-11-6510-1133.

[37] Y. Fujiwara and S. H. Zeronian. *Crystallization of cyclic oligomers on the surface of nylon 6 fibers*. In: *Journal of Applied Polymer Science* 23.12 (1979), pp. 3601–3619. DOI: `https://doi.org/10.1002/app.1979.070231216`.

[38] G. W. Becker and D. Braun. *Technische Thermoplaste, Polyamide Kunststoff-Handbuch*. L. Bottenbruch and R. Binsack, Hanser, 1998.

[39] *Sicherheitsdatenblatt REM PVR Rissfüller VZ (mit Indikator) Komponente A*. 1.0. Rembrandtin Coating GmbH. Mar. 2021.

[40] *Sicherheitsdatenblatt REM PVR Deckbeschichtung VZ Komponente A*. 1.0. Rembrandtin Coating GmbH. Mar. 2021.

[41] *Sicherheitsdatenblatt Haerter 442*. 2.02. Rembrandtin Coating GmbH. Mar. 2021.

[42] Roland.chem. *Allgemeine Struktur von linearen Polyurethanen*. URL: `https://commons.wikimedia.org/w/index.php?curid=36670935`.

[43] *Technical Data Sheet DOWSILTM 7094 Flowable Sealant*. The Dow Chemical Company. 2020.

[44] *Fronius Symo 3.0-3-M Technical Data*. 23rd ed. Fronius International GmbH. Dec. 2021.

[45] G. Halfacree. *The official Raspberry Pi Beginners Guide*. Ed. by P. King. Russel Barnes, 2020.

[46] Raspberry Pi Ltd. URL: `https://www.raspberrypi.com/documentation/computers/os.html#gpio-and-the-40-pin-header`.

[47] OpenJS Foundation and Contributors. URL: `https://nodered.org`.

[48] Grafana Labs. URL: `https://grafana.com/grafana/`.

[49] A. Gassner. *Setup of ambient influence sensors for a test site of repaired PV modules*. Project thesis. TU Wien, Institute of Applied Physics, 2022.

[50] DeltaOhm. *Pyranometer LPPYRA03 Operating manual*. GHM Group.

[51] *Ultra-Small, Low-Power, 16-Bit Analog-to-Digital Converter with Internal Reference ADS1113, ADS1114, ADS1115*. Texas Instruments. 2009.

[52] *Fronius Datamanager Modbus TCP & RTU*. Fronius Solar Energy.

[53] *SunSpec Information Model Specification*. 1.9. Sunspec Alliance. URL: `https://sunspec.org/wp-content/uploads/2015/06/SunSpec-Information-Models-12041.pdf`.

[54] M. Heidl. *Tolernce Fronius Symo 3.0-3-M - 8.2-3-M*. Fronius International GmbH. Wels, Jan. 2018.

[55] Fronius. URL: `http://www.fronius.com/QR-link/0006`.

[56] *PVPM1040C Peakleistungs-u und Kennlinien-Messgeraet fuer PV-Module und -Generatoren*. PV-Engineering GmbH. Nov. 2016.

[57] *Exoscan Instrument User's Guide*. A2 Technologies Polytec GmbH.

[58] *i-Raman Plus Portable Raman System User Manual*. BWS465-532S. B&WTEK.

[59] *NIR Spektrometer SYS-IR-R-P*. trinamiX.

[60] *Zamg data hub*. Zentralanstalt für Meteorologie und Geodynamik. URL: `https://data.hub.zamg.ac.at/dataset/klima-v1-10min`.

[61] PerkinElmerInc. *Perkin Elmer Spectrum IR Software*. URL: `https://www.perkinelmer.com/de/product/software-kit-spectrum-10-es-lx108875`.

[62] G. C. Eder et al. *Climate specific accelerated ageing tests and evaluation of ageing induced electrical, physical, and chemical changes*. In: *Progress in Photovoltaics: Research and Applications* 27.11 (2019), pp. 934–949. DOI: `https://doi.org/10.1002/pip.3090`.

[63] G. Socrates. *Infrared and Raman Characteristic group Frequencies*. 3rd ed. John Wiley and Sons Ltd, 2001. ISBN: 0-471-85298-8.

[64] D. O. Hummel. *Atlas of Polymer and Plastics Analysis*. 3rd ed. Vol. 1. Part b. S.901. Hanser Publishers, 1991.

[65] S. Fan et al. *Characterization of HTV silicone rubber with different content of ATH filler by mechanical measurements, FTIR and XPS analyzes*. In: *2018 12th International Conference on the Properties and Applications of Dielectric Materials (ICPADM)*. 2018, pp. 888–891. DOI: `10.1109/ICPADM.2018.8401171`.